Rochester Institute of Technology

RIT Digital Institutional Repository

Theses

4-22-2020

Polarization Engineering for Deep-Ultraviolet Light-Emitting Diodes

Cheng Liu
cl7007@rit.edu

Follow this and additional works at: https://repository.rit.edu/theses

Recommended Citation

Liu, Cheng, "Polarization Engineering for Deep-Ultraviolet Light-Emitting Diodes" (2020). Thesis. Rochester Institute of Technology. Accessed from

This Dissertation is brought to you for free and open access by the RIT Libraries. For more information, please contact repository@rit.edu.

R·I·T

Polarization Engineering for Deep-Ultraviolet Light-Emitting Diodes

by

Cheng Liu

A dissertation submitted in partial fulfillment of the requirements
for the degree of Doctor of Philosophy in Microsystems Engineering

Microsystems Engineering Program
Kate Gleason College of Engineering

Rochester Institute of Technology
Rochester, New York
April 22nd, 2020

Polarization Engineering for Deep-Ultraviolet Light-Emitting Diodes

by

Cheng Liu

Committee Approval:

We, the undersigned committee members, certify that we have advised and/or supervised the candidate on the work described in this dissertation. We further certify that we have reviewed the dissertation manuscript and approve it in partial fulfillment of the requirements of the degree of Doctor of Philosophy in Microsystems Engineering.

Dr. Jing Zhang Date
Associate Professor

Dr. Seth Hubbard Date
Professor

Dr. Stefan F. Preble Date
Professor

Dr. Parsian K. Mohseni Date
Assistant Professor

Dr. Stephen Boedo Date
Professor

Certified by:

Dr. Bruce Smith Date
Director, Microsystems Engineering Program

ABSTRACT

Kate Gleason College of Engineering
Rochester Institute of Technology

Degree: Doctor of Philosophy **Program**: Microsystems Engineering

Authors Name: Cheng Liu

Advisors Name: Jing Zhang

Dissertation Title: Polarization Engineering for Deep-Ultraviolet Light-Emitting Diodes

The new Coronavirus or Covid-19 has already became a world-wide pandemic. As of April 22nd, 2020, there are more than 2593129 confirmed case and 179725 total deaths. To fight against the Coronavirus, tremendous efforts have been made for slowing down the spread, such as social distancing. Recently, deep-ultraviolet (DUV) light-emitting diodes (LEDs) are demonstrated to be super effective to deactivate the virus/bacteria. In addition, the outstanding properties such as long life-time, compact size and environmental-friendly from DUV LEDs make them ideal for protecting people from the Coronavirus. However, all AlGaN-based DUV LEDs suffers from low external quantum efficiency issue. Among all the determinants, optical polarization significantly influences internal quantum efficiency and light extraction efficiency from the devices. In this work, we theoretically investigated the impact of the optical polarization properties on DUV LED device efficiencies by using a self-consistent 6-band $\boldsymbol{k \cdot p}$ model and a finite-difference time-domain (FDTD) software. The factors influencing optical polarization switching are also examined and verified. In addition, this work proposed and demonstrated a novel delta-quantum well (QW) design to engineer the optical polarization from the active region. The molecular beam epitaxy (MBE)-grown AlGaN-delta-GaN structure in this study shows an extremely high 85% internal quantum efficiency at 255 nm on a conventional AlN/sapphire substrate, which indicates the delta-QW design is promising for efficient DUV LEDs. Furthermore, several other techniques, such as top-down nanowire arrays, sphere current spreading LEDs, AlGaN substrate and microsphere arrays, are also developed to further improve device efficiency.

ACKNOWLEDGMENTS

Pursuing this Ph.D. has been a truly life-changing experience for me, and I will never regret for this decision. There are many challenging moments during the past six years, and it would not have been possible to finish it without the support and help that I received from many people.

First of all, I want to thank my parents, Jixiang Liu and Yumei Liu. Words cannot express how grateful I am for all the sacrifices that you've made. Also special thanks to my family, Sitong Zhou, Zhengzheng Zhou, Meiling Na, Zheng Liu, and Xu xu. Thank you for supporting and understanding me for everything. Love you all.

I would like to express my appreciation to my advisor, Prof. Jing Zhang. You are a tremendous mentor who always encourages my research and guides me to grow as a research scientist. It's my honor to be one of your first Ph.D. students, having the opportunity to build up the lab, to explore the research topics. The flexible and professional research environment you provide to us is of great importance for the success of my graduate study.

I would also like to thank Prof. Seth Hubbard, Prof. Stefan F. Preble, Prof. Parsian K. Mohseni and Prof. Stephen Boedo for serving as my dissertation committees, and for sharing your brilliant comments and suggestions. Thanks to Microsystems Engineering Program at RIT, especially Prof. Bruce Smith and Lisa Zimmerman for all the help.

Many thanks also to my lab mates, Yu Kee Ooi, Matthew Hartensveld, Bryan Melanson, Vijaygopal Thirupakuzi Vangipuram, and Gildas Ouin for letting my Ph.D. career to be an enjoyable experience. I will not be possible to get this work done without all your helps and contributions.

I would also like to acknowledge our collaborators from Cornell University, Prof. Debdeep Jena, Prof. Grace (Huili) Xing, Kevin Lee, and SM Moududul Islam. Thank you so much to allow me to operate your Gen-10 Veeco MBE system, and for all the helps regarding the MBE growth and my projects.

Thanks to all my friends for supporting me through all the difficulties, for bring me endless joy. I will always remember the burger nights at Blu Wolf Bistro drinking the "good" tequila with Michael Fanto and Zihao Wang, the mornings playing basketball and jogging around the campus with Xinye Chen, the days looking up at the galaxy and shooting arrows with Peichuan Yin, the weekends playing Tak and VR games with Brian Daly and Sarah Daly…

I also want to thank my dog, the “drama queen”, Polymer, to bring me a lot of pleasure and “nightmare”.

I also greatly appreciate the funding support from RIT microsystems Engineering Program, National Science Foundation, and Office of Naval Research.

CONTENTS

LIST OF TABLES **ix**

LIST OF FIGURES **x**

CHAPTER 1: Introduction of III-Nitride Deep-Ultraviolet Light-Emitting Diodes **1**

- **1.1 Applications of UV Light** **1**
- **1.2 Nitride Semiconductor for DUV LEDs** **4**
  - 1.2.1 Fundamentals of III-Nitride Materials 5
  - 1.2.2 Basics of LEDs 7
- **1.3 Current Status of DUV LEDs** **11**
  - 1.3.1 Challenges for DUV LEDs 11
  - 1.3.2 Radiative Recombination Efficiency 13
  - 1.3.3 Light Extraction Efficiency 15
  - 1.3.4 Current Status of DUV LEDs 16
- **1.4 Optical Polarization from DUV LEDs** **17**
- **1.5 Motivation of This Work** **20**

CHAPTER 2: Basic and Challenges of III-Nitride Deep-Ultraviolet Light-Emitting Diodes **29**

- **2.1 Radiative Recombination Efficiency from Conventional AlGaN QWs** **30**
- **2.2 Carrier Injection Efficiency from Conventional AlGaN QW** **34**
  - 2.2.1 Model of Current Injection Efficiency for AlGaN LEDs 34
  - 2.2.2 Current Injection Efficiency from conventional AlGaN QW LEDs 36
- **2.3 Light Extraction Efficiency from Conventional AlGaN QW** **39**
- **2.4 Summary** **41**

CHAPTER 3: Optical Polarization from AlGaN-Based Deep-Ultraviolet Light-Emitting Diodes **43**

- **3.1 Factors Influencing the Light Polarization Switching in AlGaN Layer** **44**
  - 3.1.1 Strain State of the AlGaN Layers 44
  - 3.1.2 Quantum Confinement in AlGaN QWs 45
  - 3.1.3 Other Factors 47

3.2 Effect of QW Thickness on the Optical Polarization of AlGaN-Based DUV LEDs 47

CHAPTER 4: Design Analysis of Al(In)GaN-Delta-GaN for Deep-Ultraviolet Emitters 62

4.1 Engineer of AlGaN-Delta-GaN QW for UV Emitters 63
- 4.1.1 Concept and Valence Band Structures of AlGaN-Delta-GaN QW 63
- 4.1.2 Optical Characteristics of AlGaN-Delta-GaN QW 66
- 4.1.3 Engineering of AlGaN-Delta-GaN QW 69
- 4.1.4 AlGaN-Delta-GaN QW for laser applications 71

4.2 Proposal and Physics of AlInN-Delta-GaN QW UV Lasers 72
- 4.2.1 Concept and Valence Band Structures of AlInN-Delta-GaN QW 73
- 4.2.2 Optical Properties of AlInN-Delta-GaN QW 76

4.3 Summary 79

CHAPTER 5: Polarization Properties of AlN-Delta-GaN Quantum Well Ultraviolet Light-Emitting Diodes 84

5.1 Physics and Optical Properties from AlN-Delta-GaN QW UV LEDs 85
- 5.1.1 Physics of AlN-delta-GaN QWs for deep- and mid-UV emissions 85
- 5.1.2 Optical Properties of MBE-grown AlN-delta-GaN QW UV LEDs 89

5.2 Polarization Properties from AlN-Delta-GaN QW UV LEDs 91
- 5.2.1 Optical polarization measurements setup 91
- 5.2.2 Optical polarization from AlN-delta-GaN QW UV LEDs 93

5.3 Summary 97

CHAPTER 6: MBE Growth of AlGaN-Delta-GaN Quantum Wells 101

6.1 Concept and Physics of 260-nm AlGaN-delta-GaN Quantum Well 103

6.2 MBE-grown 260-nm AlGaN-delta-GaN Quantum Well 104

6.3 Characterizations of MBE-grown 260-nm AlGaN-delta-GaN Quantum Well 106
- 6.3.1 Structural properties from the MBE-grown AlGaN-delta-GaN QW 106
- 6.3.2 High Internal Quantum Efficiency from the MBE-grown AlGaN-delta-GaN QW 108

6.4 Summary 110

CHAPTER 7: Concepts for Improving DUV Light-Emitting Diodes Efficiency 115

7.1 Light Extraction Properties of the UV LEDs with Self-Assembled Microsphere Arrays 115
- 7.1.1 Experimental setup and results discussion 116
- 7.1.2 Physics and Simulation results 118

7.2 The Use of AlGaN Substrates for DUV Emissions 122
- 7.2.1 Physics and Simulation results 124
- 7.2.2 Summary 130

7.3 Current Spreading Layer Based on Nanosphere Lithography 131

7.4 III-Nitride Top-Down Nanowire LEDs 134

CHAPTER 8: Future Work 143

8.1 AlGaN-delta-GaN QW UV LEDs Epitaxy 144

8.2 Top-Down Nanowire DUV LEDs 145

8.3 Current Spreading DUV LEDs 146

APPENDIX A. Material Parameters for GaN and AlN 148

APPENDIX B: Numerical Simulation for Optical Properties of III-Nitride Quantum Wells 151

B.1 *k·p* Method for Strained Wurtzite Semiconductors 151
- B.1.1 Kane's Model for Wurtzite Semiconductors 152
- B.1.2 **k·p** Method for Strained Wurtzite Semiconductors 156

B.2 Self-Consistent 6-Band *k·p* Model for III-Nitride Band Structure Calculations 164
- B.2.1 Incorporation of Spontaneous and Piezoelectric Polarization Fields 164
- B.2.2 Carrier Screening Effect and Calculation Flowchart 165

B.3 Spontaneous Radiative Recombination Rate and Optical Gain of Strained Wurtzite III-Nitride QW 167

LIST OF TABLES

Table 1.1: Calculated square of the transition matrix element of GaN and AlN for light polarized parallel and perpendicular to the **c**-axis *[1]*. 19

Table 2.1: Values of Al contents (***x***) in $Al_xGa_{1-x}N$ wells and (***y***) in $Al_yGa_{1-y}N$ barriers [3] 37

Table 7.1: Refractive index and absorption coefficient used in the simulations...........119

Table A.1: Polarization and Bandgap of $In_xGa_{1-x}N$, $Al_xGa_{1-x}N$, and $Al_xIn_{1-x}N$ [2].......149

LIST OF FIGURES

Figure 1.1: The electromagnetic spectrum showing the ultraviolet radiation...................1

Figure 1.2: Applications of UVA, UVB, and UVC LEDs [1]. 3

Figure 1.3: Bandgap vs. lattice constant for common semiconductor materials. (www.seas.ucla.edu) 4

Figure 1.4: (a) GaN wurtzite structure (https://en.wikipedia.org/wiki/Gallium_nitride); (b) Polarization fields in strained GaN/AlN heterostructure....................................6

Figure 1.5: Reported external quantum efficiencies for III-nitride quantum well LEDs emitting in the UV spectral range [1]. 11

Figure 1.6: Methodology used in this work. 22

Figure 2.1: Efficiency components and loss mechanisms in UV LEDs.........................29

Figure 2.2: (a)TE- and TM-polarized $\mathbf{R_{sp}}$, as well as degree of polarization (DOP) at different wavelength; (b) band energy lineups with ground state wave functions and valence band structures from the conventional 3-nm $Al_{0.8}Ga_{0.2}N$ QW, $Al_{0.7}Ga_{0.3}N$ QW, $Al_{0.5}Ga_{0.5}N$ QW. 32

Figure 2.3: (a) Radiative recombination efficiency from the conventional AlGaN QW at different wavelength with different carrier densities n = 5×10^{18} cm^{-3}(black), n = 1×10^{19} cm^{-3}(red), n = 5×10^{19} cm^{-3}(blue); (b) Radiative recombination efficiency from the conventional AlGaN QW at different wavelength with different C values of 1×10^{-34} cm^6/s -1×10^{-30} cm^6/s; (c) Radiative recombination efficiency from the conventional AlGaN QW at different wavelength with different A values of $\mathbf{A}$ = 1×10^{6} s^{-1} - $\mathbf{A}$ = 1×10^{8} s^{-1}...33

Figure 2.4: (a) Carrier injection efficiency from AlGaN QW LEDs at different wavelength; inset: Schematic illustration of carrier injection model (b) carrier injection efficiency from the conventional AlGaN QW at 230 nm with different C values of 1×10^{-34} cm^6/s -1×10^{-30} cm^6/s; (c) carrier injection efficiency from the conventional AlGaN QW at 230 nm with different A values of **A** = 1×10^6 s^{-1} - **A** = 1×10^8 s^{-1}. 37

Figure 2.5: (a) schematic of the FDTD simulated bottom-emitting AlGaN-based QW DUV LEDs (b) TE- and TM-polarized light extraction efficiencies and light radiation patterns from AlGaN-based DUV LEDs at different emission wavelengths. 40

Figure 2.6: (a) TE- (black) and TM- (red) light extraction efficiency from conventional top-emitting AlGaN QW at different emission wavelengths (b) radiative recombination efficiency, effective light extraction efficiency and external quantum efficiency from conventional bottom-emitting AlGaN QW at different emission wavelengths. 41

Figure 3.1: Schematic of band structures for (a) strained $Al_xGa_{1-x}N$, (b) strained $Al_xGa_{1-x}N$ on AlN, (c) $Al_xGa_{1-x}N$/AlN QWs near the Γ point [5]. 45

Figure 3.2 : Critical Al-content where valence subbands crossover occurs with (red) and without (black) Electric field. Inset: Band-edge energies of AlN and high Al-content AlGaN Wurtzite semiconductors. 49

Figure 3.3: (a) critical Al-content (black) and critical emission wavelength (red) where TE-$\mathbf{R_{sp}}$=TM- $\mathbf{R_{sp}}$ as a function of QW thickness. (b) Comparison between $\mathbf{R_{sp}}$ crossover (black) and valence subbands crossover. 50

Figure 3.4: (a) Band structure and wavefunctions (b) envelope wavefunctions of the highest three subbands (c) valence band structure near *Γ* point (d) TE- (solid) and TM-polarized (dash) square of momentum matrix elements from C1-CH1, C1-HH1, C1-LH1 transitions for 1.5-nm $Al_{0.75}Ga_{0.25}N$ QW..51

Figure 3.5: (a) Band structure and wavefunctions (b) envelope wavefunctions of the highest three subbands (c) valence band structure near ***Γ*** point (d) TE- (solid) and TM-polarized (dash) square of momentum matrix elements from C1-CH1, C1-HH1, C1-LH1 transitions for 3-nm $Al_{0.73}Ga_{0.27}N$ QW...53

Figure 3.6: Momentum matrix element ratio between C-CH1 and C-HH1 as a function of QW thickness at the valence subbands crossover point (black) and the critical Al-content difference between $\mathbf{R_{sp}}$ crossover (x_1) and valence subbands crossover (x_2): $\Delta x = x1 - x2$ as a function of QW thickness (red). 54

Figure 3.7: Reported light polarization properties from AlGaN-based UV emitters with different QW thickness, categorized by Al-content [4], [5], [8], [9], [15], [16], [19]–[28]. 56

Figure 3.8: Reported light polarization properties from AlGaN-based UV emitters with different QW thickness, categorized by wavelength [4], [5], [8], [9], [15], [16], [19]–[28]. 57

Figure 4.1: Schematic illustration of AlGaN-delta-GaN QW structure. $\mathbf{d_1}$, $\mathbf{d_2}$ and **d** stands for the thicknesses of 1st and 2nd AlGaN sub-QW regions and delta-GaN layer 64

Figure 4.2: Band energy lineups with electron and hole wave functions of (a) $Al_{0.8}Ga_{0.2}N$-delta-GaN QW with 3-Å delta-GaN, and (b) 3-nm $Al_{0.65}Ga_{0.35}N$ QW;

Valence band structures of (c) $Al_{0.8}Ga_{0.2}N$-delta-GaN QW with 3-Å delta-GaN, and (d) 3-nm $Al_{0.8}Ga_{0.2}N$ QW. Carrier density is **n** = 5 × 10^{18} cm^{-3}. 66

Figure 4.3: (a) Polarized spontaneous emission spectra from the $Al_{0.8}Ga_{0.2}N$-delta-GaN QW with 3-Å delta-GaN and the 3-nm $Al_{0.8}Ga_{0.2}N$ QW at carrier density of **n** = 5 × 10^{18} cm^{-3}; spontaneous emission spectra from the $Al_{0.8}Ga_{0.2}N$-delta-GaN QW with different carrier density of **n** = 1 - 5 × 10^{18} cm^{-3} (dash line); (b) $\mathbf{R_{sp}}$ (black) and radiative recombination efficiency (red) as a function of carrier density for the $Al_{0.8}Ga_{0.2}N$-delta-GaN QW (solid line) and the $Al_{0.65}Ga_{0.35}N$-delta-GaN QW (dash line) 68

Figure 4.4: $\mathbf{R_{sp}}$ values and emission wavelengths from AlGaN-delta-GaN QWs with different delta-GaN thicknesses (red) from **d** = 3 – 15 Å and different sub-QW Al-contents (black) from **x** = 0.6 – 0.8. Carrier density is **n** = 5 × 10^{18} cm^{-3}. 71

Figure 4.5: TE-polarized optical gain spectra (black lines) from $Al_{0.8}Ga_{0.2}N$-delta-GaN QW with 3-Å delta-GaN (solid) and $Al_{0.7}Ga_{0.3}N$-delta-GaN QW with 3-Å delta-GaN (dash), carrier density is **n** = 5 × 10^{19} cm^{-3}. Peak TE-polarized gain as a function of carrier density up to **n** = 5 × 10^{98} cm^{-3} (red). 72

Figure 4.6: Energy band lineups for the (a) 24-Å AlInN-delta-GaN QW; (b) 24-Å conventional AlGaN QW; (c) 24-Å staggered AlInN QW with ground state electron wavefunction ($\boldsymbol{\psi_{e1}}$) and hole wavefunction ($\boldsymbol{\psi_{hh1}}$). Valence band structure for the (d) 24-Å AlInN-delta-GaN QW; (e) 24-Å conventional AlGaN QW; (f) 24-Å staggered AlInN QW at room temperature. The carrier density is 5×10^{19} cm^{-3}. 75

Figure 4.7: TE-polarized (solid line) and TM-polarized (dash line) optical gain spectra of 24-Å conventional AlGaN QW, 24-Å AlInN-delta-GaN QW and 6-Å $Al_{0.91}In_{0.09}N$/ 12-Å $Al_{0.82}In_{0.18}N$/ 6-Å $Al_{0.91}In_{0.09}N$ QW. The carrier density is 5×10^{19} cm^{-3}. 77

Figure 4.8: TE-polarized optical gain spectra of 24-Å AlInN-delta-GaN QW with the delta-GaN layer thickness of 3 Å to 27 Å. The carrier density is 5×10^{19} cm^{-3}.........78

Figure 4.9: (a) TE-polarized optical gain spectra of 24-Å AlInN-delta-GaN QW and 24-Å conventional AlGaN QW for carrier density from 1×10^{19} cm^{-3} to 6×10^{19} cm^{-3}. (b) TE-polarized peak gain as a function of carrier density for 24-Å AlInN-delta-GaN QW and 24-Å conventional AlGaN QW. 79

Figure 5.1: (a) Band structure transitioned from $Al_{0.7}Ga_{0.3}N$-delta-GaN QW to AlN-delta-GaN QW, showing that the use of AlN sub-QW layer is to replace the AlGaN sub-QW region; Energy band lineups for the (b) AlN-delta-GaN QW with delta-GaN thickness of **d** = 11 Å; (c) 30-Å conventional $Al_{0.35}Ga_{0.65}N$ QW with ground state electron wave function (ψ_{e1}), heavy hole wave function (ψ_{hh1}) and electron and hole wave functions overlap ($\boldsymbol{\Gamma e1 - hh1}$). Carrier density is **n** = 5 × 10^{18} cm^{-3}.....86

Figure 5.2: TE- (black) and TM-polarized (red) Spontaneous emission spectra of AlN-delta-GaN QWs with delta-GaN thickness of **d** = 3 - 11 Å at a carrier density of **n** =5×10^{18} cm^{-3}. Inset (a): Valence band structure from the AlN-delta-GaN QWs with **d** = 3 Å. (b) Total $\mathbf{R_{sp}}$ as a function of carrier density for AlN-delta-GaN QW with **d** = 11 Å (black) and 3-nm $Al_{0.35}Ga_{0.65}N$ QW (red). 88

Figure 5.3: (a) Schematic of MBE-grown AlN-delta-GaN QW UV-LED heterostructure and cross-sectional TEM image of the active region. The thickness of the delta-GaN region is 3-4 monolayer (ML). (b) Integrated EL intensity as a function of current

density. Inset: EL spectra from the AlN/GaN QW-like LED with different current densities (**j** = 2 – 23 A/cm^2)...90

Figure 5.4: Schematic of the MBE-grown AlN-delta-GaN QW LEDs and cross-sectional TEM images of the active regions. Normalized EL spectra from AlN-delta-GaN QW LEDs with current density of **j**=16.67 A/cm^2. (Inset) Output power as a function of current density up to **j** = 40 A/cm^2 from AlN-delta-GaN QW LEDs. The TEM images are taken from figure.2d and 2e of reference [6]. 91

Figure 5.5: (a) Schematic of the polarization-dependent EL measurements setup. (b) Schematic illustration of the polarization-dependent measurements 93

Figure 5.6: Polarization-dependent EL spectra from the 298-nm AlN-delta-GaN QW UV LED at (a) **θ** = 30° and (b) **θ** = 45° with current density of 40 A/cm^2........................94

Figure 5.7: Polarization-dependent EL spectra from the (a)-(b) 234-nm and (c)-(d) 246-nm AlN-delta-GaN QW UV LEDs at θ=30° and θ=45°...95

Figure 5.8: FDTD simulated and measured light radiation patterns of the (a) 234 nm, and (b) 246 nm AlN-delta-GaN UV LEDs..96

Figure 6.1: Spontaneous emission recombination rate per unit volume (**R$_{sp}$**) for 30-Å $Al_{0.9}Ga_{0.1}N$/5-Å GaN QW, 30-Å $Al_{0.7}Ga_{0.3}N$/3-Å GaN QW, and AlGaN QWs with QW thickness of 2 nm, 2.5 nm and 3 nm at room temperature. The carrier density is n = 5×10^{18} cm^{-3}; Spontaneous emission spectra, band lineups and wave functions from $Al_{0.9}Ga_{0.1}N$-delta-GaN QW and 3-nm $Al_{0.58}Ga_{0.42}N$ QW.............................104

Figure 6.2: Schematic of the structure with 5 periods of $Al_{0.9}Ga_{0.1}N$-delta-GaN QWs, RHEED patterns before, during and after the active region growth; flux control during the active region growth..106

Figure 6.3: ω-2θ HR-XRD spectra for (a) $Al_{0.9}Ga_{0.1}N$-delta-GaN QW and (b) $Al_{0.9}Ga_{0.1}N$ QW, showing the formation of $Al_{0.9}Ga_{0.1}N$ and 2 ML GaN layers. Inset: AFM image after the $Al_{0.9}Ga_{0.1}N$-delta-GaN active region growth 107

Figure 6.4: STEM images of (a) $Al_{0.9}Ga_{0.1}N$-delta-GaN QW and (b) 3-nm $Al_{0.9}Ga_{0.1}N$/3-nm AlN QW heterostructure. 108

Figure 6.5: Photoluminescence (PL) spectra from (a) $Al_{0.9}Ga_{0.1}N$-delta-GaN QW and (b) 3-nm $Al_{0.6}Ga_{0.4}N$/3-nm AlN QW at low and room temperature; (c) IQE value from $Al_{0.9}Ga_{0.1}N$-delta-GaN QW as a function of laser energy; (d) Reported IQE value from DUV LEDs at different wavelengths 110

Figure 7.1: (a) Schematic of 280-nm UV LED heterostructure (b) Experimental setup for measurement of light emission from the LED device, showing the commercial UV LED beneath sphere coated sapphire. (c) SEM image of the close-packed microsphere array deposited on sapphire. (d) Schematic representation of the angle dependent EL setup used to measure light extraction and far field radiation patterns of the device. 117

Figure 7.2: (a) Integrated EL intensity as a function of current for the structure with microsphere arrays (black) and without microsphere arrays (red) Inset: EL spectra of the structures with (black) and without (red) the 700-nm microspheres array at θ = 0°. (b) Light radiation pattern from the structures with microsphere arrays (black) and without microsphere arrays (red), showing the EL intensity enhancements at small angles θ < 30°. 118

Figure 7.3: Cross-sectional electric field maps produced by FDTD simulation for the structures without spheres, with 280 nm spheres, 500 nm spheres and 700 nm spheres. 120

Figure 7.4: Polarized light radiation patterns produced by FDTD simulation for the structures without spheres, with 280 nm spheres, 500 nm spheres and 700 nm spheres. 121

Figure 7.5: (a) In-plane ($\varepsilon_{xx}/\varepsilon_{yy}$) strains in the active region as a function of Al-content (x) in the $Al_xGa_{1-x}N$ QW. Band energy lineups with ground state electron and hole wave functions from (b) $Al_{0.48}Ga_{0.52}N/Al_{0.72}Ga_{0.28}N$ QW on $Al_{0.72}Ga_{0.28}N$ substrate and (c) $Al_{0.51}Ga_{0.49}N$/AlN QW on AlN substrate. 125

Figure 7.6: (a) TE-polarized (blue), TM-polarized (red) and total (black) spontaneous emission rate per unit volume (**R_{sp}**) as a function of carrier density from $Al_{0.48}Ga_{0.52}N/Al_{72}Ga_{28}N$ QW (solid line) and $Al_{0.51}Ga_{0.49}N$/AlN QW (dash line). (b) TE- (blue) and TM-polarized (red) peak optical gains from $Al_xGa_{1-x}N/Al_yGa_{1-y}N$ QW with different substrate/barrier Al-contents (y) for 260-nm emissions. (c) TE-polarized (blue), TM-polarized (red) and total (black) **R_{sp}** from $Al_xGa_{1-x}N/Al_yGa_{1-y}N$ QW with different substrate/barrier Al-contents (y) for 260-nm emissions. (d) Radiative recombination efficiencies at different SRH coefficient (A) levels from $Al_xGa_{1-x}N/Al_yGa_{1-y}N$ QW on different substrate/barrier Al-contents for 260-nm emissions. Carrier density level from the simulations is $n = 5 \times 10^{19}$ cm^{-3}. 126

Figure 7.7: (a) Critical Al-content at which HH and CH subbands have same energy level (solid line) and QW Al-contents for 240nm, 250 nm and 260 nm emissions (dash lines); TE-polarized (blue) and TM-polarized (red) peak optical gains from

$Al_xGa_{1-x}N/Al_yGa_{1-y}N$ QW on different substrate/barrier Al-contents for (b) 250-nm and (c) 240-nm emissions with carrier density of n = 5 × 10^{19} cm^{-3}. 130

Figure 7.8: Fabrication process flow of sphere current spreading LEDs. 132

Figure 7.9: SEM images of sphere current spreading LEDs.......................................133

Figure 7.10: (a) Photos of the glass slides with silver continuous film or sphere CSL, transmissivity of the glass slides with 20-nm and 50-nm sphere CSL at normal incident. (b) EL intensity from the green LEDs with and without sphere CSL. 134

Figure 7.11: (a) SEM images of GaN nanowires with different geometry (b) SEM image of nanowire LED by using nanosphere lithography showing nonuniform coating. (c) SEM image of nanowire green LED by using Heiderburg laser writer.................135

Figure 7.12: Process flow of nanowire LED fabrication 136

Figure 8.1: SEM images of AlGaN-based DUV LEDs after KOH wet etch at different times. 146

Figure B.1: The band-edge energies for wurtzite GaN (a) without spin-orbit interaction; (b) with spin-orbit interaction [2]. 155

Figure B.2: Numerical simulation flow chart for the self-consistent 6-band **k·p** model for wurtzite QW structure. 167

CHAPTER 1: Introduction of III-Nitride Deep-Ultraviolet Light-Emitting Diodes

1.1 Applications of UV Light

Ultraviolet (UV) light is a form of electromagnetic radiation with a wavelength shorter than that of visible light but longer than X-rays, typically in the range of 10 nm to 400 nm, as shown in figure 1.1. UV radiation is usually generated by either very hot objects, such as sun or electric arcs like mercury-vapor lamps. Based on the radiation wavelength and their applications, the UV spectrum can be further subdivided into Vacuum UV (10 nm – 200 nm), UVC (100 nm – 280 nm), UVB (280 nm – 315 nm) and UVA (315 nm – 400 nm) regimes [1]. In some research area, UVC, UVB, and UVA are also named as deep-UV (DUV), mid-UV, and near-UV, respectively.

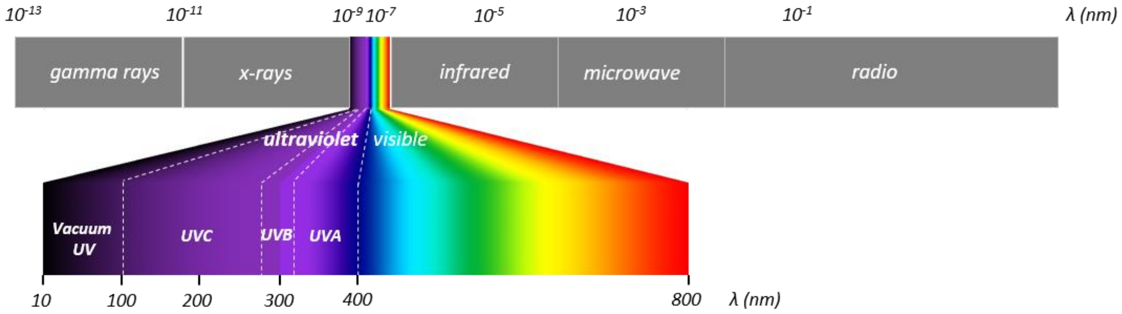

***Figure 1.1**: The electromagnetic spectrum showing the ultraviolet radiation*

The uses for UV light include a broad range of applications in industrial, commercial and military. For example, vacuum UV light is strongly absorbed by oxygen molecules in the air, but the end of the spectrum, with wavelengths of 150 nm – 200 nm, can propagate through a nitrogen environment. Therefore, a significant example is the 193-nm photolithography equipment, which is developed in this spectral range by operating in an oxygen-free atmosphere [2]. For even shorter emission wavelengths, such as Extreme UV (EUV: 10 nm – 100 nm), scientists invented a technology to reflect EUV radiation and utilize it to make telescopes for solar imaging, as well as EUV photolithography equipment [2], [3].

Compared to the Vacuum UV regime, considerable applications are realized in the range of 200 nm - 400 nm. UV light with lower photon energies (UVA and UVB) can trigger some chemical reactions, such as polymerization process during UV radiation curing. Specifically, a photoinitiator can be cleaved into free radicals after exposed in UV radiation. Those radicals then attack the monomer and oligomer molecules and initiate polymerization [1]. Therefore, such UV radiations are usually used for curing, for example, a curing step is necessary in most packaging in supermarkets [1]. Besides, high volume applications like coating, printing, sensing, and applications like blood gas analysis were realized in UVA regime, while phototherapy [4], as well as plant lightning [5] were utilizing UVB spectrum.

Besides being used to trigger chemical reaction, UV light can also destroy chemical bonds. The nucleotides, by which DNA and RNA are built up, are composed of backbone and nucleobases. Under the exposure of UVC light, a chemical bond can be formed between the adjacent bases, which disrupt the DNA/RNA replication [1], [6]–[8]. Therefore, UVC light is widely utilized in water purification, food sterilization, medical disinfection [1]. Additional applications for UVC radiation can be found in air communication [9] and the area of sensing [10]. Figure 1.2 summarizes applications for each UV radiation wavelength regime.

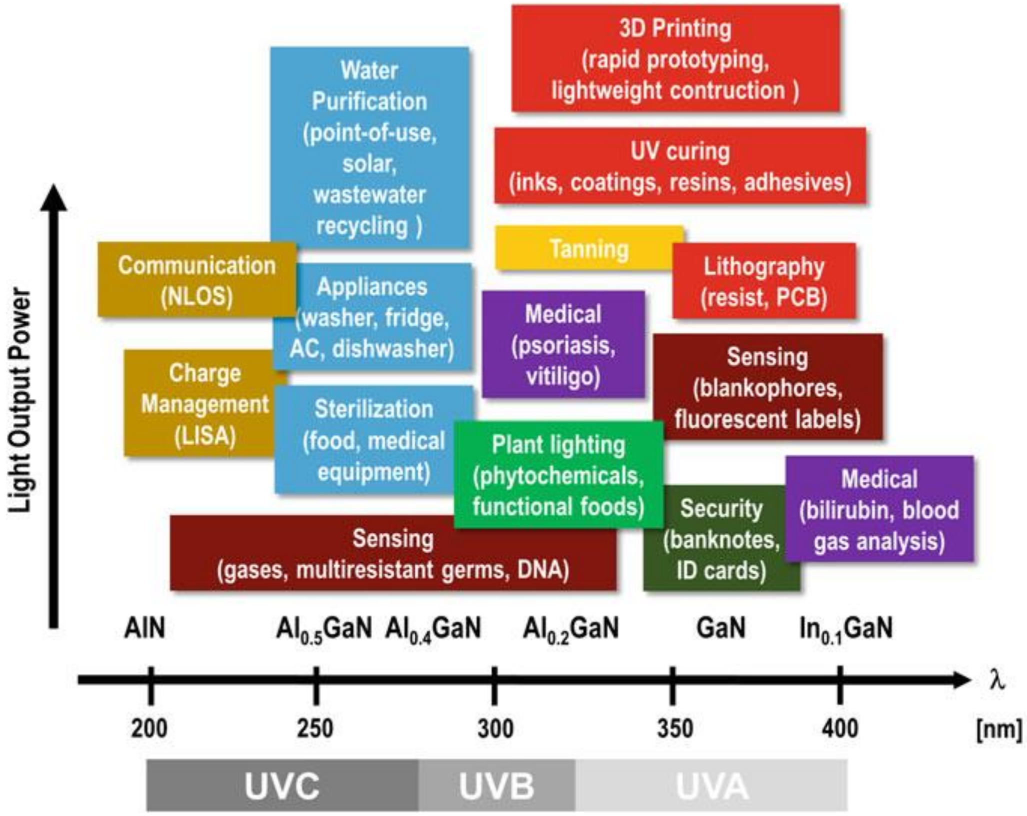

***Figure 1.2**: Applications of UVA, UVB, and UVC LEDs [1].*

Based on the variety of applications, the demand for UV products rapidly increases. The global UV LED market is projected to boost from $288 million in 2017 to $526 million in 2020 [11]. Up to now, conventional UV light sources, such as low- and medium-pressure mercury lamps still occupy most of the market. However, these UV sources have a large number of drawbacks and are gradually being replaced by UV Light-Emitting Diodes (LEDs), which have already taken 34.7% of the market in 2017 (vs. 12.7% in 2012) [12]. Compared to conventional UV sources, UV LEDs offer several advantages, such as compact size, long lifetime, and high-power efficiency. Most importantly, the emission wavelength can be engineered to desired regime, which together with the rapid switching ability could unlock several new applications for UV light, like high-sensitivity advanced sensing [1].

1.2 Nitride Semiconductor for DUV LEDs

To realize UV emissions from LEDs, Ultra-Wide-Bandgap (UWBG) materials are necessary. However, only a few semiconductors meet the requirements, such as AlInGaN, β-Ga_2O_3, ZnO, and diamond [13], [14]. Figure 1.3 shows the energy bandgap versus lattice constant for common semiconductor materials. Among all the candidates, III-nitride materials including binary, ternary and quaternary compounds are elite options for UV LEDs not only because their bandgaps could cover entire UV-Vis-IR regime (210 nm – 1850 nm), but the capability of using heterostructure designs enables them for high-efficiency quantum devices. Simply by changing the Al-content (or In-content) in the structure, the emission wavelength can be engineered to the target regime. In addition, as compared to other UWBG materials, Al(In)GaN is more mature in both laboratories and industries for LEDs applications. The success of efficient III-nitride blue LEDs could provide an extremely useful guide for III-nitride UV LED development.

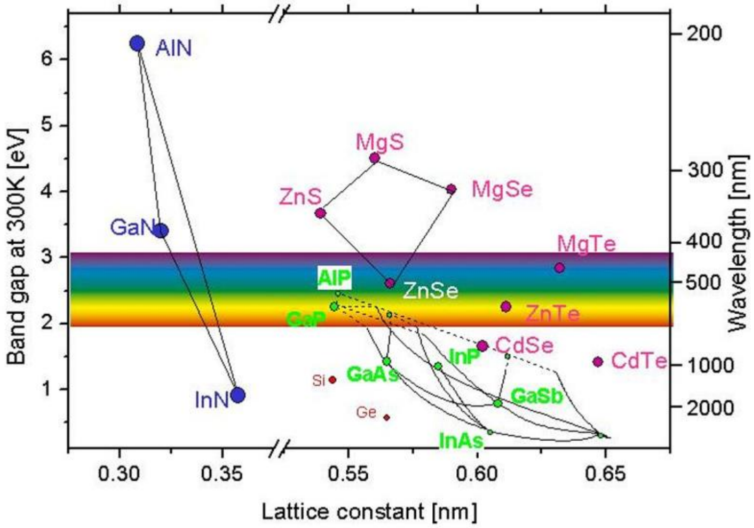

***Figure 1.3**: Bandgap vs. lattice constant for common semiconductor materials.*

(www.seas.ucla.edu)

1.2.1 Fundamentals of III-Nitride Materials

Unlike silicon and other III-V compounds, III-nitride materials including AlN, GaN, InN and their ternary/quaternary alloys are thermally stable in wurtzite form. This hexagonal close-packed structure provides several unique properties, such as high heat capacity and thermal conductivity. GaN is the most heavily studied III-nitride material although it is still relatively unknown compared to other III-V semiconductors. The lattice constants for GaN are reported as a = 3.189 Å and c = 5.185 Å [1], [15]. Therefore, one of the major issues for III-nitride materials is the lack of an ideal substrate that is both lattice and thermally matched. A lot of substrates have been utilized for III-nitride applications, such as silicon carbide, aluminum nitride, silicon, sapphire, and magnesium oxide [15]. Among all the substrates, sapphire is the most popular choice because it is stable at high temperatures, widely available, and hexagonally symmetric. However, the thermal and lattice mismatch between sapphire and III-nitride materials lead to poor material quality with large dislocation densities of 10^{10} cm^{-2}. This strongly influences the device performance such as the internal quantum efficiency in III-nitride LEDs [1]. Another unique property of III-nitride materials is the high background electron concentration attributed to nitrogen vacancies [1], [15]. After many years of effort, the background electron concentration has been reduced to 4×10^{16} cm^{-3} [15]. However, it is still difficult to achieve p-type materials with high doping levels due to the high activation energy of acceptors such as Mg and Zn [1], [15], [16]. In addition, even Si n-type doping becomes difficult in high Al-content AlGaN layers, which will cause a large voltage drop outside the active region and limit the carrier injection efficiency in III-nitride LEDs.

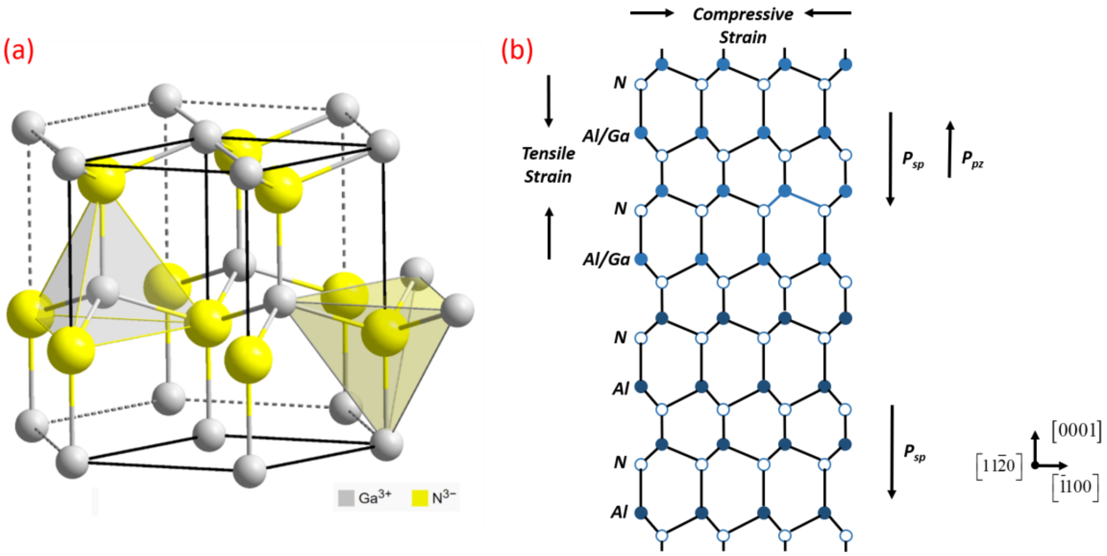

***Figure 1.4**: (a) GaN wurtzite structure (https://en.wikipedia.org/wiki/Gallium_nitride); (b) Polarization fields in strained GaN/AlN heterostructure.*

For wurtzite III-nitride material, such as GaN shown in figure 1.4 (a), each Ga atom is bonded to four N atoms. Due to the large electronegativity difference between the two atoms, each Ga-N bond is partly ionic and the electrons are pulled more towards N atom. As a result, a dipole moment is formed at each Ga-N bond. Because of the non-centrosymmetric wurtzite structure, these dipole moments cannot be canceled out like in other symmetric zinc-blende structures. This results in a net polarization along the <0001> orientation (***c***-axis), known as spontaneous polarization ($\boldsymbol{P_{SP}}$). For III-nitride ternary alloys, the spontaneous polarization follows the linear relationship and is summarized in Appendix A. Besides the spontaneous polarization, another polarization called piezoelectric polarization ($\boldsymbol{P_{PZ}}$) can be found in strained III-nitride materials induced by the lattice mismatch. For example, GaN has a larger in-plane lattice constant than that of AlN, which causes a compressive strain when GaN/AlGaN is grown on an AlN substrate. The induced piezoelectric polarization has the opposite polarity compared to the built-in spontaneous polarization, as illustrated in figure 1.4 (b). The total polarization field is then the sum of $\boldsymbol{P_{PZ}}$ and $\boldsymbol{P_{SP}}$, and determines the polarization charge density $\boldsymbol{\rho_{pol}}$ as:

$$\nabla P = \nabla \cdot (P_{PZ} + P_{SP}) = -\rho_{pol} \tag{1-1}$$

1.2.2 Basics of LEDs

A LED is a p-n junction that emits light when a positive voltage is applied across the junction. Specifically, minority carriers (electrons and holes) recombine in the p-n junction depletion region and produce photons whose wavelengths are determined by the energy bandgap of the semiconductor. The process is called electroluminescence. This section will develop a physical understanding of (i) Radiative and non-radiative recombination, (ii) current flow leading to light emission and quantum heterostructure in a LED, (iii) efficiency components of LEDs

(i) Radiative and non-radiative recombination

The recombination processes in LEDs can be either radiative or non-radiative, i.e. converted to phonons or wasted as heat. The former is clearly the preferred process for LED applications. Photons are generated during the process with emission wavelengths determined by material bandgap (E_g) follow the relationship: $\lambda = \frac{hc}{E_g} \approx \frac{1240}{E_g}\ nm.$ III-nitride semiconductors including GaN, AlN, and their ternary alloy AlGaN are direct bandgap materials. For direct bandgap material, whose minimal-energy state in the conduction band and minimal-energy state in the valence band are located at same ***k***-

vector in the Brillouin zone, the recombination processes from conduction band to valence band only generates photons.

In addition to the radiative recombination, there are several mechanisms in the structures which cause the non-radiative recombination such as defects, Auger recombination, and dangling bonds at the surface [17], [18]. Native defects in the semiconductor crystal structure like vacancies or interstitials induce energy levels which work as recombination centers within the gap of the semiconductor. Free carriers are captured by these traps and the issue becomes severe if the energy level is close to the middle of the forbidden gap. This non-radiative recombination was first studied by Shockley, Read and Hall and therefore named as SRH recombination. Note that not all of the defect-induced recombinations are non-radiative, some deep-level transitions are radiative. One example of a defect-induced radiative recombination is the yellow peak (~550 nm) in III-nitride materials, which is demonstrated to be related with Ga vacancies in the semiconductors, especially n-type [1].

For Auger recombination, instead of emitting photons, the energy generated by electron-hole recombination excites a free electron higher above the conduction band or a hole deeper past the valence band. It is demonstrated that the Auger recombination rate is proportional to the cubic of the carrier concentration, which indicates the Auger recombination influences device efficiency only at very high carrier injection current.

Non-radiative recombination can be also found at the semiconductor surface. Specifically, the atoms at the surface are either partially filled (dangling bonds) or rearranged and bonded with neighboring atoms due to the strong perturbation of the periodicity of the crystal. Both conditions will lead to new atomic structures with energy states located in the forbidden gap, which work as non-radiative recombination centers.

(ii) Current flow leading to light emission and quantum heterostructure in a LED

LEDs are based on standard p-n junctions, which have been widely discussed in most Semiconductor physics books [17], [18]. Under zero bias, a depletion region is formed in between the p-n junction where free carriers are depleted. In this region, the ionized donors and acceptors produce a built-in potential which makes the p-n junction highly resistive until forward biased. Once a positive voltage V is added on the p-side, the built-in potential barrier is lowered and the current flow starts to increase. Therefore, more carriers diffuse into the p-n junction and eventually recombine.

In simple p-n homojunctions, the mean distance of minority carriers diffusion is defined as diffusion length, which is a range up to 20 μm. This large diffusion length leads to a low carrier density for recombination and is the difficulty to realize high-efficiency LEDs since the recombination rate is strongly influenced by the carrier density. In contrast, the use of a double heterostructure, which consists of a small bandgap active region sandwiched by two large bandgap semiconductors, can significantly enhance the carrier density. This results in increased LED efficiency by confining minority carriers in the active region (0.01 – 1 μm) rather than the diffusion length. Moreover, the luminescence efficiency can be further enhanced by shrinking the active region below 10 nm, which is called a quantum well (QW).

(iii) Efficiency components of LEDs

There are many key metrics to evaluate the performance of LEDs. One of them is power efficiency, also called wall plug efficiency (WPE), which is defined as the ratio of the light output power versus the electrical input power:

$$WPE = \frac{P_{out}}{I \cdot V} = \eta_{EQE} \frac{\hbar\omega}{e \cdot V} \qquad \text{1-2}$$

In *Eq.* 1-2, $\boldsymbol{\eta_{EQE}}$ represents the external quantum efficiency, while $\boldsymbol{I}$ and $\boldsymbol{V}$ are drive current and operating voltage for the LED, and $\hbar\omega$ stands for the photon energy with $\hbar = 6.582 \times 10^{-16} eV \cdot s$. Note that the $\boldsymbol{\eta_{EQE}}$ is defined as the ratio of the number of UV photons emitted out of the device to the number of carriers injected into the device. $\boldsymbol{\eta_{EQE}}$ can be divided into three components, named as, light extraction efficiency ($\boldsymbol{\eta_{EXT}}$), radiative recombination efficiency ($\boldsymbol{\eta_{RAD}}$) and carrier injection efficiency ($\boldsymbol{\eta_{INJ}}$). The product of the η_{RAD} and the η_{INJ} is defined as internal quantum efficiency ($\boldsymbol{\eta_{IQE}}$ or IQE)

$$\eta_{EQE} = \eta_{IQE} \times \eta_{EXT} = \eta_{INJ} \times \eta_{RAD} \times \eta_{EXT}$$

$$\eta_{INJ} = \frac{\#\, of\ carriers\ reach\ the\ QW\ active\ region}{\#\, of\ carriers\ being\ injected\ into\ LED}$$

$$\eta_{RAD} = \frac{\#\, of\ radiative\ electron - hole\ recombination}{\#\, of\ total\ electron - hole\ pair\ recombineation}$$

$$\eta_{EXT} = \frac{\#\, of\ photons\ emitted\ from\ LED}{\#\, of\ photons\ generated\ in\ the\ active\ region} \qquad \text{1-3}$$

1.3 Current Status of DUV LEDs

1.3.1 Challenges for DUV LEDs

A large number of research groups have been engaged in AlGaN-based DUV LED research area during the past decade and reported encouraging/promising results. However currently, most of the reported DUV LEDs can only provide a few milliwatts of output power with lifetimes less than a thousand hours [1], [19]. One of the reasons is the low $\boldsymbol{\eta}_{\boldsymbol{EQE}}$, which is typically limited below 10% for DUV LEDs. As a comparison, the $\boldsymbol{\eta}_{\boldsymbol{EQE}}$ for visible LED has been reached 80% [20]. Figure 1.5 summarized the reported external quantum efficiencies for AlGaN, AlInGaN, and InGaN quantum well (QW) LEDs in the UV range. It is clear that the efficiency drops drastically as the emission wavelength decreases. There are many reasons limiting the efficiency of III-nitride LEDs, which will be detailed discussed in the following based on different efficiency components.

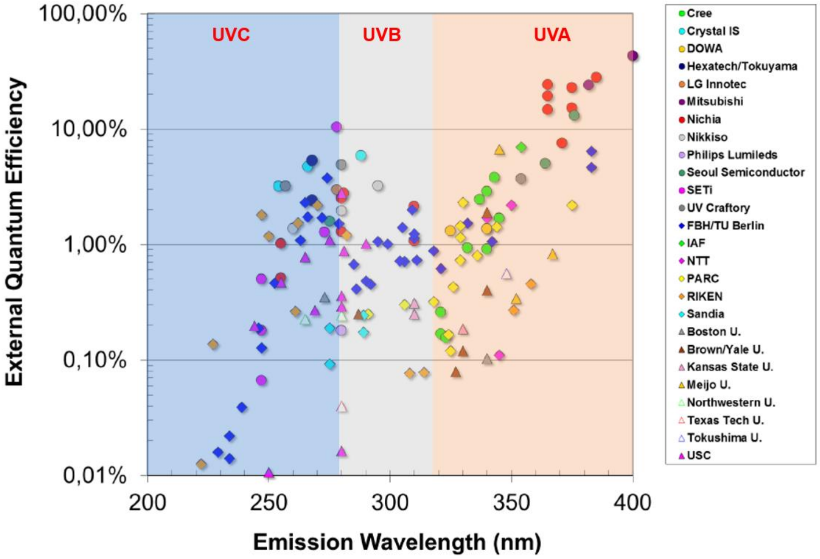

***Figure 1.5**: Reported external quantum efficiencies for III-nitride quantum well LEDs emitting in the UV spectral range [1].*

(i) Carrier Injection Efficiency

Efficient carrier injection is challenging for DUV LEDs, especially for devices with a high Al-content AlGaN layer. This is due to poor material doping level, electron overflow, and a Schottky contact. The Mg-doped p-AlGaN layer always shows a low conductivity because of the high activation energy of Mg acceptors (200-600 meV) [1], [15], [16]. Only a small fraction of the Mg acceptors can be ionized at room temperature (26 meV). Enormous efforts have been made to improve the doping level in the p-AlGaN layer and up to 10^{17} cm^{-3} hole concentration can be achieved [21]–[26]. However, the p-conductivity is still not sufficiently high to realize high-efficiency LEDs. Therefore, research groups use a p-GaN layer to reduce the p-resistivity, although it would sacrifice light extraction efficiency due to the optical absorption from the p-GaN layer. Meanwhile, several new techniques have been proposed and investigated to improve the p-contact, such as the use of short period $Al_xGa_{1-x}N/Al_yGa_{1-y}N$ superlattices [27], polarization-induced doping [28], alternative material such as p-hBN [14], [29] and Tunnel junctions [30], [31].

The electron overflow is another loss mechanism for the injection current [1], [18], [19]. As the voltage increases, the Fermi energy level will eventually rise to the top of the quantum well. As a result, the carrier concentration in the active region will not be further enhanced with injection current increases. More detailed discussion on the electron overflow and efficiency droop will be discussed in chapter 2. Previous theoretical studies show the electron overflow is more severe in structures with a thin QW region [18], [19]. Therefore, multiple quantum well active regions are incorporated to address this issue. In addition, utilizing electron-blocking layers (EBLs) [1], [32]–[37] can sufficiently prevent the electrons escaping from the active region although it sacrifices the hole injection efficiency.

Because of the wide bandgap of the AlGaN material, there is no suitable metal with desired work function to form ohmic contacts to both n- and p-AlGaN layers. The Schottky contacts with relatively large barriers introduce an additional voltage drop outside the active region. A number of studies have looked into lowering contact resistance by optimizing contact geometries and employing current spreading layers [1].

1.3.2 Radiative Recombination Efficiency

The radiative recombination efficiency is defined as the ratio of radiative recombinations versus the sum of radiative and nonradiative recombinations. In UV LED devices, SRH recombination and Auger recombination are two major components determining the nonradiative recombination rate (***R_{nr}***), which can be thereby estimated as:

$$R_{nr} = A \cdot n + C \cdot n^3 \tag{1-4}$$

where A and C donate the SRH recombination coefficient and Auger recombination coefficient respectively and. *n* is the carrier density in QW. Typical values for the Auger coefficient is in the range of 1×10^{-31} - 2×10^{-30} $cm^6 s^{-1}$ for blue-violet LEDs [1] while the value for DUV range is still under heavily debate. SRH coefficient is inverse proportional to the SRH recombination lifetime, which is strongly influenced by defect levels. Reported ***A*** value ranges from 1×10^6 - 1×10^{10} [1].

According to this definition, device radiative recombination efficiency can be enhanced by either increasing the spontaneous recombination rate ($\boldsymbol{R_{sp}}$) or limiting the non-radiative recombinations. $\boldsymbol{R_{sp}}$ can be simplified as $\boldsymbol{R_{sp}} = B \cdot n^2$ with the bimolecular recombination coefficient ($\boldsymbol{B}$) in the range of 2×10^{-10} $cm^3\,s^{-1}$, which strongly depends on the active region design and strain state of the AlGaN QW [1]. Specifically, DUV LED devices usually suffer from the quantum confined stark effect (QCSE) induced by the large built-in polarization electric fields in the active region. As a result, electron and hole wavefunctions are pushed to opposite sides of the QW region, which reduces the oscillator strength and $\boldsymbol{R_{sp}}$. Another issue limiting device $\boldsymbol{R_{sp}}$ is the valence band mixing effect in conventional AlGaN QWs [38]. It is well-reported that the light polarization from the AlGaN QW will switch from transverse-electric (TE) to transverse-magnetic (TM) with an increasing Al-content. This is due to the valence subbands such as the heavy hole (HH), light hole (LH), and crystal-field split-off hole (CH) rearrangement. These unique light polarization properties and complex valence band structures strongly influence the device $\boldsymbol{R_{sp}}$, which will be discussed in chapter 2 and 3. One possible solution to address the QCSE and valence band mixing effect is the use of delta-QW designs, such as AlGaN-delta-GaN [39], AlInN-delta-GaN, and AlN-delta-GaN QWs, as discussed in chapters 4-6.

Besides increasing the $\boldsymbol{R_{sp}}$ from the active region, the radiative recombination efficiency can be also improved by minimizing the nonradiative recombination, such as the dislocation density. Recently, several research groups reported the $\boldsymbol{\eta_{IQE}}$ can be increased from as low as 1% up to 60% by reducing the dislocation density down to 5×10^{8} cm^{-2} [35], [37], [40]. Therefore, high-quality substrate or other growth techniques have been developed for years to improve device IQE [1], including AlGaN ternary substrate, which will be discussed in chapter 7.

1.3.3 Light Extraction Efficiency

Light extraction efficiency is the biggest challenge for realizing high-efficiency DUV LEDs. For a single LED chip on the sapphire substrate, the light extraction efficiency is only in the range of 8% - 20%. This low $\boldsymbol{\eta_{EXT}}$ originates from the large refractive index contrast between AlGaN or sapphire, and air. Specifically, light traveling from one media to another should follow Snell's law, which is given as:

$$\vartheta_{crit} = arcsin\frac{n_0}{n_s} \qquad 1\text{-}5$$

where $\boldsymbol{\vartheta_{crit}}$ is the critical angle for internal reflection. In equation 1-5, $\boldsymbol{n_0}$ and $\boldsymbol{n_s}$ are the refractive indices of air and the semiconductor. Knowing the $\boldsymbol{\vartheta_{crit}}$ from top/bottom of the device, the the light extraction efficiency can be estimated as:

$$\eta_{EXT} = \frac{1}{2}(1 - \cos(\vartheta_{crit})) \qquad 1\text{-}6$$

For example, the refractive indices of sapphire and AlN are 1.81 and 2.28 at 300nm, which correspond to the critical angles of $\vartheta_{crit} = 33.5°$ and $\vartheta_{crit} = 26°$, respectively. As a result, only 8.3% and 5.1% of the photons can escape out of the LED devices [1]. In addition, the light extraction efficiency will be further reduced if the photons are TM-polarized, which prefers edge-emission. Note that there is no existing method to directly measure the light extraction efficiency from the device, however, the light radiation and extraction efficiency can be estimated by the use of finite difference time domain (FDTD) simulation.

During the past decades, researchers have been fully engaged in improving light extraction efficiency for DUV LEDs. Patterned sapphire substrates [41], [42], photonic crystal structures [41], and nanowire structure [43] have all been widely developed showing encouraging results.

1.3.4 Current Status of DUV LEDs

Currently, Al(In)GaN-based DUV LEDs with emission wavelengths of 222 nm - 351 nm have been rapidly developed. With the success of several fabrication techniques, up to 20% η_{EQE} has been realized [34].

To achieve such high η_{EQE}, high quality AlN/sapphire substrate with threading dislocation densities (TDD) of 10^8-10^9 cm^{-2} are required. Recently, H. Hirayama *et al.* developed an ammonia pulse-flow method to grow low-TDD, crack-free, stable, and flat substrates by Metal-Organic Chemical Vapor Deposition (MOCVD). Specifically, an AlN nucleation layer and a buried AlN layer were first deposited on the sapphire substrate by NH_3 pulsed-flow growth. This is followed by a high-growth-rate continuous-flow mode to smoothen the surface. By repeating the pulsed-flow growth mode and continuous-flow mode, eventually substrates with low edge- and screw-type dislocation densities of 5×10^8 and 4×10^7 cm^{-2} are achieved. Therefore, up to 60% internal quantum efficiency can be realized by the use of this type of substrate [35], [37].

In addition, H. Hirayama *et al.* also demonstrated the use of multiquantum-barrier (MQB) EBLs for carrier injection efficiency enhancement [33]. By replacing the single layer EBL, the structure with the MQB EBLs showed a 2.7-times enhancement in efficiency for 250 nm UV LEDs. This is due to the multi-reflection effects in the wave functions. The maximum power from the structures with MQB EBLs and with a single layer EBL are 4.8 mW at 135 mA and 2.2mW at 300 mA, respectively.

To improve the light extraction efficiency, H. Hirayama *et al.* utilized a transparent p-AlGaN layer and a highly reflective p-type electrode [34], [41], [44]. Specifically, a transparent p-AlGaN:Mg layer with Al-content of 65%, an Rh electrode, a patterned sapphire substrate (PSS), and encapsulation resin on a 275 nm UV LED. This resulted in a record 20.3% maximum external quantum efficiency from the device [34].

1.4 Optical Polarization from DUV LEDs

Polarization is a property applying to all transverse waves including the electromagnetic waves that specify the orientation of the oscillations. Based on different properties of the light wave, the optical polarization can be further broken down to circular polarization, elliptical polarization and linear polarization. This unique property leads to tremendous applications like polarized sunglasses, photography, display technology, which significantly change our daily life.

Optical polarization from DUV LEDs are also a hot topic and being realized and investigated. In this study, to be clear, we focus on the optical polarization properties from the active region, at which polarized photons generated. More specific, we investigate the generation and propagation of the TE- and TM-polarized photon in the

LED devices. Note that there are some linear polarization properties study in visible range, corresponding to the polarization along $\boldsymbol{x}$- and $\boldsymbol{y}$-axis, which usually strongly influences the efficiency from LED to waveguide.

As mentioned previously, III-nitride materials are thermally stabilized in the wurtzite phase, whose electrical and optical properties are mainly determined by the band structure at the Brillouin zone center ($\boldsymbol{k}$ = 0). At the zone center, the conduction band exhibits an atomic $\boldsymbol{s}$-orbital character while the valence band states have atomic p-orbital characters. Because of the reduced symmetry of the wurtzite crystal structure, III-nitride materials are anisotropic perpendicular and along the growth direction ($\mathbf{c}$-axis), which leads to a crystal field splitting ($\Delta_{\boldsymbol{cr}}$) of the valence band. As a result, the top of the valence band splits into a twofold degenerate state with $\boldsymbol{p_x}$ and $\boldsymbol{p_y}$-like character and a single degenerate state with $\boldsymbol{p_z}$-like character. With considering the spin-orbit interaction ($\Delta_{\boldsymbol{so}}$), the twofold degeneration state further separates into $\boldsymbol{\Gamma_9}$ and $\boldsymbol{\Gamma_7}$ states, named HH and LH, respectively. The $\boldsymbol{p_z}$-like state is called CH. The energy splitting in III-nitride materials based on the quasi-cubic model is expressed as:

$$\Gamma_9 - \Gamma_{7\pm} = \frac{\Delta_{cr} + \Delta_{so}}{2} \mp \sqrt{\left(\frac{\Delta_{cr} + \Delta_{so}}{2}\right)^2 - \frac{2}{3}\Delta_{cr}\Delta_{so}} \qquad \text{1-7}$$

For AlN, the negative $\Delta_{\boldsymbol{cr}}$ results in $\boldsymbol{\Gamma_9 < \Gamma_7}$ (CH subband on the top), whereas for GaN, $\Gamma_9 > \Gamma_7$ and topmost HH subband are realized because of the positive $\Delta_{\boldsymbol{cr}}$.

The light polarization is determined by the band-to-band transition involving the three valence subbands. Using the quasi-cubic model, the square of transition matrix elements of wurtzite GaN and AlN are summarized in table 1.1. The light polarized parallel to the $\boldsymbol{c}$-axis ($E \parallel \boldsymbol{c}$) corresponds to the TM-polarization while the light polarized perpendicular to the c-axis ($E \perp \boldsymbol{c}$) is called TE-polarization.

Table 1.1: Calculated square of the transition matrix element of GaN and AlN for light polarized parallel and perpendicular to the **c**-axis *[1]*.

GaN			AlN		
Transition	$E \parallel c$	$E \perp c$	Transition	$E \parallel c$	$E \perp c$
$\boldsymbol{E_A(\Gamma_{7C} \leftrightarrow \Gamma_{9V})}$	0	1	$\boldsymbol{E_A(\Gamma_{7C} \leftrightarrow \Gamma_{7V})}$	0.4580	0.0004
$\boldsymbol{E_B(\Gamma_{7C} \leftrightarrow \Gamma_{7V})}$	0.053	0.974	$\boldsymbol{E_B(\Gamma_{7C} \leftrightarrow \Gamma_{9V})}$	0	0.2315
$\boldsymbol{E_C(\Gamma_{7C} \leftrightarrow \Gamma_{7V})}$	1.947	0.026	$\boldsymbol{E_C(\Gamma_{7C} \leftrightarrow \Gamma_{7V})}$	0.0007	0.2310

The results show that the dominant transition from band-to-band for AlN is the conduction band to the topmost valence subband $\boldsymbol{\Gamma_7}$, which has negligible $E \perp \boldsymbol{c}$ component and emits TM-polarized photons. However, for GaN, the leading transition from the conduction band to $\boldsymbol{\Gamma_9}$ valence subband is almost forbidden for $E \parallel \boldsymbol{c}$ and ensures dominant TE-polarized emission. Here we introduce a parameter called the degree of polarization ($\boldsymbol{p}$) to quantize the light polarization properties:

$$p = \frac{I_{TE} - I_{TM}}{I_{TE} + I_{TM}} \qquad \text{1-8}$$

where $\boldsymbol{I_{TE}}$ and $\boldsymbol{I_{TM}}$ are the integrated intensity of the TE- and TM-polarized light, respectively.

These unique optical properties from III-nitride alloys strongly influence efficiencies from LED devices. For example, the TM-polarized photons are difficult to be extracted out from the top and bottom of the devices, which leads to a typical low light extraction efficiency of < 1 %. In addition, radiative recombination is strongly determined by the optical polarization properties from the active region. The influences of the optical polarization properties on LED efficiencies will be detailed discussed in chapter 2.

1.5 Motivation of This Work

Today, high-efficiency and high output power UV LEDs epically in the DUV regime are still challenging. One of the issues is the device optical polarization. However, the influences of the optical polarization on conventional AlGaN QW device efficiency are still not fully investigated.

Therefore, chapter 2 covers the carrier injection efficiency, radiative recombination efficiency and light extraction efficiency study for conventional DUV LEDs. A self-consistent 6-band $\boldsymbol{k \cdot p}$ model, Silvaco Atlas and Synopsys RSOFT FDTD simulation are used to investigate the fundamental challenges for conventional AlGaN QWs in DUV regime, especially the influences of optical polarization on device efficiencies. The optical polarization switching phenomenon, at which the total number of TE-photon equals to TM-photon, is important to understand the fundamental physics of the structure as well as engineering the QW designs. Therefore, a comprehensive study on the influence of the quantum well designs on the AlGaN QW light polarization switching is discussed in chapter 3.

Knowing the difficulty of conventional AlGaN QW in realizing high-efficiency DUV LEDs, we proposed several active region designs to address the issues. The target is to achieve TE-dominant device with a large $\boldsymbol{R_{sp}}$ value. These designs include AlGaN-delta-GaN and AlInN-delta-GaN QWs. The optical properties from the proposed structures are theoretically investigated and compared to that of the conventional AlGaN QWs, as organized in chapter 4. To experimentally realize the advantages of the delta-QW designs, a simplified and epitaxially straightforward structure of AlN-delta-GaN QW UV LED is carried out. The polarization-related properties of the LEDs are studied by both 6-band $\boldsymbol{k \cdot p}$ model and a FDTD simulation with results verified by polarization-dependent electroluminescence (EL) measurements. The results are presented and discussed in chapter 5.

With the success of the AlN-delta-GaN UV LEDs, we used Plasma-Assisted Molecular Beam Epitaxy (PAMBE) to pursue the AlGaN-delta-GaN QW structures growth. The growth details, structural properties and optical characterizations are presented in chapter 6,

In addition, we also proposed different methods to improve other efficiency components in chapter 7. We designed and fabricated nanowire structures and developed self-aligned SiO_2 microsphere arrays to enhance the light extraction efficiency. In addition, we also developed a fabrication process to help the current spreading for DUV LEDs. Besides, the potential of the use of AlGaN substrate is investigated in this study as well.

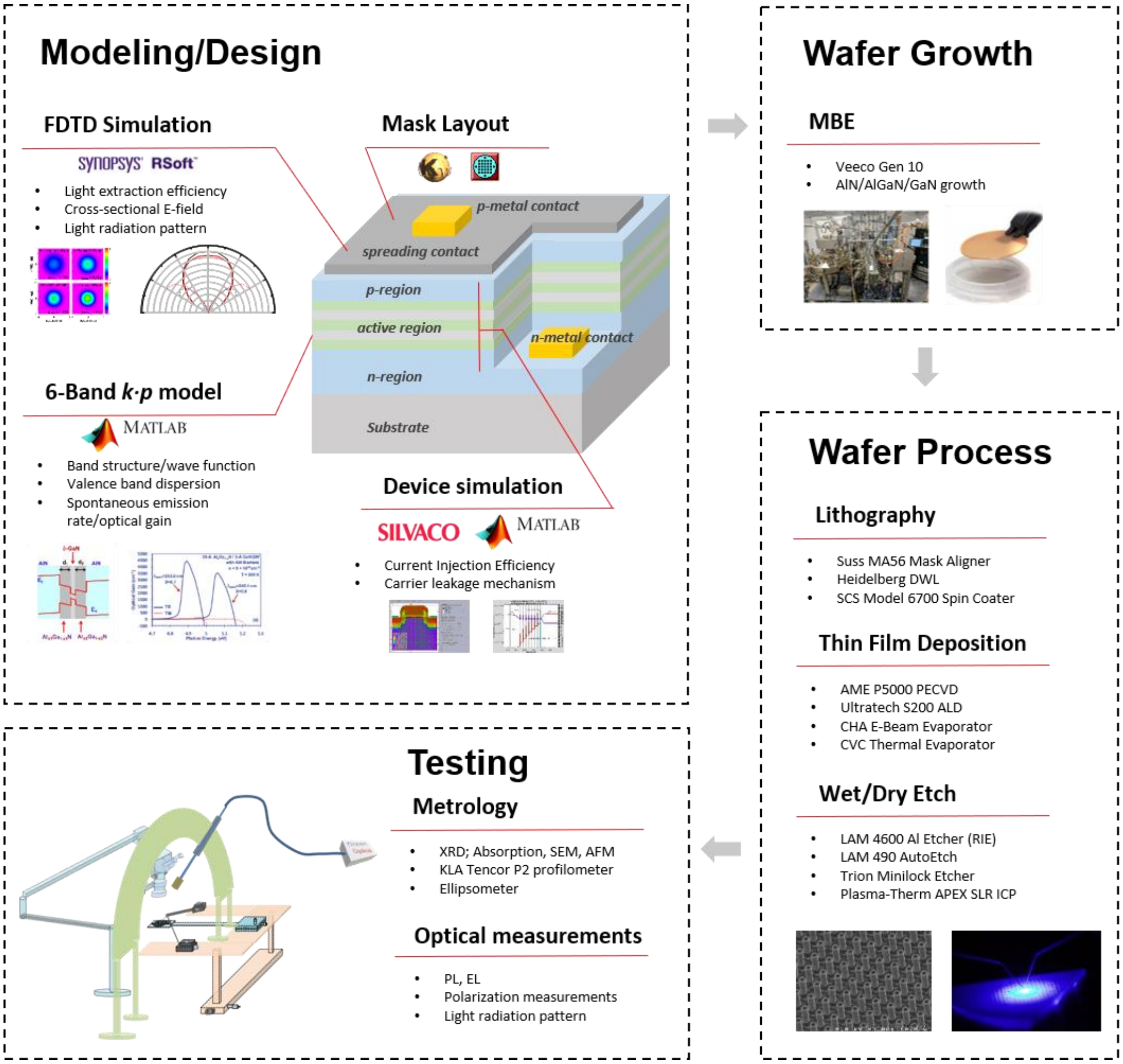

Figure 1.6: *Methodology used in this work.*

Reference for Chapter 1

[1] M. Kneissl and J. Rass, *III-Nitride Ultraviolet Emitters*, 227. Springer International Publishing Cham, 2016.

[2] K. Suzuki and B. W. Smith, *Microlithography : science and technology*. CRC Press, 2007.

[3] V. Bakshi, Ed., *EUV Lithography, Second Edition*. SPIE, 2018.

[4] P. E. Hockberger, “A History of Ultraviolet Photobiology for Humans, Animals and Microorganisms,” *Photochem. Photobiol.*, 76, 6, 561, 2002.

[5] M. Schreiner, J. Martínez-Abaigar, J. Glaab, and M. Jansen, “UV-B Induced Secondary Plant Metabolites,” *Opt. Photonik*, 9, 2, 3, 2014.

[6] S. Vilhunen, H. Särkkä, and M. Sillanpää, “Ultraviolet light-emitting diodes in water disinfection,” *Environ. Sci. Pollut. Res.*, 16, 4, 439, 2009.

[7] M. A. Würtele *et al.*, “Application of GaN-based ultraviolet-C light emitting diodes - UV LEDs - for water disinfection,” *Water Res.*, 45, 3, 1481, 2011.

[8] M. Kneissl, T. Y. Seong, J. Han, and H. Amano, “The emergence and prospects of deep-ultraviolet light-emitting diode technologies,” *Nat. Photonics*, 13, 4, 233–244, 2019.

[9] Z. Xu and B. M. Sadler, “Ultraviolet communications: Potential and state-of-the-art,” *IEEE Commun. Mag.*, 46, 5, 67, 2008.

[10] J. Hodgkinson and R. P. Tatam, “Optical gas sensing: A review,” *Meas. Sci. Technol.*, 24, 1, 2013.

[11] “UV LED market growing at 34% CAGR from $288m in 2017 to $526m in 2020,” *Semiconductor Today,* 2017. [Online]. Available: http://www.semiconductor-today.com/news_items/2017/jun/ledinside_150617.shtml. [Accessed: 13-Aug-2018].

[12] “LEDinside Says Global UV LED Market to Expand at a CAGR of 34% From 2015 to 2020 as Applications for Related Solutions Emerge - LEDinside,” *LED inside,* 2017. [Online]. Available: https://www.ledinside.com/intelligence/2017/6/ledinside_says_global_uv_led_market_to_expand_at_a_cagr_of_34_from_2015_to_2020_as_applications_for_related_solutions_emerge. [Accessed: 13-Aug-2018].

[13] S. Koizumi and K. Watanabe, “Ultraviolet Emission from pn Junction,” *Science (80-.).*, 292, 5523, 1899, 2012.

[14] J. Y. Tsao *et al.*, “Ultrawide-Bandgap Semiconductors: Research Opportunities and Challenges,” *Adv. Electron. Mater.*, 4, 1600501, 2018.

[15] S. Strite, “GaN, AlN, and InN: A review,” *J. Vac. Sci. Technol. B Microelectron. Nanom. Struct.*, 10, 4, 1237, 1992.

[16] P. Pampili and P. J. Parbrook, “Doping of III-nitride materials,” *Mater. Sci. Semicond. Process.*, 62, 180, 2017.

[17] E. Zojer, *Semiconductor optoelectronic devices*. Amsterdam: Academic Press, 2003.

[18] E. F. Schubert, *Light-Emitting Diodes*, (2nd Ed.). Cambridge: Cambridge Universtiy Press, 2006.

[19] T.-Y. Seong, H. Jung, H. Amano, and H. Morkoc, *III-Nitride Based Light Emitting Diodes and Applications*, (2nd Ed.)., 133. Dordrecht: Springer Netherlands, 2017.

[20] Y. Zhao *et al.*, “30-mW-class high-power and high-efficiency blue semipolar $(10\bar{1}\bar{1})$ InGaN/GaN light-emitting diodes obtained by backside roughening technique,” *Appl. Phys. Express*, 3, 102101, 2010.

[21] Y. Chen *et al.*, “High hole concentration in p-type AlGaN by indium-surfactant-assisted Mg-delta doping,” *Appl. Phys. Lett.*, 106, 162102, 2015.

[22] B. P. Gunning *et al.*, “Comprehensive study of the electronic and optical behavior of highly degenerate p-type Mg-doped GaN and AlGaN,” *J. Appl. Phys.*, 117, 045710, 2015.

[23] T. Kinoshita, T. Obata, H. Yanagi, and S. I. Inoue, “High p-type conduction in high-Al content Mg-doped AlGaN,” *Appl. Phys. Lett.*, 102, 012105, 2013.

[24] A. Chakraborty *et al.*, “Electrical and structural characterization of Mg-doped p-type Al0.69Ga0.31N films on SiC substrate,” *J. Appl. Phys.*, 101, 053717, 2007.

[25] S. R. Jeon *et al.*, “Investigation of Mg doping in high-Al content p -type Alx Ga1-x N (0.3<x<0.5),” *Appl. Phys. Lett.*, 86, 082107, 2005.

[26] M. L. Nakarmi, K. H. Kim, J. Li, J. Y. Lin, and H. X. Jiang, “Enhanced p-type conduction in GaN and AlGaN by Mg-δ-doping,” *Appl. Phys. Lett.*, 82, 3041, 2003.

[27] B. Cheng *et al.*, “Enhanced vertical and lateral hole transport in high aluminum-containing AlGaN for deep ultraviolet light emitters,” *Appl. Phys. Lett.*, 102, 231106, 2013.

[28] S. M. Islam *et al.*, “MBE-grown 232-270 nm deep-UV LEDs using monolayer thin binary GaN/AlN quantum heterostructures,” *Appl. Phys. Lett.*, 110, 041108, 2017.

[29] D. A. Laleyan *et al.*, “AlN/h-BN Heterostructures for Mg Dopant-Free Deep Ultraviolet Photonics,” *Nano Lett.*, 17, 6, 3738, 2017.

[30] A. Armstrong and S. Rajan, “Enhanced Light Extraction in Tunnel Junction Enabled Top Emitting UV LEDs Yuewei Zhang,” 052102, 1011, 10–13, 1882.

[31] Y. Zhang *et al.*, “Reflective metal / semiconductor tunnel junctions for hole injection in AlGaN UV LEDs Reflective metal / semiconductor tunnel junctions for hole injection in AlGaN UV LEDs,” *Appl. Phys. Lett.*, 111, 051104, 2017.

[32] P. Sun *et al.*, “Advantages of AlGaN-based deep ultraviolet light-emitting diodes with a superlattice electron blocking layer,” *Superlattices Microstruct.*, 85, 59, 2015.

[33] H. Hirayama, Y. Tsukada, T. Maeda, and N. Kamata, “Marked enhancement in the efficiency of deep-ultraviolet AlGaN light-emitting diodes by using a

multiquantum-barrier electron blocking layer," *Appl. Phys. Express*, 3, 031002, 2010.

[34] T. Takano, T. Mino, J. Sakai, N. Noguchi, K. Tsubaki, and H. Hirayama, "Deep-ultraviolet light-emitting diodes with external quantum efficiency higher than 20% at 275 nm achieved by improving light-extraction efficiency," *Appl. Phys. Express*, 10, 031002, 2017.

[35] H. Hirayama, N. Noguchi, T. Yatabe, and N. Kamata, "227 nm AlGaN light-emitting diode with 0.15 mW output power realized using a thin quantum well and AIN buffer with reduced threading dislocation density," *Appl. Phys. Express*, 1, 0511011, 2008.

[36] H. Hirayama, N. Noguchi, and N. Kamata, "222nm deep-ultraviolet AlGaN quantum well light-emitting diode with vertical emission properties," *Appl. Phys. Express*, 3, 032102, 2010.

[37] H. Hirayama *et al.*, "222-282 nm AlGaN and InAlGaN-based deep-UV LEDs fabricated on high-quality AlN on sapphire," *Phys. Status Solidi Appl. Mater. Sci.*, 206, 6, 1176, 2009.

[38] J. Zhang, H. Zhao, and N. Tansu, "Effect of crystal-field split-off hole and heavy-hole bands crossover on gain characteristics of high Al-content AlGaN quantum well lasers," *Appl. Phys. Lett.*, 97, 111105, 2010.

[39] J. Zhang, H. Zhao, and N. Tansu, "Large optical gain AlGaN-delta-GaN quantum wells laser active regions in mid- and deep-ultraviolet spectral regimes," *Appl.*

Phys. Lett., 98, 171111, 2011.

[40] H. Hirayama, T. Yatabe, N. Noguchi, T. Ohashi, and N. Kamata, "231-261 nm AlGaN deep-ultraviolet light-emitting diodes fabricated on AlN multilayer buffers grown by ammonia pulse-flow method on sapphire," *Appl. Phys. Lett.*, 91, 071901, 2007.

[41] H. Hirayama, N. Maeda, and M. Jo, "Recent Progress and Future Prospects of AlGaN Deep-UV LEDs," *Jpn. J. Appl. Phys.*, 53, 100209, 2014.

[42] Y. K. Ooi and J. Zhang, "Light Extraction Efficiency Analysis of Flip-Chip Ultraviolet Light-Emitting Diodes With Patterned Sapphire Substrate," *IEEE Photonics J.*, 10, 4, 2018.

[43] Y. K. Ooi, C. Liu, and J. Zhang, "Analysis of Polarization-Dependent Light Extraction and Effect of Passivation Layer for 230-nm AlGaN Nanowire Light-Emitting Diodes," *IEEE Photonics J.*, 9, 4501712, 2017.

[44] M. Jo, N. Maeda, and H. Hirayama, "Enhanced light extraction in 260 nm light-emitting diode with a highly transparent p-AlGaN layer," *Appl. Phys. Express*, 9, 012102, 2016.

CHAPTER 2: Basic and Challenges of III-Nitride Deep-Ultraviolet Light-Emitting Diodes

Chapter 1 briefly introduces efficiency issues from DUV LEDs. In general, because of the unique properties of the AlGaN materials, such as wide bandgap, large polarization field and large refractive index, all the three efficiency components present low values from AlGaN-based DUV LEDs, as summarized in figure 2.1.

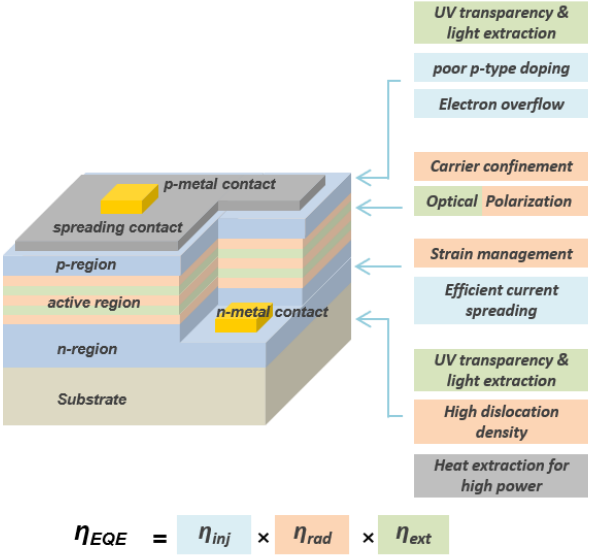

Figure 2.1: *Efficiency components and loss mechanisms in UV LEDs.*

To have a better understanding on the challenges of AlGaN-based DUV LEDs, this chapter will theoretically discuss all the three efficiency components in depth, especially the effect of optical polarization on device efficiency. Specifically, a self-consistent 6-band ***k·p*** model will be used for radiative recombination efficiency calculations. Silvaco Atlas and an in-house carrier transport calculation model are utilized for calculating carrier injection efficiency. For light extraction efficiency, Synopsys RSOFT FDTD simulation is employed.

2.1 Radiative Recombination Efficiency from Conventional AlGaN QWs

As mentioned in the chapter 1, depending on the emission wavelength regimes, the conventional AlGaN QWs suffer from the QCSE, valence band mixing effect and dominant TM-polarization emission, resulting in low TE-polarized (desired polarization for light propagation) spontaneous emission rate. Here we use a self-consistent 6-band $\boldsymbol{k \cdot p}$ model [1] to study the device optical properties from the active region. More details on the simulation model are introduced in appendix B while all the parameters in this study are listed in appendix A. The barrier thickness is kept at 3 nm on each side of the QW for all the simulations.

Figure 2.2 (a) plots the TE- and TM-polarized $\boldsymbol{R_{sp}}$ and degree of polarization (DOP) from 3-nm conventional $Al_xGa_{1-x}N$ QWs. Note that DOP is equal to zero around $\boldsymbol{x} = 0.7$, indicating the TE- and TM-polarized $\boldsymbol{R_{sp}}$ are identical. Throughout the whole DUV regime, the TE-polarized $\boldsymbol{R_{sp}}$ is limited below 1×10^{25} $s^{-1}cm^{-3}$ for the conventional AlGaN QW, which is responsible for the low radiative recombination efficiency, because:

i. Dominant TM-polarized emission

For the conventional $Al_xGa_{1-x}N$ QW with high Al-content ($\boldsymbol{x} > 0.7$), emitting photons with wavelength below ~230 nm, TM-polarized $\boldsymbol{R_{sp}}$ is larger than TE-polarized $\boldsymbol{R_{sp}}$. This is because the ground state CH is the topmost valence subband in the QW structure. For example, figure 2.2 (b) shows the band lineups with wave functions and valence band structure from the 3-nm $Al_{0.8}Ga_{0.2}N$ QW. The ordering of the valence subband ensures majority of the carriers are populated at the ground state CH subband, leading to the generation of the TM-polarized photons. Since the CH hole has a lighter effective mass and its wave function is wider as compared to the that from HH/LH, the ground state electron-hole wave function overlap of 50.94% is large enough to realize high $\boldsymbol{R_{sp}}$ value. However, those TM-polarized photons are difficult to extract out from the device. The total external quantum efficiency is not promising although relatively large radiative recombination efficiency is observed in this regime. More discussion can be found in the following section.

ii. Band mixing effect

Once the emission wavelength reaches 230 - 250 nm, the biggest problem to realize large TE-polarized $\boldsymbol{R_{sp}}$ is the valence band mixing effect. In this regime, the topmost valence subband switches from CH to HH subband, as shown in figure 2.2 (b). For the $Al_{0.7}Ga_{0.3}N$ QW, ground state HH, LH and CH are mixing together with small energy separation. As a result, carriers equally locate at those three energy subbands. The insufficient C-HH transition, together with the relatively low electron-hole wave function overlap ($\boldsymbol{\Gamma_{e1\text{-}hh1}}$ = 21.38%), eventually leads to the low TE-polarized $\boldsymbol{R_{sp}}$.

iii. Quantum confined stark effect

For longer emission wavelength regime (λ > 250 nm), the quantum confined stark effect becomes the biggest obstacle. As presented in figure 2.2 (b), ground state HH is on the top of the valence subband with large energy separation to ground state CH subband. However, the large spontaneous and piezoelectric polarization induce a large electric field in the QW region, which tilts the band energy lineups significantly. Consequently, electron and hole wave functions are pushed to the opposite side of the QW, only $\boldsymbol{\Gamma_{e1\text{-}hh1}}$ = 13.04% can be achieved from the structure. As discussed in the appendix B, the low

$\boldsymbol{\Gamma}_{e1\text{-}hh1}$ will translate into low matrix element value and hence the radiative recombination rate.

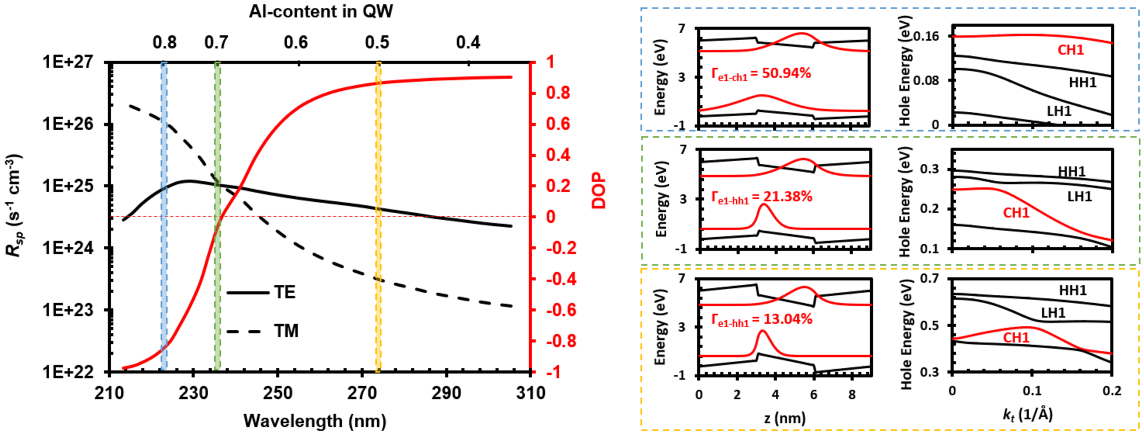

Figure 2.2*: (a)TE- and TM-polarized* $\boldsymbol{R_{sp}}$*, as well as degree of polarization (DOP) at different wavelength; (b) band energy lineups with ground state wave functions and valence band structures from the conventional 3-nm* $Al_{0.8}Ga_{0.2}N$ *QW,* $Al_{0.7}Ga_{0.3}N$ *QW,* $Al_{0.5}Ga_{0.5}N$ *QW.*

As introduced in chapter 1, the $\boldsymbol{R_{sp}}$ is the determinant of radiative recombination efficiency. Here the radiative recombination efficiency is calculated based on the simple ABC-model. The $\boldsymbol{R_{sp}}$ values from figure 2.2 (a) correspond to the black curve in figure 2.3 (a) with SRH coefficient ($\boldsymbol{A}$) of $\boldsymbol{A} = 1\times10^{7}$ s^{-1} and Auger coefficient ($\boldsymbol{C}$) of $\boldsymbol{C} = 1\times10^{-33}$ cm^{6}/s [2]. As discussed, below $\boldsymbol{\lambda} < 230$ nm, the radiative recombination efficiency can reach as high as 80% because of the large TM-polarized $\boldsymbol{R_{sp}}$. For the structure with emission wavelength $\boldsymbol{\lambda} > 230$ nm, the radiative recombination efficiency is limited below 40% and becomes smaller as the emission wavelength increases. Figure 2.3 (a) also plots the radiative recombination efficiency at higher carrier densities ($\boldsymbol{n} = 1\times10^{19}$ cm^{-3} and $\boldsymbol{n} = 5\times10^{19}$ cm^{-3}). Higher efficiency values are observed for structures with higher carrier densities because of the SRH is the dominant non-radiative recombination mechanism under this condition, which is only the first-order function of $\boldsymbol{n}$.

The ***A*** and ***C*** values for DUV LEDs are still under heavy debate. Therefore, we calculated the radiative recombination efficiencies with different ***A*** and ***C*** values and plotted in figure 2.3 (b) and (c). The carrier density is kept at ***n*** = 5×10^{18} cm^{-3}. Small differences in the radiative recombination efficiency are observed if we change the ***C*** value from ***C*** = 1×10^{-34} cm^6/s to ***C*** = 1×10^{-32} cm^6/s, indicating the dominant non-radiative recombination mechanism is still SRH. Further increasing the ***C*** value up to ***C*** = 1×10^{-30} cm^6/s, the efficiency value starts to drop, which means Auger recombination plays a non-negligible role in determining the efficiency. The SRH coefficient (***A***), which is a function of sample dislocation density, strongly influences the radiative recombination efficiency. The efficiency value can be decrease from 80% with ***A*** = 1×10^7 s^{-1} to 30% with ***A*** = 1×10^8 s^{-1}. Therefore, improving substrate quality is a straightforward method to realize high radiative recombination efficiency.

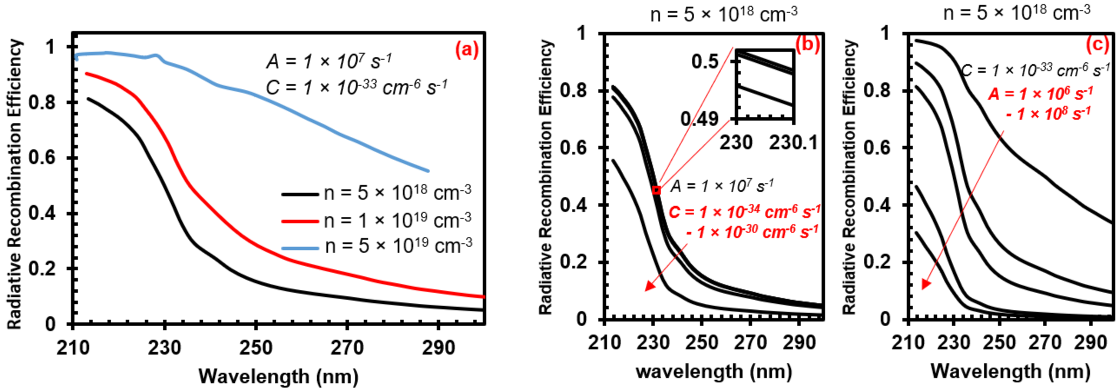

Figure 2.3*: (a) Radiative recombination efficiency from the conventional AlGaN QW at different wavelength with different carrier densities n =* 5×10^{18} cm^{-3}*(black), n =* 1×10^{19} cm^{-3}*(red), n =* 5×10^{19} cm^{-3}*(blue); (b) Radiative recombination efficiency from the conventional AlGaN QW at different wavelength with different C values of* 1×10^{-34} cm^6/s *-*1×10^{-30} cm^6/s*; (c) Radiative recombination efficiency from the conventional AlGaN QW at different wavelength with different A values of* ***A*** *=* 1×10^6 s^{-1} *-* ***A*** *=* 1×10^8 s^{-1}*.*

2.2 Carrier Injection Efficiency from Conventional AlGaN QW

AlGaN-based QWs usually suffer from the efficiency reduction at high operating current density, known as "efficiency droop" due to the thermionic escape of carriers [3]. Here we theoretically study the carrier injection efficiency based on analytical equations from current continuity relation for carrier transport across the barrier [2].

2.2.1 *Model of Current Injection Efficiency for AlGaN LEDs*

i. Formulation of current injection efficiency model for quantum well LEDs/lasers

The formulation of current injection efficiency model for quantum well LEDs/lasers has been detailed discussed for InGaAsN-based laser devices [4] and InGaN-based LEDs [2]. For clarity, the schematic of a single quantum well structure used in the numerical model is presented in figure 2.4 (a) inset. The current injection efficiency formulation is simplified from the dynamic of the carrier density in the QW (***N***$\boldsymbol{N_{QW}}$) and barrier ($\boldsymbol{N_B}$), as well as the dynamic relation of the photon density (***S***), and described as:

$$\eta_{injection} = \frac{1}{1 + \frac{\tau_{bw}}{\tau_B} \cdot \left(1 + \frac{\tau_{QW_{total}}}{\tau_e}\right)} \qquad \text{2-1}$$

where $\tau_{QW_{total}}$ stands for the total carrier lifetime in the QW region and can be obtained by calculating the radiative lifetime and non-radiative lifetime $\frac{1}{\tau_{QW_{total}}} = \frac{1}{\tau_{rad}} + \frac{1}{\tau_{nonrad}} = A + B \cdot N_{QW} + C \cdot {N_{QW}}^2$. Similarly, carrier lifetime in barrier τ_B can be calculated. $\tau_{bw}$and τ_e here represent the barrier-well lifetime and thermionic carrier escape lifetime.

ii. Thermionic Carrier Escape Rate for Quantum Well-Barrier LEDs

The thermionic carrier escape lifetime is the determinant for the total current injection efficiency. As indicated in *Eq.* 2-1, a small thermionic carrier lifetime, which means a large escape rate of the carriers from the QW to the barrier, leads to a lower current injection efficiency. The thermionic carrier leakage currents can be expressed as:

$$J_{thermionic_e} = \frac{4\pi \cdot q \cdot (k_B T)^2}{h^3} \cdot m_e^* \cdot \exp\left(-\frac{E_{b_e} - F_e}{k_B T}\right) \qquad 2\text{-}2$$

$$J_{thermionic_h} = \frac{4\pi \cdot q \cdot (k_B T)^2}{h^3} \cdot m_h^* \cdot \exp\left(-\frac{E_{b_h} - F_h}{k_B T}\right) \qquad 2\text{-}3$$

where m_e^* and m_h^* are electron and hole effective masses. $\boldsymbol{E_{b\_e}}$ and $\boldsymbol{E_{b\_h}}$ stand for the effective barriers for conduction band and valence band, respectively, and are calculated as the average barrier height. $\boldsymbol{F_e}$ and $\boldsymbol{F_h}$ represent the quasi-fermi levels for electron and hole.

The thermionic carrier lifetime can be calculated based on the thermionic carrier leakage current:

$$\tau_{e_e} = \frac{n \cdot q \cdot L_z \cdot N_{QW}}{J_{thermionic_e}} \qquad 2\text{-}4$$

$$\tau_{e_h} = \frac{n \cdot q \cdot L_z \cdot N_{QW}}{J_{thermionic_h}} \qquad 2\text{-}5$$

here $\boldsymbol{L_z}$ is the QW thickness while $\boldsymbol{n}$ represents the carrier density. Note that the thermionic carrier lifetimes from *Eq.* 2-4 and 2-5 only calculate one side of the QW. The carrier leakage can be contributed by the both sides of the QW and the final expression is

$$\frac{1}{\tau_e}=\frac{1}{\tau_{e_e}}+\frac{1}{\tau_{e_h}}=\frac{1}{\tau_{e_{e_{left}}}}+\frac{1}{\tau_{e_{e_{right}}}}+\frac{1}{\tau_{e_{h_{left}}}}+\frac{1}{\tau_{e_{h_{right}}}} \qquad \text{2-6}$$

For AlGaN-based DUV LEDs, thermionic carrier leakage for electron mainly comes from p-side barrier while the leakage for hole mainly takes place from n-side.

iii. Barrier-Well Lifetime (τ_{bw}) in QW LEDs

The barrier-well lifetime (τ_{bw}) is the sum of the carrier transport time (τ_r) and the quantum capture time (τ_{cap}).The carrier capture time is defined as the time required for the carrier being captured in the QW region, and usually in the femtosecond range. For carrier transport time, which is from the barrier to the QW region, can be expressed as follow based on the ambipolar carrier transport:

$$\tau_r=\frac{1}{2}\cdot\left(\frac{{L_S}^2}{2\cdot D_p}+\frac{{L_S}^2}{2\cdot D_n}\right) \qquad \text{2-7}$$

$$D_p=\left(\frac{k_BT}{q}\right)\mu_p \quad D_n=\left(\frac{k_BT}{q}\right)\mu_n \qquad \text{2-8}$$

where $\boldsymbol{L_s}$ and $\boldsymbol{D_p}$ ($\boldsymbol{D_n}$) represent for the thickness of the barrier region and diffusion coefficient for hole (electron), respectively.

2.2.2 Current Injection Efficiency from conventional AlGaN QW LEDs

Based on the carrier injection model, the injection efficiency from AlGaN QW LEDs are calculated in this study. The $\boldsymbol{\tau_{QW_{total}}}$ is obtained from the $\boldsymbol{R_{sp}}$ values calculated by the 6-band $\boldsymbol{k\cdot p}$ model. All the parameters used in this work can be found from appendix A.

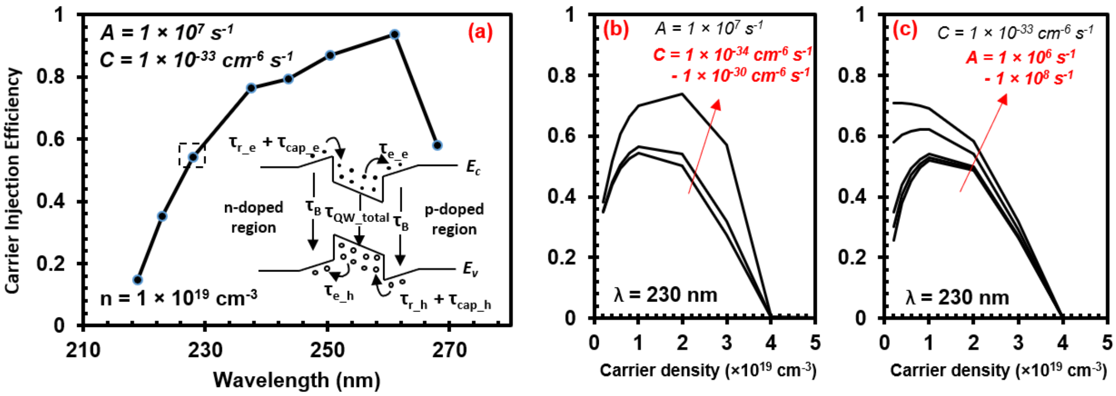

***Figure 2.4**: (a) Carrier injection efficiency from AlGaN QW LEDs at different wavelength; inset: Schematic illustration of carrier injection model (b) carrier injection efficiency from the conventional AlGaN QW at 230 nm with different C values of 1×10^{-34} cm^6/s -1×10^{-30} cm^6/s; (c) carrier injection efficiency from the conventional AlGaN QW at 230 nm with different A values of **A** = 1×10^{6} s^{-1} - **A** = 1×10^{8} s^{-1}.*

Figure 2.4 (a) plots the carrier injection efficiency from the conventional AlGaN QW LEDs at different emission wavelength. The Al-contents in the QW and barrier regions are selected based on the reported values and summarized in table 2-1.

Table 2.1: Values of Al contents (***x***) in $Al_xGa_{1-x}N$ wells and (***y***) in $Al_yGa_{1-y}N$ barriers [3]

Wavelength (nm)	Al-content in QW (*x*)	Al-content in barrier (*y*)
219	0.83	0.89
223	0.79	0.87
228	0.74	0.84
237.5	0.64	0.78
243.6	0.60	0.75

250.5	0.55	0.72
261	0.47	0.67
268	0.40	0.55

As shown in figure 2.4 (a), in general, the carrier injection efficiency increases as the emission wavelength increases. This is because the higher effective barrier height obtained from the QW designs for devices with longer emission wavelength. For example, at $\boldsymbol{n}$ = 1×10^{19} cm^{-3}, the total thermionic carrier lifetimes are calculated as 9.2922×10^{-13} s for 223-nm LED and 2.6037×10^{-11} s for 250.5-nm LED, which results in 35.26% and 86.87% injection efficiency, respectively with $\boldsymbol{A}$ = 1×10^{7} s^{-1} and $\boldsymbol{C}$ = 1×10^{-33} cm^{6}/s. The carrier injection efficiencies from 230-nm AlGaN LEDs with different $\boldsymbol{A}$ and $\boldsymbol{C}$ values are calculated and shown in figure 2.4 (b) and (c). The influence of the non-radiative recombination coefficients on device injection efficiency is less significant than that on device radiative recombination efficiency. Note that as the carrier density increases to $\boldsymbol{n}$ = 2×10^{19} cm^{-3}, the carrier injection efficiency starts decreasing, which is consistent with the reported experiment results in which efficiency droop occurs.

To minimize the efficiency droop from the AlGaN QW LEDs, researchers have developed multiple-barrier EBLs, which combined with other techniques, such as patterned sapphire substrate, highly-reflective p-electrode and photonic crystals, enable the device to reach a record 20% external quantum efficiency from DUV LEDs.

2.3 Light Extraction Efficiency from Conventional AlGaN QW

As mentioned previously, the conventional AlGaN QW will generate both TE- and TM-polarized photons. Here, the TE-polarized light is defined as the light with electric field perpendicular to the growth direction (***c***-axis) while TM-polarized light is the light with electric field along the growth direction. Therefore, different radiation pattern inside the semiconductors can be expected for TE- and TM-polarized photons, as well as the light extraction efficiency. Here we use a FDTD method from Synopsys RSOFT to calculate the light extraction efficiency and light radiation pattern from the conventional AlGaN QW LEDs at different emission wavelengths. The Al-contents used in this study at each wavelength are taken from ref. [3] .The refractive indices for AlGaN material follow the linear relationship. Figure 2.5 (a) shows a schematic of the simulated bottom-emitting structure. This study also investigates the top-emitting device which has identical layers with flipped structure. A perfect electric conductor (PEC) boundary was used at the bottom of the simulation domain, while perfectly matched layer (PML) was used for all the other domain surfaces. A dipole source with $\boldsymbol{E_x}/\boldsymbol{E_y}$ and $\boldsymbol{E_z}$ directions is placed at the active region center to study the TE- and TM-polarized light radiation properties, respectively. To measure the light extraction efficiency, two monitors are required. One is placed to enclose the dipole source while the other one is located at the top of the simulation domain, 1.4 µm above the semiconductor or sapphire/air interface.

TE- and TM-polarized light extraction efficiencies at different emission wavelengths are calculated and plotted in figure 2.5 (b). Due to the large refractive index difference between AlN (or sapphire)/air, both TE- and TM-polarized light extraction efficiencies are limited below 20% throughout the whole DUV regime. In addition, because of the electric field directions, TE-polarized photons prefer emitting at small angles with respect to the ***c***-axis while TM-polarized photons mainly propagate at larger angles, which can be observed from the light radiation patterns in figure 2.5 (b). As a result, TM-polarized photons have a much smaller LEE as compared to TE-polarized photons.

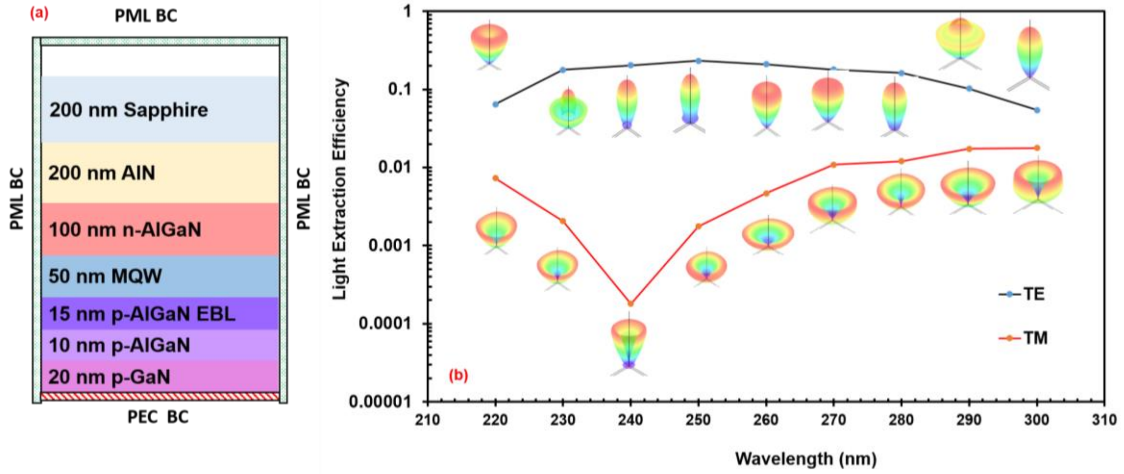

Figure 2.5*: (a) schematic of the FDTD simulated bottom-emitting AlGaN-based QW DUV LEDs (b) TE- and TM-polarized light extraction efficiencies and light radiation patterns from AlGaN-based DUV LEDs at different emission wavelengths.*

The light extraction properties from top-emitting devices are also investigated in this study as well and presented in figure 2.6 (a). Similar to the bottom-emitting devices, both TE- and TM-polarized light extraction efficiencies are limited below 20% due to the large refractive index difference between p-GaN/air. As discussed in section 2.1, both TE- and TM-polarized photons can be generated in the conventional AlGaN QW, and the ratio varies as the wavelength changes. Here we calculated the effective light extraction values based on the DOP values collected from the figure 2.2 and the light extraction data. As shown in fig. 2.6 (b), the effective light extraction efficiency increases up to 20% from 220 nm to 250 nm and then maintains at the 10% -20% range. This is because TM-polarized photons are dominant in the shorter emission wavelength regime, which has extremely low LEE values. Here we assume 100% current injection efficiency from the AlGaN-based devices, the total external quantum efficiency can be calculated by considering both radiative recombination efficiency collected in section 2.1 and the effective light extraction efficiency. As shown in figure 2.6 (b), the total external quantum efficiency for conventional bottom-emitting AlGaN QW LEDs are below 3% throughout the entire DUV range.

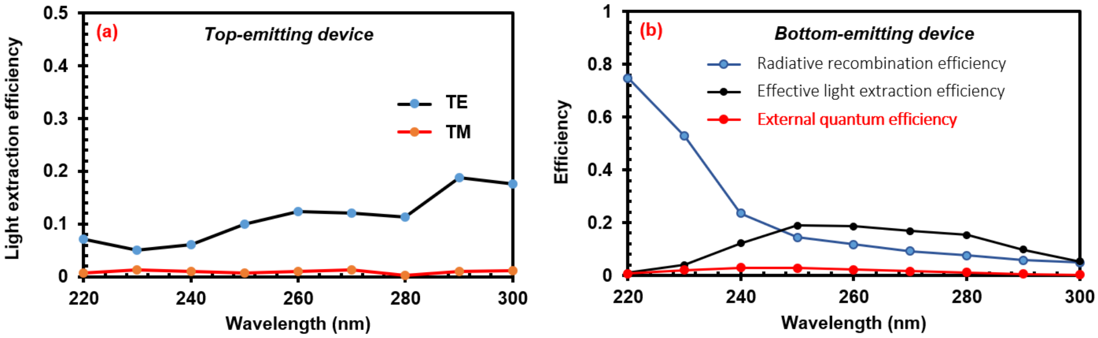

Figure 2.6*: (a) TE- (black) and TM- (red) light extraction efficiency from conventional top-emitting AlGaN QW at different emission wavelengths (b) radiative recombination efficiency, effective light extraction efficiency and external quantum efficiency from conventional bottom-emitting AlGaN QW at different emission wavelengths.*

2.4 Summary

In summary, radiative recombination efficiency, carrier injection efficiency, and light extraction efficiency from conventional AlGaN QW LEDs are theoretically investigated in this chapter. Both TE- and TM-polarized photons are considered here. The results show that it is difficult to realize large TE-$\boldsymbol{R}_{sp}$ because of the topmost CH subband, band mixing effect, and QCSE at different wavelengths. The influence of optical polarization properties on device light extraction efficiency are also investigated in this study, showing extremely small TM-polarized LEE because of the nature of the TM-polarized light. Although the LEE for TE-polarized photon can reach 20%, the low radiative recombination efficiency eventually determines the limited external quantum efficiency. Therefore, to engineer the polarization properties, there are two methods. One is to design a structure that emits a dominant TE-polarized light with large $\boldsymbol{R_{sp}}$ which is introduced and investigated in chapter 4-6. Another method is to engineer the geometry of the full LED structure to significantly improve TM-polarized LEE, which will be introduced as nanowire LEDs in chapter 7.

Reference for Chapter 2

[1] H. Zhao, R. A. Arif, Y. K. Ee, and N. Tansu, “Self-consistent analysis of strain-compensated InGaN-AlGaN quantum wells for lasers and light-emitting diodes,” *IEEE J. Quantum Electron.*, 45, 1, 66, 2009.

[2] H. Zhao, G. Liu, J. Zhang, R. A. Arif, and N. Tansu, “Analysis of internal quantum efficiency and current injection efficiency in III-nitride light-emitting diodes,” *IEEE/OSA J. Disp. Technol.*, 9, 4, 212–225, 2013.

[3] M. Kneissl and J. Rass, *III-Nitride Ultraviolet Emitters*, 227. Springer International Publishing Cham, 2016.

[4] J. Y. Yeh, L. J. Mawst, and N. Tansu, “The role of carrier transport on the current injection efficiency of InGaAsN quantum-well lasers,” *IEEE Photonics Technol. Lett.*, 17, 9, 1779–1781, 2005.

CHAPTER 3: Optical Polarization from AlGaN-Based Deep-Ultraviolet Light-Emitting Diodes

Chapter 1 and 2 introduce the band structure profiles for III-nitride alloys, especially AlN and GaN. Due to the large difference of the crystal-field splitting energy between AlN (-169 meV) and GaN (10 meV), the valence band orderings are dissimilar for AlN and GaN, which results in light polarization changes from dominant TM for AlN to TE for GaN. Consequently, AlGaN-based DUV LED are emitting both TM- and TE-polarized photons and the percentage of each polarization is determined by the Al-composition in the corresponding AlGaN QWs. It has been well discussed that the light polarization from the QW structure strongly influences the internal quantum efficiency and light extraction efficiency. Therefore, the understanding of the light polarization from DUV LEDs is essential for the structure design in order to optimize device total efficiency.

In this chapter, this work theoretically investigates the effect of the quantum well designs, especially the quantum well thickness, on the optical polarization of AlGaN-based UV LEDs. All the band structure calculations are based on the self-consistent 6-band $\boldsymbol{k}\cdot\boldsymbol{p}$ model described in appendix B.

3.1 Factors Influencing the Light Polarization Switching in AlGaN Layer

In literature, a large variation in the Al-content, at which the light polarization from $Al_xGa_{1-x}N$ layers switching occurs, has been reported. Zhang *et al*. realized the switching from TE- to TM-polarization for 3-nm $Al_xGa_{1-x}N$/AlN QW at x = 68% [3]. Kawanishi *et al.* studied the AlGaN MQW lasers grown on free-standing AlN template on SiC substrates, showing the laser polarization changes from TM mode to TE mode at an Al content of x ≈ 0.36 – 0.41 [4]. Banal *et al.* reported the critical Al-content of ~ 83% for $Al_xGa_{1-x}N$/AlN QW grown on sapphire substrates at which the light polarization switches based on experimental results [5].

There are many influencing factors cause the discrepancies in the reported values of the critical Al-content, such as the strain state, quantum well/barrier thickness, substrate type.

3.1.1 Strain State of the AlGaN Layers

An analytical expression of the energy splitting in an unstrained $Al_xGa_{1-x}N$ layer is shown in *Eq.* 1-7. The critical Al-content at which $\Gamma_9 = \Gamma_7$ is achieved only when $\Delta_{cr} = 0$. Assuming the parameters for AlGaN alloy follow a linear relationship between that of AlN and GaN, the critical Al-content is calculated as $\boldsymbol{x}$ = 0.044 [5].

Taking into consideration the strain state, the band-edge energies should be modified by a strain-related factor. The $\Delta' = \Delta_{\mathrm{cr}} + \left[\mathrm{D}_3 - \mathrm{D}_4 \frac{\mathrm{C}_{33}}{\mathrm{C}_{13}}\right] \varepsilon_{\mathrm{zz}}$ replaces $\boldsymbol{\Delta_{cr}}$ for the energy splitting calculation. Therefore, for a strained $Al_xGa_{1-x}N$ layer on the AlN template, the critical Al-content is realized by solving $\Delta' = 0$ and calculated as $\mathbf{x}$ = 0.6

[5]. A cartoon is plotted in figure 3.1 to explain the strain effect in the AlGaN/AlN QW. Specifically, the in-plane compressive stain in the AlGaN layer push the $|\boldsymbol{X} \pm \boldsymbol{iY}\rangle$-related bands upward while the tensile strain along the c-axis causes the $|\boldsymbol{Z}\rangle$-related band move downward. As a result, a higher Al-content is required to realize $\boldsymbol{\Gamma_9} = \boldsymbol{\Gamma_7}$ for strained AlGaN layer as compared to the unstrained AlGaN alloy, which has been demonstrated by several reports [5]–[7].

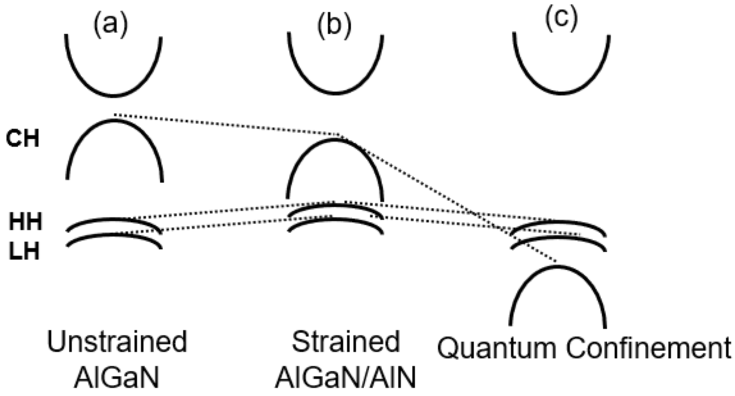

***Figure 3.1**: Schematic of band structures for (a) strained $Al_xGa_{1-x}N$, (b) strained $Al_xGa_{1-x}N$ on AlN, (c) $Al_xGa_{1-x}N$/AlN QWs near the Γ point [5].*

3.1.2 Quantum Confinement in AlGaN QWs

Besides the strain state, the quantum confinement in $Al_xGa_{1-x}N/Al_yGa_{1-y}N$ QWs affects the optical polarization as well. It has been realized that the effective mass of CH hole is much smaller than that of HH and LH [5]. Therefore, the quantum confinement pushes the lighter CH subband deeper into the QW than HH and LH subbands and higher critical Al-content is expected for optical polarization switching.

Quantum well thickness is one of the factors that strongly influences the quantum confinement and as well as the optical polarization. Banal *et al.* utilized a simple model to study the effect of the quantum confinement on the splitting energy $\boldsymbol{\Gamma_7 - \Gamma_9}$ [5]. For thin quantum wells (< 3 nm), the well width is the strongest factor for the quantum confinement which lowers the energy of the CH subband. Therefore the critical Al-content shifts to a higher value as the well width shrinks. For thick quantum wells (> 3 nm), the well width is no longer the determinant factor. Instead, the internal polarization field starts to dominate the quantum confinement. The critical Al-content is found to be independent of the well width. In addition, Al Tahtamouni *et al.* studied the optical polarization of $Al0_{0.65}Ga_{0.35}N/AlN$ quantum wells with different quantum well thickness by using photoluminescence spectroscopy. As the quantum well thickness shrinks down to 2 nm, the dominant light polarization switches from $E \parallel c$ (TM-polarized) to $E \perp c$ (TE-polarized) [8]. Wierer *et al*. also found the degree of polarization decreases with increasing the well width for $Al_xGa_{1-x}N/Al_yGa_{1-y}N$ QWs [9]. However, the influence of the QW thickness on the light polarization switching are still unclear, which will be discussed in the following section.

The Al-content in the quantum barrier decides the barrier height in the active region and is a nonnegligible factor for the quantum confinement. It is well known that the higher the barrier is, the better quantum confinement can be achieved. Northrup *et al.* demonstrated the lighter CH subband is more sensitive to the barrier height adjustment [6]. Reich *et al.* also found that as the barrier composition increases, the light polarization switches from TM to TE for 1.5-nm QWs with same QW Al-content [10].

Besides, the critical Al-content is also related to the carrier density [11]. Specifically, the critical Al-content at which polarization switching takes place decreases with increasing carrier density. This can be explained by the fact that high carrier density enables more carrier population at the second and third highest valence subbands, which will take the transition matrix elements far from $\boldsymbol{k} = 0$ into consideration when we study the light emission characteristics. And it should be noted that the matrix elements for TM polarization above the band edge are larger than those for the TE polarization, which favors the total TM-polarization at higher carrier density.

3.1.3 Other Factors

The UV LEDs grown on different substrate types or substrate orientations also have different polarization characteristics [12]–[14]. The temperature decides the carrier population as well and therefore the light polarization [15]. More discussion can be found in *Ref.* [2].

3.2 Effect of QW Thickness on the Optical Polarization of AlGaN-Based DUV LEDs

The critical Al-content at which the light polarization from UV LEDs crossover takes places is demonstrated to be influenced by many factors, such as the strain state, quantum confinement and substrates type. However, the physical mechanisms related to the shift of the critical Al-content are still unclear. For example, Banal *et al.* observed the light polarization for $Al_{0.82}Ga_{0.18}N$/AlN QW switched from TM to TE as the well width decreased from 13 nm to 1.3 nm [5]. Al Tahtamouni *et al.* realized a similar trend in $Al_{0.65}Ga_{0.35}N$/AlN QWs by reducing the QW thickness from 3 nm to 1 nm [8]. However, a dominant TE-polarized emission was reported from 2-nm $Al_{0.66}Ga_{0.34}N$/4.8-nm $Al_{0.83}Ga_{0.17}N$ QW [16] while a dominant TM-polarized emission from 1-nm $Al_{0.66}Ga_{0.34}N$/4.1-nm $Al_{0.83}Ga_{0.17}N$ QW [17], which is inconsistent with the previous reported results. In addition, all the studies so far focus on the devices with the same Al-content. The effect of the QW thickness on the critical Al-content change has not been reported yet, which is also important for the DUV active region design.

This work theoretically calculates the light polarization properties from AlGaN QW and predicts the critical Al-content for the QWs with different QW thicknesses (d) by using the self-consistent 6-band $\boldsymbol{k \cdot p}$ model. AlN was served as the quantum barrier material with a thickness of 6 nm at each side. The carrier density is fixed at 5 $\times 10^{18}$ cm^{-3} throughout the simulation. More simulation method details can be found in appendix B. Material parameters used in this study are summarized in appendix A.

As mentioned earlier, $\Delta' = 0$ takes place at Al-content $x = 0.6$ for strained $Al_xGa_{1-x}N$ alloy. Taking into consideration the quantum confinement, we achieved the critical Al-content at which HH and CH have the same energy level and plotted in figure 3.3. Without the internal electric field, it can be simplified to a 1-dimensional Schrodinger equation. The quantum confinement becomes stronger as the QW thickness decreases, which pushes the CH subband downward. As a result, higher Al-content is required to realize HH and CH energy levels crossover. The trend is similar to the previously reported data [5]. However, for ultra-thin QW ($\boldsymbol{t}$ < 1.5 nm), the decrease of the well width does not lead to a higher critical Al-content, which has not been discussed in the previous study. The unnormal phenomenon can be explained by the barrier height difference between the CH and HH subbands. Specifically, the band-edge energy of CH subband (E_2^0) is higher than that of HH subband (E_1^0) for both AlN barrier and high AlGaN QW with high Al-content, as shown in figure 3.3 inset. However, the barrier height of CH subband which is defined as $\Delta E_2^0 = |E_2^0(AlN) - E_2^0(AlGaN)|$ is smaller than that of the

HH subband $\Delta E_1^0 = |E_1^0(AlN) - E_1^0(AlGaN)|$, which weakens the quantum confinement for CH subband. The weaker quantum confinement caused by the barrier height difference becomes nonnegligible for ultra-thin QW and eventually results in the unnormal trend for the critical Al-content. The quantum confinement can be further affected by the internal electric field. As shown in figure 3.2 taking into consideration both spontaneous polarization and piezoelectric polarization, the critical Al-content rises as the QW thickness increases from 1 nm to 5 nm. The internal electric field in the QW structure follows the *Eq*. B-45. However, the influence of the internal electric field on energy levels is still under debate.

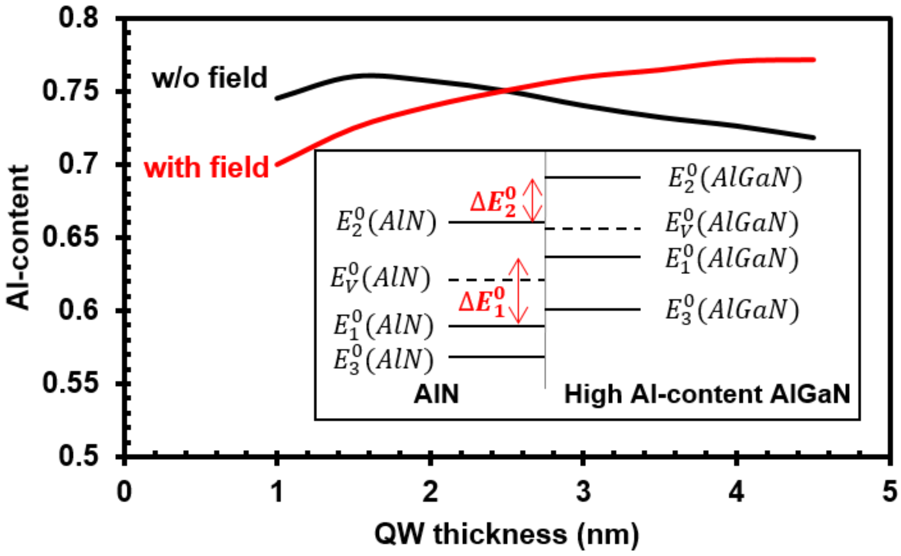

Figure 3.2 *: Critical Al-content where valence subbands crossover occurs with (red) and without (black) Electric field. Inset: Band-edge energies of AlN and high Al-content AlGaN Wurtzite semiconductors.*

The spontaneous emission recombination rates (**R_{sp}**) directly determined the light polarization characteristics from the active region. The critical Al-contents at which TE- and TM-polarized **R_{sp}** are identical are calculated and plotted in figure 3.3 (a), with considering the internal electric field. As the QW thickness increases, the crossover Al-content rises to $x = 0.75$ at $t = 1.5$ nm and then falls throughout the simulation regime. For the critical emission wavelength, an increasing trend is observed as the QW thickness increases, which is attributed to the reduced critical Al-content and the weaker quantum confinement. The two critical Al-content curves for valence subband crossover and $\boldsymbol{R_{sp}}$ switching are compared in figure 3. 3(b). The critical Al-content for valence subband crossover is higher than that for $\boldsymbol{R_{sp}}$ crossover for thin QWs (< 2.2 nm) while it is lower for thick QW. To study the physics behind the critical Al-content change, two structures (1.5-nm QW and 3-nm QW) with critical Al-contents at which TE- and TM-polarized $\boldsymbol{R_{sp}}$ switching takes place are further investigated.

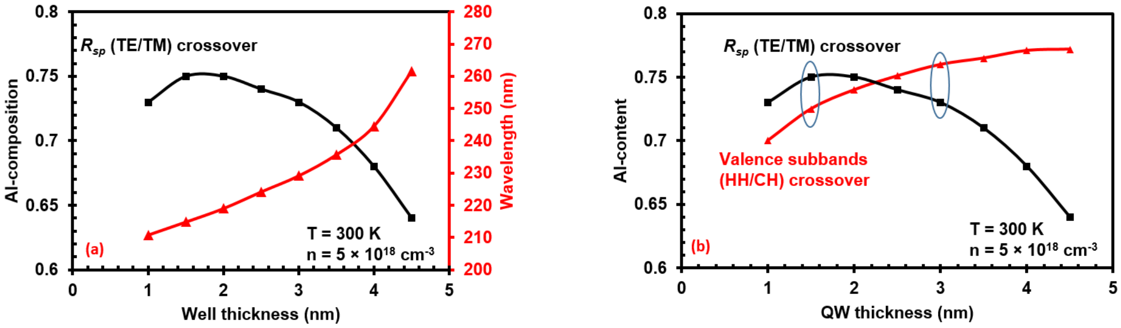

***Figure 3.3**: (a) critical Al-content (black) and critical emission wavelength (red) where TE-$\boldsymbol{R_{sp}}$=TM- $\boldsymbol{R_{sp}}$ as a function of QW thickness. (b) Comparison between $\boldsymbol{R_{sp}}$ crossover (black) and valence subbands crossover.*

For 1.5-nm $Al_{0.75}Ga_{0.25}N$ QW, the Al-content is higher than the critical Al-content for valence subband crossover, which indicates CH subband is on the top of the valence band. The band structure with ground state electron and hole wave functions are plotted in figure 3.4(a). The narrow QW region helps the electron-hole wavefunction overlap and a large matrix element value can be expected. Figure 3.4 (b) plots the envelope wave functions of the top three subbands for 1.5-nm $Al_{0.75}Ga_{0.25}N$ QW. The top three subbands are labeled as CH, HH, and LH due to the dominant $g^{(3)}, g^{(1)}, g^{(2)}$ wavefunctions, respectively. Note that the coupling between the LH and CH subband is weak, which will result in small TM-polarized emission from C-LH transition and negligible TE-polarized emission from C-CH transition. The valence band structure near the zone center is plotted in figure 3.4 (c), the small energy separations between the ground state CH, HH and LH subbands ensures the carriers populating all three valence subband with similar surface carrier densities. Another factor determining the spontaneous emission, which is the square of the momentum matrix element, is examined in figure 3.4 (d). Large momentum matrix elements are observed from the transition C-CH1, C-HH1 and C-LH1, which are attributed to the fact that the thin QW ensures the

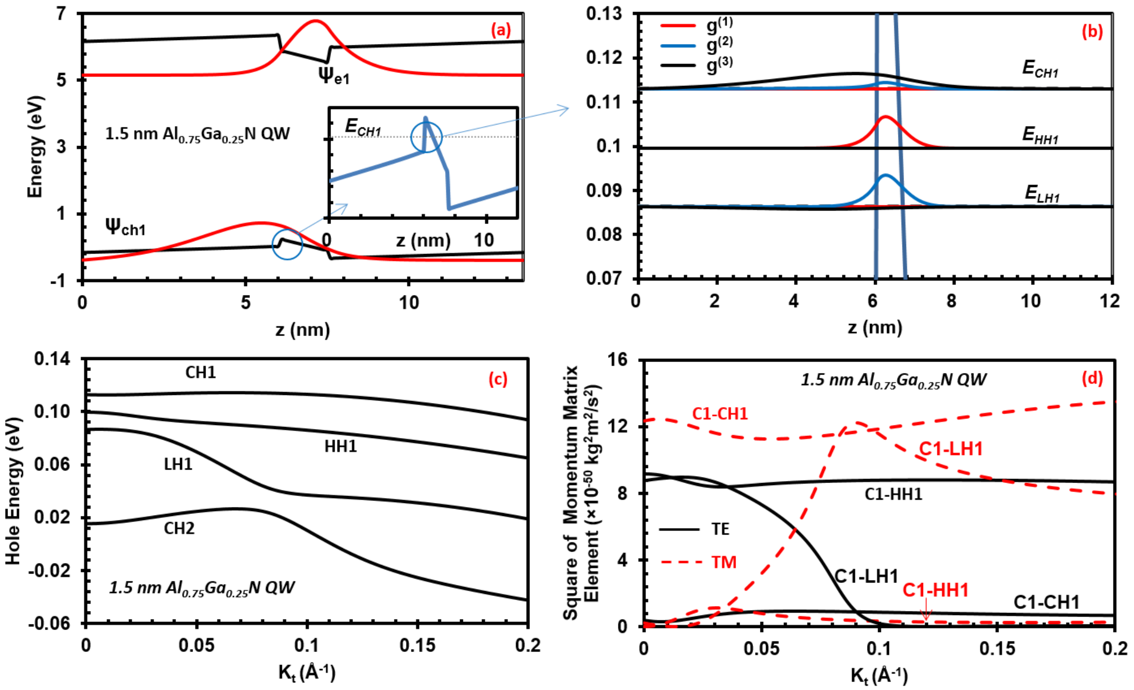

***Figure 3.4**: (a) Band structure and wavefunctions (b) envelope wavefunctions of the highest three subbands (c) valence band structure near Γ point (d) TE- (solid) and TM-polarized (dash) square of momentum matrix elements from C1-CH1, C1-HH1, C1-LH1 transitions for 1.5-nm* $Al_{0.75}Ga_{0.25}N$ *QW.*

large electron-hole wave function overlaps for all the three ground states CH, HH and LH subbands. Note that although the matrix element from C-CH1 has the highest value due to the wider CH wave function, the differences between all the matrix elements are small for the thin QW. In addition, the weak interaction between CH and LH subbands ensures the minimum TE-polarized matrix element from the C-CH transition and small TM-polarized matrix element from C-LH transition. For 1.5-nm $Al_{0.75}Ga_{0.25}N$ QW, although the surface carrier density and TM-polarized matrix element from the CH1 subband are larger than that from HH1 and LH1 subbands, the TM-polarized $\boldsymbol{R_{sp}}$ generated by C-CH1 transition is identical to the TE-polarized $\boldsymbol{R_{sp}}$ produced by the combination of the C-HH1 and C-LH1 transition.

For 3-nm $Al_{0.73}Ga_{0.27}N$ QW, the internal electric field pushes the electron and hole wave functions to the opposite of the QW, which results in a small electron-hole wave function overlap, as shown in figure 3.5 (a). Since the Al-content from the QW is smaller than the critical Al-content for valence subbands crossover, HH occupies the highest energy level, followed by the LH and CH subbands. Checking the envelope wave functions from the top four energy states, there is a strong interaction between CH and LH subbands in this structure, which is evidenced by the envelope wave functions profiles in the second and third energy states shown in figure 3.5 (b). The valence band structure from 3-nm $Al_{0.73}Ga_{0.27}N$ QW in figure 3.5 (c) shows the top three valence subbands are closely separated, which indicates the similar surface carrier densities from the three energy states. Both TE-polarized and TM-polarized momentum matrix elements are plotted in figure 3.5 (d). Note that the matrix elements from C-CH1 transition are much larger than that from other transitions because the wider CH subband wave function suffers less severe QCSE, as compared to other subbands. Therefore, although HH1 is the highest energy state with the largest carrier density, the large TM-polarized matrix element generated by the C-CH transition ensures the total TM-polarized $\boldsymbol{R}_{sp}$ is comparable to the total TE-polarized $\boldsymbol{R}_{sp}$. In addition, it is worth to note that the TM-polarized matrix element from C-LH transition is larger than the TE-polarized matrix element from the same transition due to the strong interaction between LH and CH subbands.

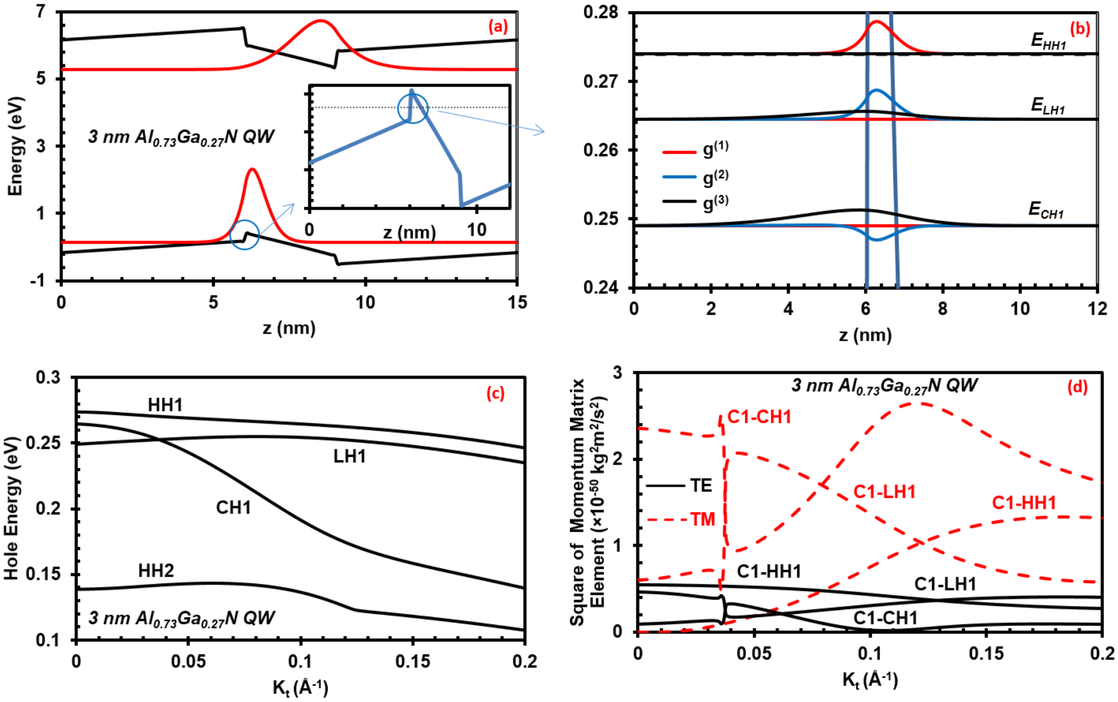

***Figure 3.5**: (a) Band structure and wavefunctions (b) envelope wavefunctions of the highest three subbands (c) valence band structure near **Γ** point (d) TE- (solid) and TM-polarized (dash) square of momentum matrix elements from C1-CH1, C1-HH1, C1-LH1 transitions for 3-nm $Al_{0.73}Ga_{0.27}N$ QW.*

From previous discussions on the 1.5-nm $Al_{0.75}Ga_{0.25}N$ QW and 3-nm $Al_{0.73}Ga_{0.27}N$ QW, the difference between the critical Al-contents (TE/TM-$\boldsymbol{R}_{sp}$ crossover and HH/CH valence subbands crossover) can be attributed to the combined effect of QCSE and band mixing effect. To further investigate the impact of the two effects on the critical Al-content, we simulated the structures with the critical Al-contents at which the valence subbands crossovers take place. Figure 3.6 plots the unpolarized momentum matrix elements ratio between C-CH1 and C-HH1 transitions as a function of QW thickness, together with the critical Al-contents difference between TE/TM $\boldsymbol{R_{sp}}$ crossover (x_1) and valence subbands crossover (x_2): $\Delta x = x_1 - x_2$. Note that for the structure with the critical Al-content at which valence subbands crossover, small separations between the three valence subbands and similar surface carrier densities can be expected. The results show the matrix element ratio increases significantly as the QW becomes wider because the thicker QW suffers more severe QCSE, which affects more on HH and LH than the lighter CH with wider hole wave function. Consequently, the large matrix elements ratio from thicker QW eventually translates to the big difference between TM-polarized $\boldsymbol{R_{sp}}$ and TE-polarized $\boldsymbol{R_{sp}}$ which requires lower Al-content to realize TE-$\boldsymbol{R_{sp}}$ =TM-$\boldsymbol{R_{sp}}$. This

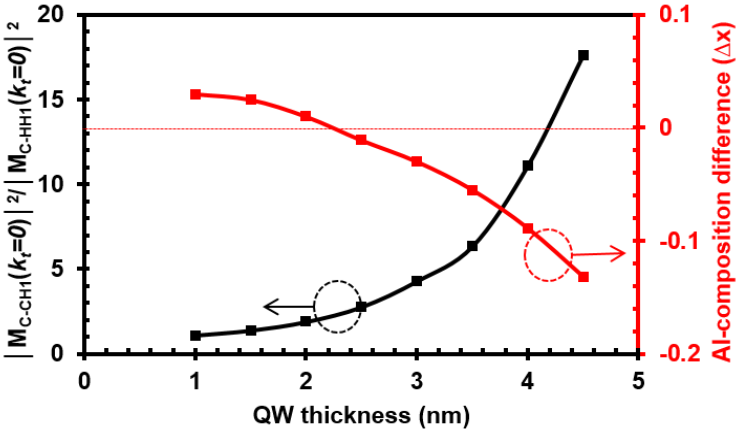

Figure 3.6: *Momentum matrix element ratio between C-CH1 and C-HH1 as a function of QW thickness at the valence subbands crossover point (black) and the critical Al-content difference between* $\boldsymbol{R_{sp}}$ *crossover* (x_1) *and valence subbands crossover* (x_2): $\Delta x = x_1 - x_2$ *as a function of QW thickness (red).*

fact can be verified by the critical Al-content difference curve. Specifically, for thinner QW, a positive value is observed for the Al-content difference, which can be explained by the fact that the difference between the matrix elements is small and the band mixing effect is the dominant factor influencing the total spontaneous emission rate. However, the large matrix elements difference induced by the QCSE becomes the foremost effect determining the polarization profile.

To verify the predicted critical Al-contents at difference QW thickness, the reported light polarization properties from AlGaN-based UV emitters are summarized and plotted in figure 3.7 [4], [5], [8], [9], [15], [16], [19]–[28]. A similar trend is observed in the figure, as compared to the calculated results shown in figure 3.3 (a). Specifically, a maximum critical Al-content is realized at the QW thickness of 1.5 nm with the value of x = 0.82. Note that there is a large variation between the reported values and the calculated results, which can be explained by the effect of the other factors such as the carrier density, temperature, substrate type, and barrier Al-content. Therefore, the effect of the QW thickness on the critical Al-content change is well-explained in this study and verified by the reported data, which is essential for the high-efficiency DUV QW designs. Specifically, we can pursue novel QW designs to engineer the polarization properties from the DUV LEDs which strongly determines the internal quantum efficiency and external quantum efficiency from the structure. We also examined the critical emission wavelengths at different QW thickness by summarizing the reported data, as shown in figure 3.8. An increasing trend is achieved from the experiments, which again indicates the accuracy of the simulations in this study.

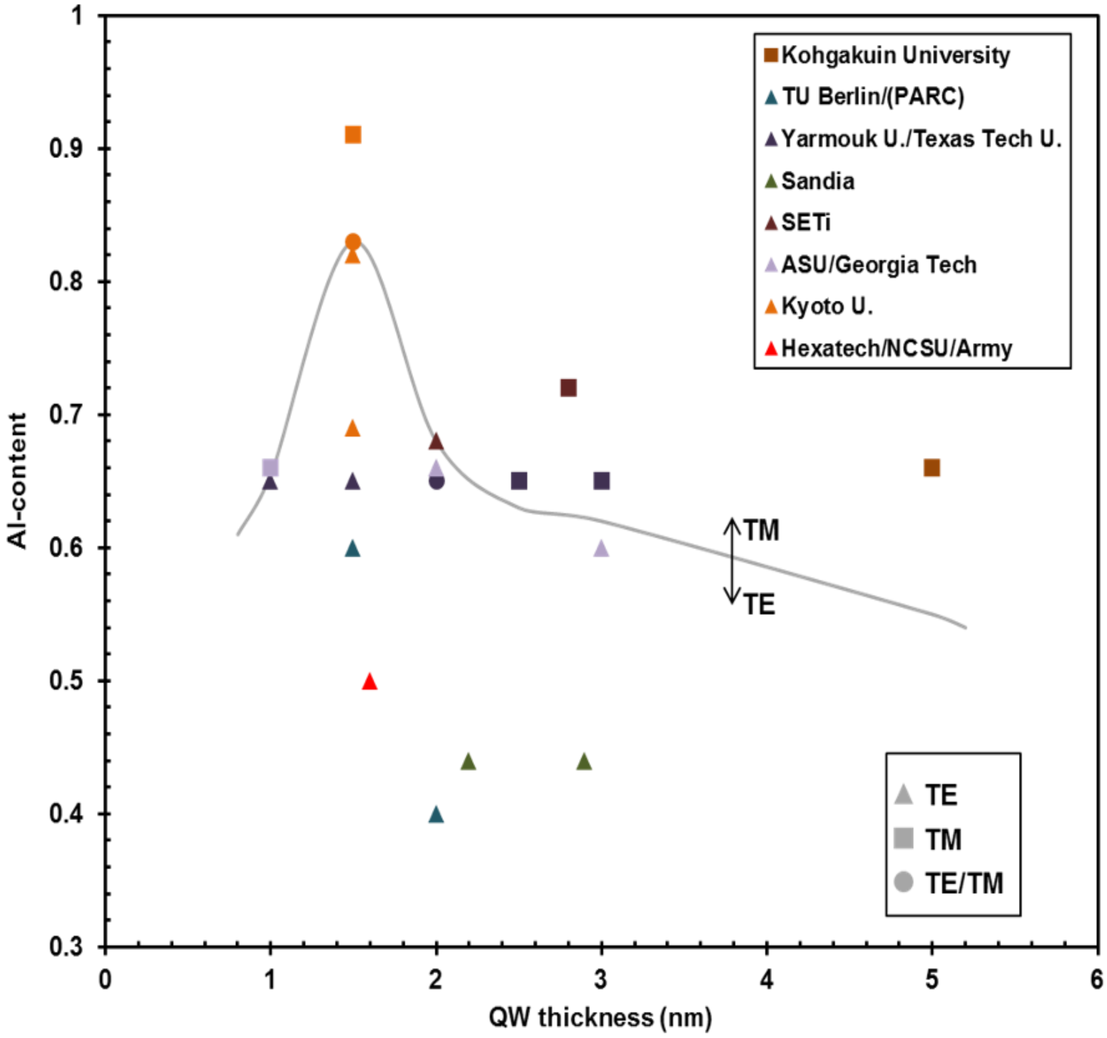

Figure 3.7*: Reported light polarization properties from AlGaN-based UV emitters with different QW thickness, categorized by Al-content [4], [5], [8], [9], [15], [16], [19]–[28].*

In summary, this study theoretically investigates the effect of the QW thickness on the light polarization properties of the AlGaN-based UV emitters. The critical Al-contents at which the valence subbands crossover takes place and at which the TE-polarized $\boldsymbol{R_{sp}}$ and TM-polarized $\boldsymbol{R_{sp}}$ have the same value are calculated. The results show the critical Al-content for the $\boldsymbol{R_{sp}}$ crossover increases for thin QW while decreases for thicker QW as the QW thickness increases. The difference between the two critical Al-contents can be explained by the combined effect of the QCSE and the band mixing effect. In addition, the results are verified by the reported light polarization properties from the AlGaN QW structures, which indicates this study is essential for the DUV emitter study since the polarization properties from the structure can be engineered to realize the high-efficiency devices.

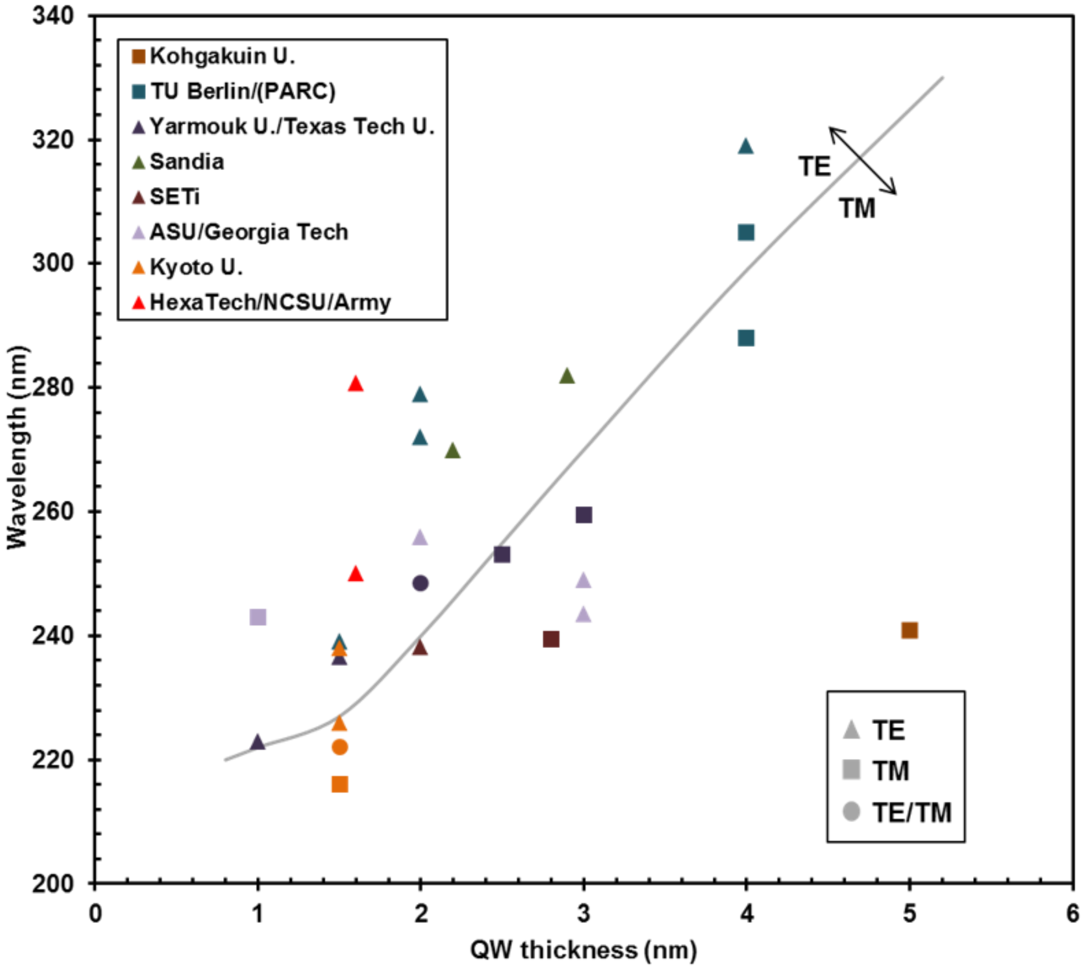

__Figure 3.8__: Reported light polarization properties from AlGaN-based UV emitters with different QW thickness, categorized by wavelength [4], [5], [8], [9], [15], [16], [19]–[28].

Reference for Chapter 3:

[1] S. Chuang and C. Chang, “k·p method for strained wurtzite semiconductors,” *Phys. Rev. B - Condens. Matter Mater. Phys.*, 54, 4, 2491, 1996.

[2] M. Kneissl and J. Rass, *III-Nitride Ultraviolet Emitters*, 227. Springer International Publishing Cham, 2016.

[3] J. Zhang, H. Zhao, and N. Tansu, “Effect of crystal-field split-off hole and heavy-hole bands crossover on gain characteristics of high Al-content AlGaN quantum well lasers,” *Appl. Phys. Lett.*, 97, 111105, 2010.

[4] H. Kawanishi, M. Senuma, and T. Nukui, “Anisotropic polarization characteristics of lasing and spontaneous surface and edge emissions from deep-ultraviolet (λ≈240 nm) AlGaN multiple-quantum-well lasers,” *Appl. Phys. Lett.*, 89, 041126, 2006.

[5] R. G. Banal, M. Funato, and Y. Kawakami, “Optical anisotropy in [0001]-oriented AlxGa1-xN/AlN quantum wells (x>0.69),” *Phys. Rev. B*, 79, 121308, 2009.

[6] J. E. Northrup *et al.*, “Effect of strain and barrier composition on the polarization of light emission from AlGaN/AlN quantum wells,” *Appl. Phys. Lett.*, 100, 021101, 2012.

[7] T. K. Sharma, D. Naveh, and E. Towe, “Strain-driven light-polarization switching in deep ultraviolet nitride emitters,” *Phys. Rev. B - Condens. Matter Mater. Phys.*, 84, 035305, 2011.

[8] T. M. Al Tahtamouni, J. Y. Lin, and H. X. Jiang, "Optical polarization in c-plane Al-rich AlN/Al xGa 1-xN single quantum wells," *Appl. Phys. Lett.*, 101, 042103, 2012.

[9] J. J. Wierer, I. Montaño, M. H. Crawford, and A. A. Allerman, "Effect of thickness and carrier density on the optical polarization of Al0.44Ga0.56N/Al0.55Ga0.45N quantum well layers," *J. Appl. Phys.*, 115, 174501, 2014.

[10] C. Reich *et al.*, "Strongly transverse-electric-polarized emission from deep ultraviolet AlGaN quantum well light emitting diodes," *Appl. Phys. Lett.*, 107, 142101, 2015.

[11] S.-H. Park and J.-I. Shim, "Carrier density dependence of polarization switching characteristics of light emission in deep-ultraviolet AlGaN/AlN quantum well structures," *Appl. Phys. Lett.*, 102, 221109, 2013.

[12] J. Bhattacharyya, S. Ghosh, and H. T. Grahn, "Are AlN and GaN substrates useful for the growth of non-polar nitride films for UV emission? The oscillator strength perspective," *Phys. Status Solidi Basic Res.*, 246, 6, 1184, 2009.

[13] C. P. Wang and Y. R. Wu, "Study of optical anisotropy in nonpolar and semipolar AlGaN quantum well deep ultraviolet light emission diode," *J. Appl. Phys.*, 112, 033104, 2012.

[14] R. G. Banal, Y. Taniyasu, and H. Yamamoto, "Deep-ultraviolet light emission properties of nonpolar M-plane AlGaN quantum wells," *Appl. Phys. Lett.*, 105, 053104, 2014.

[15] T. Kolbe *et al.*, “Optical polarization characteristics of ultraviolet (In)(Al)GaN multiple quantum well light emitting diodes,” *Appl. Phys. Lett.*, 97, 171105, 2010.

[16] X. H. Li *et al.*, “Low-threshold stimulated emission at 249 nm and 256 nm from AlGaN-based multiple-quantum-well lasers grown on sapphire substrates,” *Appl. Phys. Lett.*, 105, 141106, 2014.

[17] X. H. Li *et al.*, “Demonstration of transverse-magnetic deep-ultraviolet stimulated emission from AlGaN multiple-quantum-well lasers grown on a sapphire substrate,” *Appl. Phys. Lett.*, 106, 041115, 2015.

[18] S. L. Chuang, *Physics of photonic devices*. John Wiley & Sons, 2012.

[19] Z. Lochner *et al.*, “Deep-ultraviolet lasing at 243 nm from photo-pumped AlGaN/AlN heterostructure on AlN substrate,” *Appl. Phys. Lett.*, 102, 101110, 2013.

[20] T. T. Kao *et al.*, “Sub-250 nm low-threshold deep-ultraviolet AlGaN-based heterostructure laser employing HfO2/SiO2dielectric mirrors,” *Appl. Phys. Lett.*, 103, 211103, 2013.

[21] W. Guo *et al.*, “Stimulated emission and optical gain in AlGaN heterostructures grown on bulk AlN substrates,” *J. Appl. Phys.*, 115, 103108, 2014.

[22] M. Martens *et al.*, “Performance characteristics of UV-C AlGaN-based lasers grown on sapphire and bulk AlN substrates,” *IEEE Photonics Technol. Lett.*, 26, 4, 342, 2014.

[23] Y. S. Liu *et al.*, “Optically pumped AlGaN quantum-well lasers at sub-250 nm grown by MOCVD on AlN substrates,” *Phys. Status Solidi Curr. Top. Solid State Phys.*, 11, 2, 258, 2014.

[24] H. Kawanishi, M. Senuma, M. Yamamoto, E. Niikura, and T. Nukui, “Extremely weak surface emission from (0001) c-plane AlGaN multiple quantum well structure in deep-ultraviolet spectral region,” *Appl. Phys. Lett.*, 89, 081121, 2006.

[25] C. Reich *et al.*, “Strongly transverse-electric-polarized emission from deep ultraviolet AlGaN quantum well light emitting diodes,” *Appl. Phys. Lett.*, 107, 14, 1–6, 2015.

[26] X. H. Li *et al.*, “Demonstration of transverse-magnetic deep-ultraviolet stimulated emission from AlGaN multiple-quantum-well lasers grown on a sapphire substrate,” *Appl. Phys. Lett.*, 106, 4, 1–5, 2015.

[27] M. Lachab *et al.*, “Optical polarization control of photo-pumped stimulated emissions at 238nm from AlGaN multiple-quantum-well laser structures on AlN substrates,” *Appl. Phys. Express*, 10, 012702, 2017.

[28] J. Xie *et al.*, “Lasing and longitudinal cavity modes in photo-pumped deep ultraviolet AlGaN heterostructures,” *Appl. Phys. Lett.*, 102, 171102, 2013.

CHAPTER 4: Design Analysis of Al(In)GaN-Delta-GaN for Deep-Ultraviolet Emitters

In chapter 2, the physics of the conventional AlGaN QW for DUV LEDs, especially their band structure and optical properties, have been deeply discussed. In general terms, by using the conventional AlGaN-based QW, it is difficult to realize strong TE-polarized emission in the entire DUV regime. Specifically, for short wavelength emission (λ < 230 nm), the topmost valence band is CH subband, which leads to the dominant TM-polarized. Negligible TE-polarized light can be generated from the conventional AlGaN QW in this regime. For λ ~ 230 nm - 250 nm, HH/LH and CH subbands are mixed together with small energy separations, which is known as band mixing effect. As a result, the carriers are almost equally populated at those three subbands, causing the insufficient conduction band to HH transition and therefore TE-polarized photons generations. For longer emission wavelength (λ ~250 nm - 300 nm), the main challenge from the conventional AlGaN QW is the large polarization field induced QCSE, which results in low TE-polarized and TM-polarized $\boldsymbol{R_{sp}}$, although C-HH transition becomes dominant in this emission wavelength regime. In addition, previous discussion also points out that the TM photons are difficult to extract out from the top (bottom) of the device, as compared to TE-polarized photons. Therefore, the structures with strong TE-polarized emission are essential to realize high-efficiency DUV LEDs, which is, however, very challenging by the use of conventional AlGaN QWs.

To address this issue, one possible solution is the use of delta-QWs. Specifically, an ultra-thin layer with smaller bandgap is inserted into the center of conventional QW materials to form the stepped QW structure. Since the ultra-thin delta layer could provide a local minimum for electron and hole wave functions, which significantly reduces the QCSE from the structure, large spontaneous emission rate can then be achieved. In addition, the insertion of another material into the center of QW could also rearrange the valence subbands and engineer the optical polarization from the emissions. This concept has been demonstrated for visible LEDs by the use of InGaN-delta-InN QW [1] and for DUV regime by the use of AlGaN-delta-GaN QWs [2], [3]. In this Chapter, we continue investigating the use of delta-QWs for DUV LEDs. Specifically, the optical properties, as well as efficiencies from the AlGaN-delta-GaN QWs are studied. Besides, we also proposed and investigated the physics of AlInN system as an alternative for high-efficiency UV lasers. The band structure and optical properties for the both AlGaN-delta-GaN QW and proposed AlInN-delta-GaN QW, as well as the conventional AlGaN QWs (used for comparison) are calculated based on the self-consistent 6-band ***k·p*** formalism introduced in appendix B.

4.1 Engineer of AlGaN-Delta-GaN QW for UV Emitters

In this section, we introduce the AlGaN-delta-GaN QWs for DUV emitters. The valence band structure, optical properties such as spontaneous emission rate and optical gains, device efficiencies of the AlGaN-delta-GaN QWs are deeply investigated and discussed.

4.1.1 Concept and Valence Band Structures of AlGaN-Delta-GaN QW

Figure 4.1 schematically illustrates the concept of the AlGaN-delta-GaN QWs. Specifically, an ultra-thin layer with smaller bandgap material (GaN for this case) is inserted into the conventional AlGaN QW region to form the AlGaN-delta-GaN QW. For the new heterostructure, the total QW region consists of two AlGaN layers and an ultra-thin GaN layer, named as AlGaN sub-QW and delta-GaN layer, respectively. The thicknesses of the AlGaN sub-QW regions and delta-GaN layer are defined as d_1, d_2 and d. In this work, we only studied the case that AlGaN sub-QW regions are identical. Specifically, both Al-content and thickness of the two AlGaN sub-QW are the same ($\boldsymbol{d_1} = \boldsymbol{d_2} = 1.5$ nm).

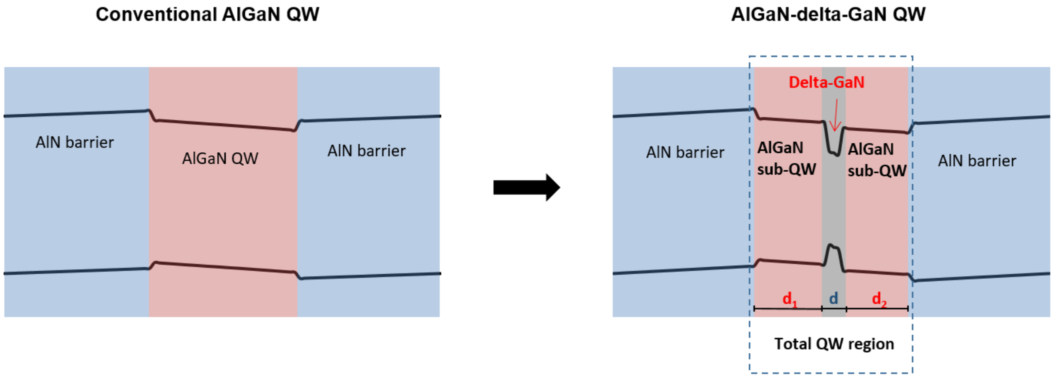

Figure 4.1: *Schematic illustration of AlGaN-delta-GaN QW structure.* $\boldsymbol{d_1}$, $\boldsymbol{d_2}$ *and* ***d*** *stands for the thicknesses of 1st and 2nd AlGaN sub-QW regions and delta-GaN layer*

To study the structural and optical properties from the AlGaN-delta-GaN QW structure, we use the self-consistent 6-band ***k·p*** model and Fermi's Golden Rule, which detailed described in appendix B. All the material parameters used in this chapter are presented in appendix A. Figure 4.2 (a) plots the band energy lineups, as well as the ground state electron and hole wave functions of an $Al_{0.8}Ga_{0.2}N$-delta-GaN QW with 3-Å delta-GaN. The thicknesses of the barrier and AlGaN sub-QW are set to be 3 nm and 1.5 nm, respectively. For comparison, a conventional 3-nm AlGaN QW with Al-content of 65% was investigated, as shown in figure 4.2 (b). The 65% Al-content was selected to achieve a similar emission wavelength with the AlGaN-delta-GaN QW. For the conventional $Al_{0.65}Ga_{0.35}N$ QW, it is clear that the ground state electron and hole wave functions are largely separated due to the existence of large polarization electric field. As a result, only 18.51% electron-hole wave function overlap can be realized. In contrast, the ground state electron and hole wave functions are pushed to the QW center from the $Al_{0.8}Ga_{0.2}N$-delta-GaN QW, which is attributed to the insertion of ultra-thin small bandgap GaN layer, leading to a significant electron-hole wave function overlap ($\boldsymbol{\Gamma_{e1\text{-}hh1}}$ = 70.57%). As explained in Appendix B, the overlap integral is responsible for matrix element value and the optical properties. Therefore, significant enhancement of the spontaneous emission rate can be expected by the use of $Al_{0.8}Ga_{0.2}N$-delta-GaN QW, as compared to that of the conventional $Al_{0.65}Ga_{0.35}N$ QW.

To show the influence of the insertion of the ultra-thin delta-GaN layer on valence subbands, the valence band structures from $Al_{0.8}Ga_{0.2}N$ QW with and without 3-Å delta-GaN layer were calculated and compared in this work, as shown in figure 4.2 (c) and (d). The carrier density of $\boldsymbol{n} = 5 \times 10^{18}$ cm^{-3} is used here, which is a typical value for LED application. For 3-nm $Al_{0.8}Ga_{0.2}N$ QW, the Al-content is higher than predicted valence band crossover point (detailed discussed in chapter 3), ground state CH subband is the topmost valence subband, followed by the HH and LH subbands. However, for $Al_{0.8}Ga_{0.2}N$-delta-GaN QW, the insertion of the delta-GaN layer enables the valence band rearrangement. Specifically, the ground state HH is pushed to the top of the valence band, which is critical to realize dominant TE-polarized emission from the structure. Note that the energy separation between HH1/LH1 and CH1 is large, which leads to many advantages. Specifically, majority of the carriers populated at HH1 and LH1 subbands, while very little at the CH subband, which suppresses the TM-polarized photons generated. Besides, weak LH1 and CH1 coupling in this structure due to the large energy separation, which causes that majority of the photons generated by C-LH1 are TE-polarized. Therefore, the insertion of delta-GaN layer is beneficial to generate TE-

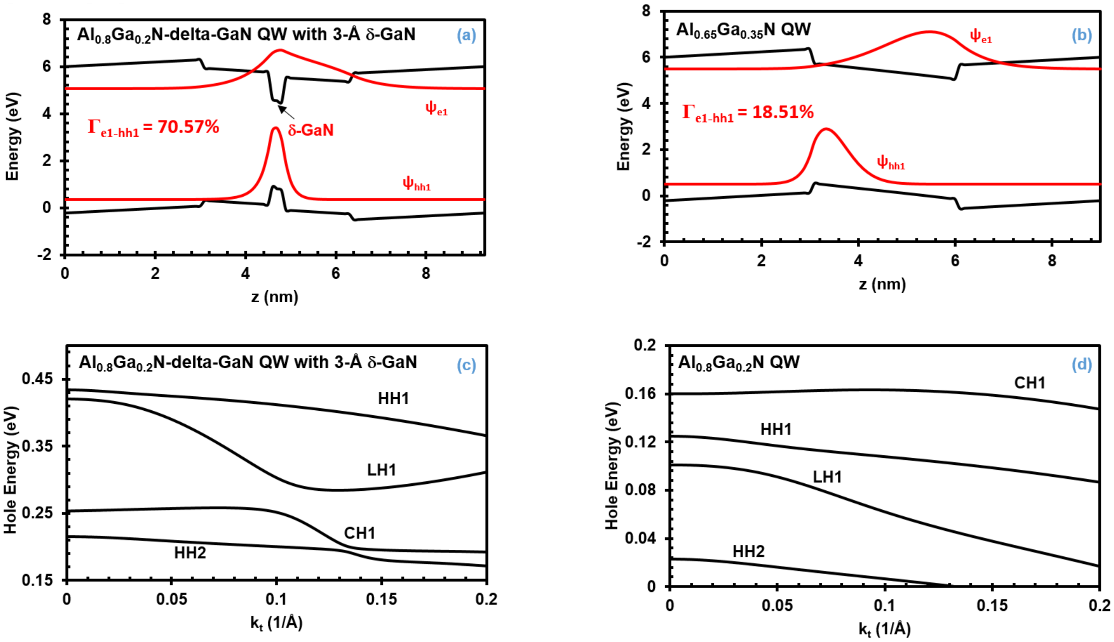

Figure 4.2: *Band energy lineups with electron and hole wave functions of (a) $Al_{0.8}Ga_{0.2}N$-delta-GaN QW with 3-Å delta-GaN, and (b) 3-nm $Al_{0.65}Ga_{0.35}N$ QW; Valence band structures of (c) $Al_{0.8}Ga_{0.2}N$-delta-GaN QW with 3-Å delta-GaN, and (d) 3-nm $Al_{0.8}Ga_{0.2}N$ QW. Carrier density is* $\boldsymbol{n} = 5 \times 10^{18}$ *cm*$^{-3}$.

4.1.2 Optical Characteristics of AlGaN-Delta-GaN QW

The polarization properties after the ultra-thin GaN layer insertion were studied and presented in figure 4.3 (a). Both TE- and TM-polarized spontaneous emission rates from the $Al_{0.8}Ga_{0.2}N$-delta-GaN QW and the $Al_{0.8}Ga_{0.2}N$ QW are calculated at carrier density of $\boldsymbol{n} = 5 \times 10^{18}$ cm^{-3}. As predicted, dominant TE-polarized emission while negligible TM-polarized emission are realized for the $Al_{0.8}Ga_{0.2}N$-delta-GaN QW with 3-Å delta-GaN, attributing to the valence subbands rearrangement, specifically, topmost HH valence subband. However for $Al_{0.8}Ga_{0.2}N$ QW, the dominant C-CH1 transition leads to the larger TM-polarized spontaneous emission rate, as compared to TE-polarized. Although the energy separation between CH1 and HH1 is small, the wider hole wave function for CH hole (due to small effective mass of CH hole) leads to larger overlap integral, as compared to the HH hole, which is responsible for the large difference in TM- and TE-polarized spontaneous emission rate values. Note that after the insertion of ultra-thin GaN layer, the peak emission wavelength is adjusted as well. 246 nm and 224 nm are observed from the $Al_{0.8}Ga_{0.2}N$-delta-GaN QW and the $Al_{0.8}Ga_{0.2}N$ QW, respectively.

The spontaneous emission spectra for $Al_{0.8}Ga_{0.2}N$-delta-GaN QW with different carrier density $\boldsymbol{n} = 1 - 5 \times 10^{18}$ cm^{-3} were also presented in figure 4.3 (a) (dash lines). A slight blue-shift from the peaks of the spontaneous emission spectra is exhibited, which is attributed to the state filing effect.

Besides of the polarization properties engineering, another benefit of the AlGaN-delta-GaN QW is the significant enhancement in electron-hole wave function overlap. Figure 4.3 (b) plots the $\boldsymbol{R_{sp}}$ value as a function of carrier density up to density $\boldsymbol{n} = 1 \times 10^{19}$ cm^{-3} for both the $Al_{0.8}Ga_{0.2}N$-delta-GaN QW and the conventional 3-nm $Al_{0.65}Ga_{0.35}N$ QW. It is clear that the $\boldsymbol{R_{sp}}$ values from the $Al_{0.8}Ga_{0.2}N$-delta-GaN QW are significantly larger than that from the $Al_{0.65}Ga_{0.35}N$ QW for entire carrier density range due to the improved electron-hole wave function overlap. Specifically, at carrier density of $\boldsymbol{n} = 5 \times 10^{18}$ cm^{-3}, the improved overlap integral ($\boldsymbol{\Gamma_{e1\text{-}hh1}}$ = 70.57% vs. $\boldsymbol{\Gamma_{e1\text{-}hh1}}$ = 18.51%) results in a large $\boldsymbol{R_{sp}}$ value of 1.391×10^{28} cm^{-3} from $Al_{0.8}Ga_{0.2}N$-delta-GaN QW.

As mentioned in previous chapters, the $\boldsymbol{R_{sp}}$ value directly determines the device radiative recombination efficiency and therefore the internal quantum efficiency. Follow the simple ABC model, the radiative recombination efficiency can be calculated as: $\eta_{rad} = \frac{R_{sp}}{A\cdot n+R_{sp}+C\cdot n^3}$, where A and C stand for SRH coefficient and Auger coefficient. Here we use A = 1×10^{7} s^{-1} and C = 1×10^{-33} cm^6/s for efficiency calculations. By the use of the $Al_{0.8}Ga_{0.2}N$-delta-GaN QW, up to 91.39% radiative recombination efficiency can be achieved in the typical LED operation carrier density regime. On the contrast, the radiative recombination efficiency can barely reach 33.47% at carrier density of $\boldsymbol{n} = 5 \times 10^{18}$ cm^{-3}, which combines with the low light extraction efficiency (~10%) and leads to the extremely low external quantum efficiency of ~3% even without considering carrier injection efficiency. In summary, the large TE-polarized $\boldsymbol{R_{sp}}$ generates from the AlGaN-delta-GaN QW is promising for realizing high-efficiency DUV LEDs.

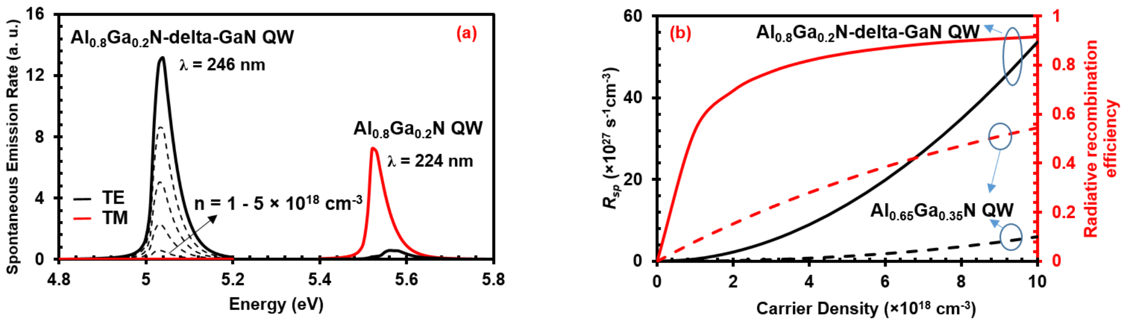

***Figure 4.3**: (a) Polarized spontaneous emission spectra from the $Al_{0.8}Ga_{0.2}N$-delta-GaN QW with 3-Å delta-GaN and the 3-nm $Al_{0.8}Ga_{0.2}N$ QW at carrier density of $\boldsymbol{n} = 5 \times 10^{18}$ cm^{-3}; spontaneous emission spectra from the $Al_{0.8}Ga_{0.2}N$-delta-GaN QW with different carrier density of $\boldsymbol{n} = 1 - 5 \times 10^{18}$ cm^{-3} (dash line); (b) $\boldsymbol{R_{sp}}$ (black) and radiative recombination efficiency (red) as a function of carrier density for the $Al_{0.8}Ga_{0.2}N$-delta-GaN QW (solid line) and the $Al_{0.65}Ga_{0.35}N$-delta-GaN QW (dash line)*

4.1.3 Engineering of AlGaN-Delta-GaN QW

To show the flexibility of the AlGaN-delta-GaN QW designs, structures with different thicknesses of the delta-GaN layer and different sub-QW Al-contents were studied. For the conventional AlGaN QW, the emission wavelength from the structure is mainly adjusted by the Al-content in the active region. Although the thickness of the QW also strongly influences the emission wavelength, it could cause polarization properties and device performance fluctuations as well, which make it undesirable for wavelength engineering. However, for AlGaN-delta-GaN QWs, there are enough variables to adjust to achieve target emission wavelength without sacrificing the supreme optical performance of the delta-QW designs.

Figure 4.4 summarizes the R_{sp} values and emission wavelengths from different AlGaN-delta-GaN QW designs. All the results were collected at carrier density of $n = 5 \times 10^{18}$ cm^{-3}. The emission wavelength is sensitive to the delta-GaN layer thickness, as presented by the red dots in figure 4.4. By adjusting the delta-GaN thickness from 3 Å to 10 Å, the emission wavelength switches from 246 nm to 297 nm. It is noteworthy that large TE-polarized R_{sp} value can be maintained within this regime, which is beneficial for DUV LED designs. Further increase the delta-GaN thickness to 1.5 nm, the emission wavelength reaches 325 nm while the R_{sp} value drops significantly. This is because the structure with large delta-GaN layer thickness works more like a single QW structure instead of the delta-QW. Since the thickness of the delta-GaN layer is critical to the emission wavelength, the epitaxy of this AlGaN-delta-GaN QW structure requires precise control down to monolayer, which make it very challenging to realize experimentally. However, thanks to the development of the MBE and MOCVD during the past decades, we successfully grew the AlGaN-delta-GaN QWs with controllable delta-GaN thickness, which will detailed discussed in chapter 6.

The thickness of the delta-GaN layer is a coarse adjustment on the emission wavelength. However, to precisely control the emission wavelength, another fine adjustment knob is required, which can be achieved by engineering the sub-QW Al-content. As presented by black dots in figure 4.4, structures with different sub-QW Al-contents were compared. By tuning the Al-content from $\boldsymbol{x}$ = 0.8 to $\boldsymbol{x}$ = 0.6, the emission wavelength is shifted from 246 nm to 266 nm, which covers the entire range of wavelength gap between structures with 3-Å and 5-Å delta-GaN. Although the $\boldsymbol{R_{sp}}$ value drops if relatively lower Al-content is used, the value is still much better than that from the conventional AlGaN QW structure. Furthermore, this issue can be improved by optimizing the AlGaN-delta-GaN QW design. Specifically, there are more than one possible combinations of sub-QW Al-content and delta-GaN thickness to achieve target emission wavelength. For example, both thinner delta-GaN layer with lower sub-QW Al-content and thicker delta-GaN layer with higher sub-QW Al-content can meet the requirements.

Besides the sub-QW Al-content and delta-GaN thickness, the emission wavelength and device optical performance can also be engineered by the use of asymmetric AlGaN-delta-GaN QW designs, which is detailed discussed in ***ref***. [3]. Specifically, by adjusting the thickness distribution of the sub-QW region, i. e. $\boldsymbol{d_1}$ = 18 Å, 20% enhancement on the optical gain can be achieved, as compared to the symmetric AlGaN-delta-GaN QW design. In addition, the optical properties of the structure can be further boosted by using different Al-content AlGaN materials for sub-QW layers [3]. In summary, the emission wavelength of the AlGaN-delta-GaN QW can be engineered within the entire DUV range while maintaining large TE-polairzed ***R_{sp}*** value, which is extremely promising for DUV LED applications.

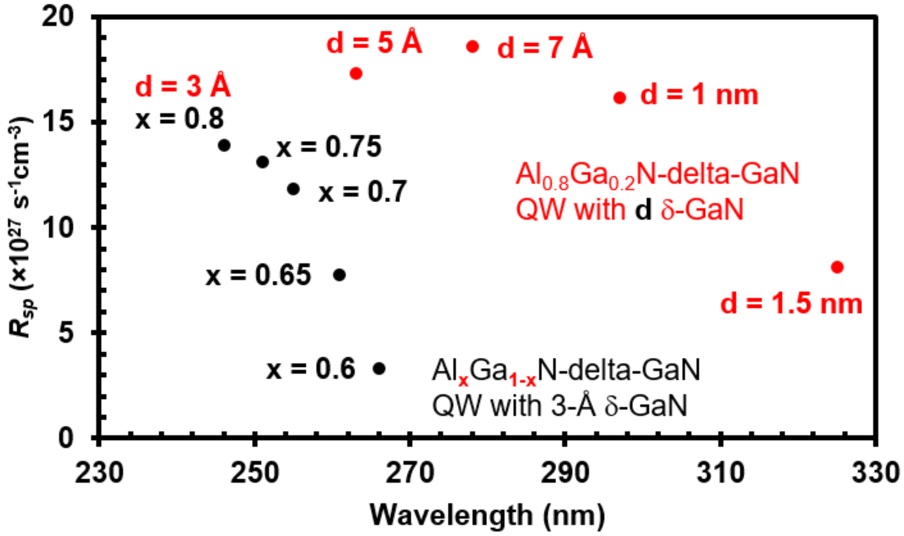

***Figure 4.4**: **R_{sp}** values and emission wavelengths from AlGaN-delta-GaN QWs with different delta-GaN thicknesses (red) from **d** = 3 – 15 Å and different sub-QW Al-contents (black) from **x** = 0.6 – 0.8. Carrier density is **n** = 5 × 10^{18} cm^{-3}.*

4.1.4 AlGaN-Delta-GaN QW for laser applications

By employing the AlGaN-delta-GaN QW, the valence subband can be rearranged into TE-preferred orders and the electron-hole wave function overlap can be significantly improved. Therefore, it is suitable for realizing high-efficiency TE-polarized lasers in DUV regime. Figure 4.5 plots the TE-polarized optical gain spectra from $Al_{0.8}Ga_{0.2}N$-delta-GaN QW and $Al_{0.7}Ga_{0.3}N$-delta-GaN QW at carrier density of ***n*** = 5 × 10^{19} cm^{-3}. Both delta-QW designs have 3-Å delta-GaN. Up to 3610.18 cm-1 and 3513.2 cm-1 TE-polarized peak optical gain were achieved from $Al_{0.8}Ga_{0.2}N$-delta-GaN QW and $Al_{0.7}Ga_{0.3}N$-delta-GaN QW at 252 nm and 244 nm, respectively. Red lines shown in figure 4.5 present the peak optical gain value as a function of carrier density up to ***n*** = 5 ×

10^{19} cm^{-3} from both delta-QW structures. The transparency carrier density (***n_{tr}***) was observed at ***n_{tr}*** ~ 1.8 × 10^{19} cm^{-3} for both structures. More discussion on the AlGaN-delta-GaN QW for laser applications can be found in ***ref.*** [2], [3].

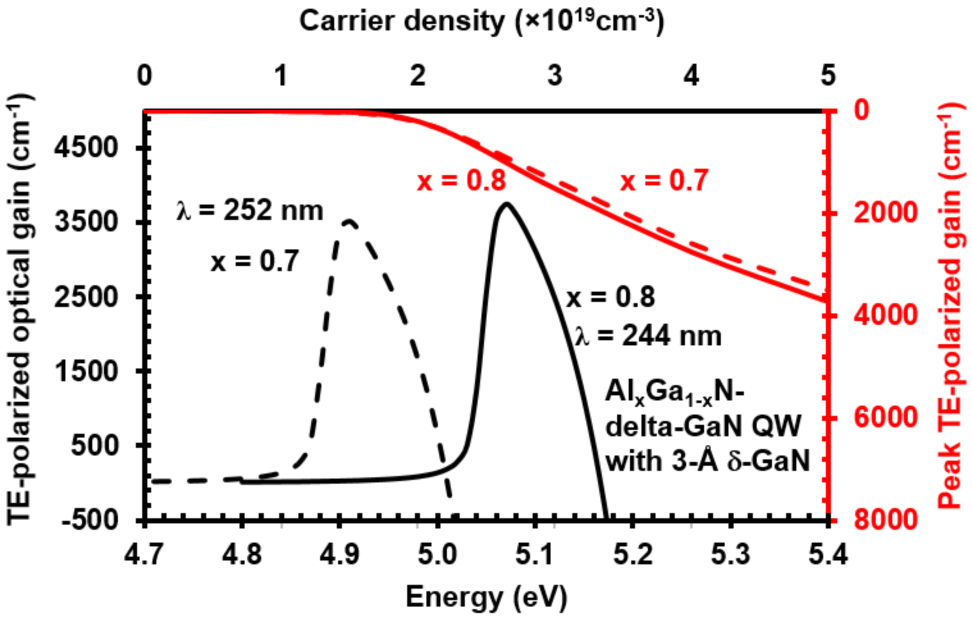

***Figure 4.5**: TE-polarized optical gain spectra (black lines) from $Al_{0.8}Ga_{0.2}N$-delta-GaN QW with 3-Å delta-GaN (solid) and $Al_{0.7}Ga_{0.3}N$-delta-GaN QW with 3-Å delta-GaN (dash), carrier density is **n** = 5 × 10^{19} cm^{-3}. Peak TE-polarized gain as a function of carrier density up to **n** = 5 × 10^{98} cm^{-3} (red).*

4.2 Proposal and Physics of AlInN-Delta-GaN QW UV Lasers

Conventionally, AlGaN-based QWs are widely used as the active regions for DUV emitters, especially UV lasers. However, high-efficiency electrically injected UV lasers are still very challenging below 300 nm as the corresponding AlGaN QWs suffer from severe band-mixing effect and QCSE. Therefore, the progress of the electrically injected UV lasers has only been shown in near-UV regime (330 nm – 370 nm) [4]–[9] until recently. By the use of high quality AlN substrate with a dislocation density of 10^3-10^4 cm^{-2}, a record 271.8 nm DUV laser for room temperature operation was developed in

2019 [10]. However, it is still very challenging to realize electrically DUV lasers based on the conventional AlGaN QWs in general. Therefore, exploring alternative materials will be a possible solution for high-efficiency DUV emitters.

Theoretically, high Al-content AlInN alloys can also serve as active regions for UV lasers and there has been emerging interests in using this novel large bandgap material. However, the progress on the use of such alloys has been limited by the epitaxial growth challenge and the understanding on the degeneration valence subbands. Recently, AlInN thin films have been successfully carried out by MOCVD with In-content up to 9% on c-plane AlN template [11]–[14], and up to 55% on semipolar AlN substrate [15]. Consequently, there has been a theoretical attempt on using AlInN as the active region for UV lasers [16]. Nevertheless, the studies on the physics of AlInN-based QW, especially the degeneration valence subbands, are still lacking, which is essential for the high-efficiency UV LED designs.

Therefore, in this section, we proposed and investigated the band structure and optical gain characteristics of AlInN-based QW for UV lasers. Specifically, we design an AlInN-delta-GaN QW with an ultra-thin GaN layer inserted at the center of a 24-Å staggered $Al_{0.91}In_{0.09}N$/ $Al_{0.82}In_{0.18}N$ QW. The whole QW structure is designed on the AlN substrate and its optical properties are compared with that of the conventional AlGaN QW at similar emission wavelength regime [17].

4.2.1 *Concept and Valence Band Structures of AlInN-Delta-GaN QW*

The energy band lineups and the corresponding ground state electron and hole wavefunctions of the proposed AlInN-delta-GaN QWs are shown in figure 4.6 (a). The

In-contents of the 24-Å staggered $Al_{0.91}In_{0.09}N/Al_{0.82}In_{0.18}N$ QW are selected based on the experimentally reported values of AlInN epitaxial growth [11]–[14]. In addition, the use of the staggered AlInN layers could ensure better confinement of electron and hole wavefunctions. Meanwhile, the incorporation of the delta-QW design could further localize the electron and hole wavefunctions toward the QW centers, large wavefunction overlap is observed from the proposed AlInN-delta-GaN QW. For comparison, the band structures for conventional $Al_{0.54}Ga_{0.46}N$ QW and staggered AlInN QW are plotted in figure 4.6 (b) and (c). The 54% Al-content in the conventional AlGaN QW is chosen to achieve the similar emission wavelength with the proposed AlInN-delta-GaN QW. Large lattice mismatch between the AlGaN and AlN substrate/barrier induces relatively large intrinsic polarization electric field, which leads to a large separation of the electron and hole wavefunctions. Note that the use of staggered AlInN QW could slightly push the wavefunctions toward the center. However, the shallow QW results in a weak quantum confinement, which again proves the importance of employing the proposed AlInN-delta-GaN QW structure.

To better understand the physics of the proposed QW structure, the valence band structures for the 24-Å staggered $Al_{0.91}In_{0.09}N/ Al_{0.82}In_{0.18}N$-delta-GaN QW, the conventional 24 Å $Al_{0.54}Ga_{0.46}N$ QW and the staggered AlInN QW are compared and plotted in figure 4.6 (d), (e) and (f), respectively. For the conventional $Al_{0.54}Ga_{0.46}N$ QW, the Al-content is lower than the critical Al-content where TE/TM-polarized $\boldsymbol{R_{sp}}$ crossover occurs (~68%) [18]. Therefore, the energy level of HH subband is higher than that of the CH subband. On the other hand, the staggered AlInN QW also shows the HH subband on the top of the valence band. However, the energy separation between HH and CH is relatively small, which will lead to the insufficient carrier population at HH subband. For the 24-Å staggered $Al_{0.91}In_{0.09}N$/ $Al_{0.82}In_{0.18}N$-delta-GaN QW, the insertion of the delta-GaN layer ensures the HH subband occupies the highest energy level. Note that there is no CH subband located at the four highest valence band energy levels and hence dominant C-HH transition and large TE-polarized optical gain can be expected.

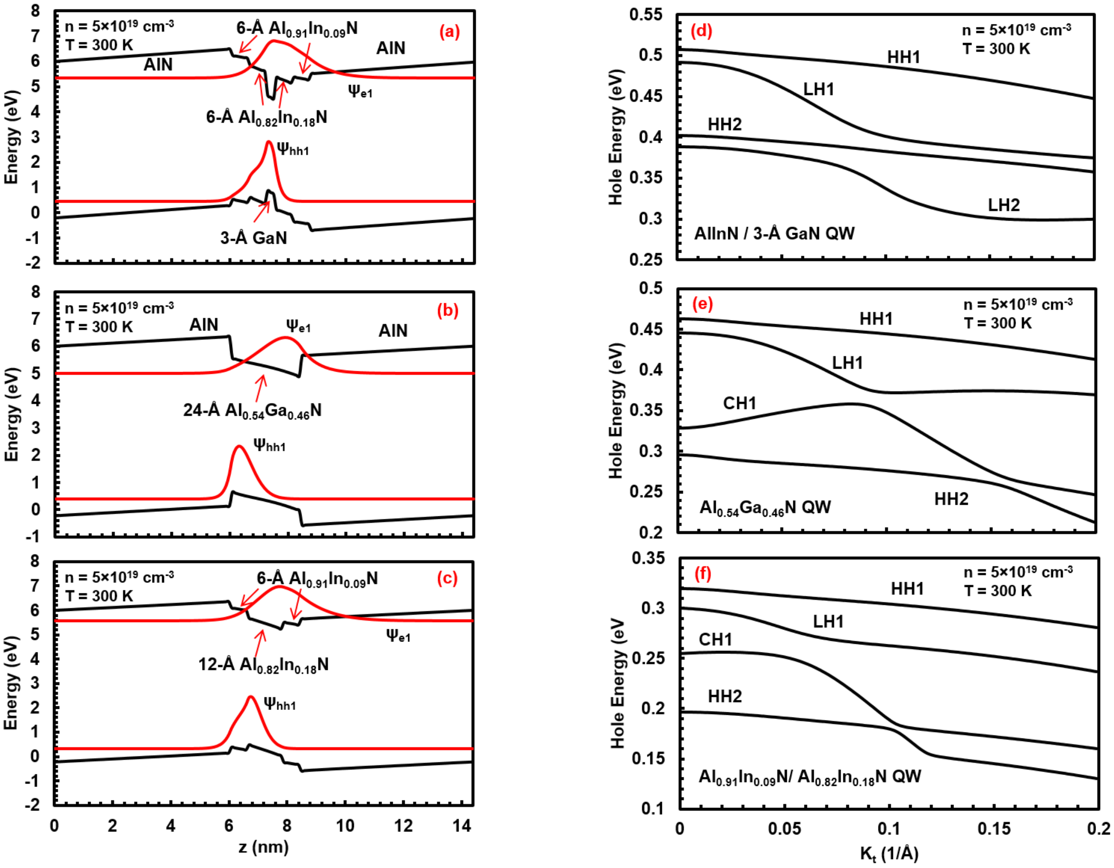

***Figure 4.6**: Energy band lineups for the (a) 24-Å AlInN-delta-GaN QW; (b) 24-Å conventional AlGaN QW; (c) 24-Å staggered AlInN QW with ground state electron wavefunction (ψ_{e1}) and hole wavefunction (ψ_{hh1}). Valence band structure for the (d) 24-Å AlInN-delta-GaN QW; (e) 24-Å conventional AlGaN QW; (f) 24-Å staggered AlInN QW at room temperature. The carrier density is 5×10^{19} cm^{-3}.*

4.2.2 Optical Properties of AlInN-Delta-GaN QW

The crucial role of the delta-GaN layer in the AlInN QW in optical gain characteristics is examined in figure 4.7. Both TE- and TM-polarized optical gain spectra are taken into comparison for AlInN-delta-GaN QW, AlGaN QW, and staggered AlInN QW. The use of the AlInN-delta-GaN QW leads to large peak TE-gain at λ ~255 nm, which is 2750 cm^{-1} with $\boldsymbol{n} = 5 \times 10^{19}$ cm^{-3} attributing to the improved wavefunction overlap and dominant C-HH transition. For the conventional $Al_{0.54}Ga_{0.46}N$ QW, its TE-polarized gain is larger than its TM-polarized gain as the C-HH transition still dominates before the valence subbands crossover. However, the peak TE-polarized gain of the $Al_{0.54}Ga_{0.46}N$ QW ($\boldsymbol{g}_{\mathbf{peak}}$ ~ 840 cm^{-1}) is much smaller than that of the AlInN-delta-GaN QW at same wavelength due to band mixing effect and smaller wavefunction overlap. To study the effect of delta-layer insertion, it is also interesting to compare the optical gain of 24-Å staggered $Al_{0.91}In_{0.09}N$/ $Al_{0.82}In_{0.18}N$-delta-GaN QW with the 24-Å staggered $Al_{0.91}In_{0.09}N$/ $Al_{0.82}In_{0.18}N$ QW. As shown in figure 4.7, the TE gain $\boldsymbol{g}_{\mathbf{peak}}$ ~ 835.8 cm^{-1} was obtained at $\boldsymbol{\lambda} = 234$ nm for the use of staggered $Al_{0.91}In_{0.09}N$/ $Al_{0.82}In_{0.18}N$ QW only, which is also significantly lower than that of the $Al_{0.91}In_{0.09}N$/ $Al_{0.82}In_{0.18}N$-delta-GaN QW as there is no delta-GaN layer to localize the wavefunctions toward the center of the QW. Note that there is a red-shift after the insertion of the delta-GaN layer due to the band structure adjustment.

Although the In-content in the AlInN-based QW is limited by the epitaxial growth, the emission wavelength can be tuned by engineering other structural parameters. To show the flexibility in the AlInN-delta-GaN QW design, figure 4.8 plots the TE-polarized

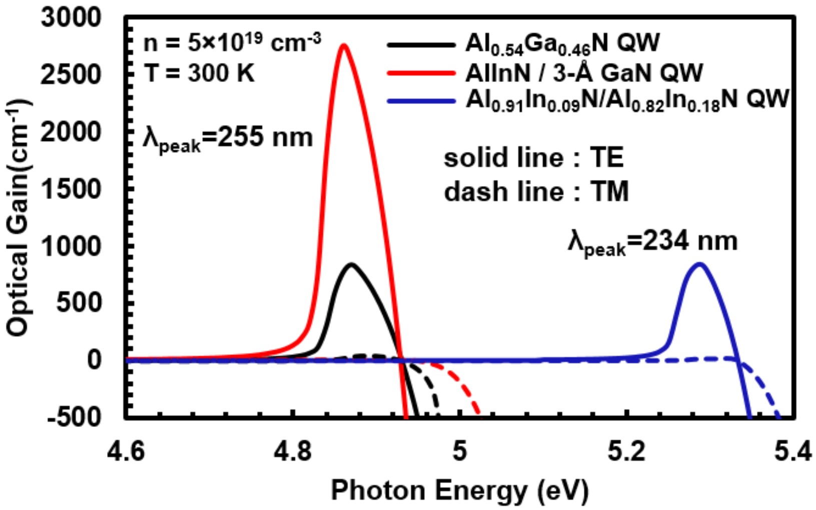

Figure 4.7: *TE-polarized (solid line) and TM-polarized (dash line) optical gain spectra of 24-Å conventional AlGaN QW, 24-Å AlInN-delta-GaN QW and 6-Å* $Al_{0.91}In_{0.09}N$*/ 12-Å* $Al_{0.82}In_{0.18}N$*/ 6-Å* $Al_{0.91}In_{0.09}N$ *QW. The carrier density is* 5×10^{19} cm^{-3}.

optical gain for AlInN-delta-GaN QW structures with different QW thickness at room temperature. For AlInN-delta-GaN QW with thin delta GaN layer less than 9 Å, varying the delta GaN layer thickness will still give emission wavelength in the mid-UV regime while maintaining large TE optical gain. Specifically, up to 3726 cm^{-1} and 3712 cm^{-1} optical gain can be obtained with λ = 293 nm and λ = 276 nm, respectively, which is very challenging to realize in conventional AlGaN QW structures. Further increasing the thickness of the delta GaN layer will rapidly reduce the TE optical gain as well as shift the peak emission wavelength to the near UV regime. This relative low optical gain observed at near-UV regime indicates that the active region behaves like GaN single QW (SQW). Thus the novel AlInN-delta-GaN QW structure with ultrathin GaN layer (d = 3 - 9 Å) is demonstrated to be an excellent candidate to achieve high gain for DUV lasers with flexibility in epitaxy growth.

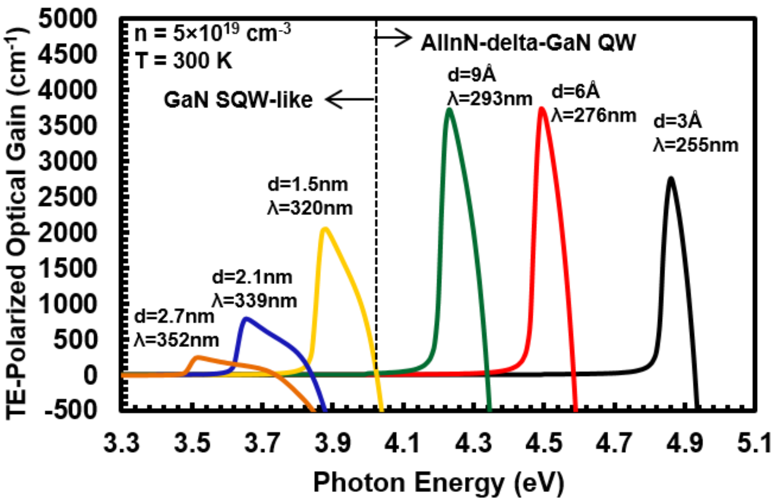

***Figure 4.8**: TE-polarized optical gain spectra of 24-Å AlInN-delta-GaN QW with the delta-GaN layer thickness of 3 Å to 27 Å. The carrier density is 5×10^{19} cm^{-3}.*

Figure 4.9 (a) compares the TE-polarized gain spectra with different carrier density up to 6×10^{19} cm^{-3} for AlInN-delta-GaN QW and $Al_{0.54}Ga_{0.46}N$ QW at 300 K. For typical laser carrier density ($\boldsymbol{n}$ = 4×10^{19} cm^{-3} - 6×10^{19} cm^{-3}), ~4.1 – 2.7 times enhancement of TE-polarized peak gain was observed from the AlInN-delta-GaN QW compared to that from the conventional AlGaN QW. This again confirms that the delta QW design is promising for UV laser application as the structure ensures that the majority of the carriers are populating the HH1 subband under higher level injection. Note that both QWs exhibit wavelength blue shift at higher carrier density due to the carrier screening effect.

Figure 4.9 (b) summarized the peak TE-polarized optical gain as a function of carrier density for both the AlInN-delta-GaN QW and the conventional AlGaN QW at room temperature. The transparency carrier densities ($\boldsymbol{n_{tr}}$) are 2.2×10^{19} cm^{-3} and 2.6×10^{19} cm^{-3} for both the $Al_{0.91}In_{0.09}N$/ $Al_{0.82}In_{0.18}N$-delta-GaN QW and $Al_{0.54}Ga_{0.46}N$ QW, respectively. The peak optical gain of AlInN-delta-GaN QW surged to 3600 cm^{-1} at $\boldsymbol{n}$ =

6×10^{19} cm^{-3}, which is ~3 times larger than that of AlGaN QW at the same carrier density. This significant enhancement in the optical gain of AlInN-delta-GaN QW again implies the promising potential for highly efficient UV laser with wavelength down to 250 nm. Furthermore, the threshold properties of AlInN-delta-GaN QW UV lasers were analyzed with laser structure similar in ***ref***. [19]. The threshold gain ($\boldsymbol{g_{th}}$) was estimated as ~1250 cm^{-1} with cavity length as 500 μm, optical confinement factor as 0.02, mirror loss as 11 cm^{-1}, and the internal loss as 14 cm [2], [19]. Thus, the threshold carrier densities ($\boldsymbol{n_{th}}$) are obtained as 5.94×10^{19}cm^{-3} and 3.58×10^{19}cm^{-3} for Al$_{0.54}$Ga$_{0.46}$N QW and AlInN-delta-GaN QW, respectively. It can be concluded that 1.7 times smaller threshold can be achieved by the use of the AlInN-delta-GaN QW UV laser.

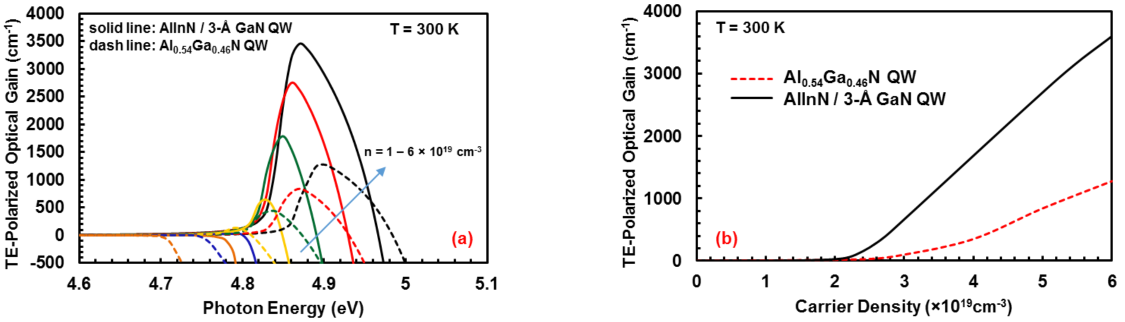

Figure 4.9*: (a) TE-polarized optical gain spectra of 24-Å AlInN-delta-GaN QW and 24-Å conventional AlGaN QW for carrier density from 1×10^{19} cm^{-3} to 6×10^{19} cm^{-3}. (b) TE-polarized peak gain as a function of carrier density for 24-Å AlInN-delta-GaN QW and 24-Å conventional AlGaN QW.*

4.3 Summary

In summary, this chapter introduces and investigates the use of AlGaN-delta-GaN QW for DUV LED and laser applications. The insertion of the ultra-thin delta-GaN layer could not only improve the wave function overlap integral, but rearrange the valence subbands with HH on the top. As a result, the TE-polarized spontaneous emission rate is improved by 10 times, as compared to the conventional AlGaN QW at same emission wavelength. Up to 91.39% radiative recombination efficiency can be realized by the use of $Al_{0.8}Ga_{0.2}N$-delta-GaN QW with 3-Å delta-GaN, which is much higher than that from the conventional AlGaN QW (33.47%). Therefore, the AlGaN-delta-GaN QW have shown great potential for high-efficiency DUV LEDs and lasers.

This chapter also explores the use of AlInN-delta-GaN QW for UV lasers. The optical gain characteristics of the AlInN-delta-GaN QW are compared to that of conventional AlGaN QW structure with the wavelength ranging from ~250 nm to ~300 nm. Like AlGaN-delta-GaN QW, the insertion of GaN ultra-thin layer results in dominant C-HH transition and improved electron and hole wavefunction overlap, which leads to up to 3-times enhancement in TE optical gain compared to that of the AlGaN QW. Up to 3726 cm^{-1} TE optical gain can be maintained by tuning the thickness of the delta GaN layer at mid-UV regime (280 nm-300 nm). Significantly reduced threshold carrier density can also be observed by the AlInN-delta-GaN QW UV laser at 250 nm, attributing from the large overlap design. Therefore, it is anticipated that the proposed AlInN-delta-GaN structure, with improved understanding in physics, could serve as a promising alternative active region for high-efficiency UV lasers.

.

Reference for Chapter 4:

[1] H. Zhao, G. Liu, and N. Tansu, "Analysis of InGaN-delta-InN quantum wells for light-emitting diodes," *Appl. Phys. Lett.*, 97, 131114, 2010.

[2] J. Zhang, H. Zhao, and N. Tansu, "Large optical gain AlGaN-delta-GaN quantum wells laser active regions in mid- and deep-ultraviolet spectral regimes," *Appl. Phys. Lett.*, 98, 171111, 2011.

[3] J. Zhang and N. Tansu, "Engineering of AlGaN-delta-GaN quantum-well gain media for mid- and deep-ultraviolet lasers," *IEEE Photonics J.*, 5, 2, 2013.

[4] H. Yoshida, Y. Yamashita, M. Kuwabara, and H. Kan, "Demonstration of an ultraviolet 336 nm AlGaN multiple-quantum-well laser diode," *Appl. Phys. Lett.*, 93, 241106, 2008.

[5] H. Yoshida, M. Kuwabara, Y. Yamashita, Y. Takagi, K. Uchiyama, and H. Kan, "AlGaN-based laser diodes for the short-wavelength ultraviolet region," *New J. Phys.*, 11, 125013, 2009.

[6] S. Masui, Y. Matsuyama, T. Yanamoto, T. Kozaki, S. I. Nagahama, and T. Mukai, "365 nm Ultraviolet Laser Diodes Composed of Quaternary AlInGan Alloy," *Japanese J. Appl. Physics, Part 2 Lett.*, 42, 11 A, 1318, 2003.

[7] M. Kneissl, D. W. Treat, M. Teepe, N. Miyashita, and N. M. Johnson, "Ultraviolet AlGaN multiple-quantum-well laser diodes," *Appl. Phys. Lett.*, 82, 4441, 2003.

[8] M. Kneissl, Z. Yang, M. Teepe, C. Knollenberg, O. Schmidt, P. Kiesel, N. M.

Johnson, S. Schujman, and L. J. Schowalter., "Ultraviolet semiconductor laser diodes on bulk AlN," *J. Appl. Phys.*, 101, 123103, 2007.

[9] K. Iida, Z. Yang, M. Teepe, C. Knollenberg, O. Schmidt, P. Kiesel, N. M. Johnson, S. Schujman, and L. J. Schowalter., "350.9 nm UV laser diode grown on low-dislocation-density AlGaN," *Japanese J. Appl. Physics, Part 2 Lett.*, 43, 4 A, 499, 2004.

[10] Z. Zhang, M. Kushimoto, T. Sakai, N. Sugiyama, L. J. Schowalter, C. Sasaoka, and H. Amano., "A 271.8 nm deep-ultraviolet laser diode for room temperature operation," *Appl. Phys. Express*, 12, 12, 124003, 2019.

[11] S. Choi, H. J. Kim, Z. Lochner, J. Kim, R. D. Dupuis, A. M. Fischer, R. Juday, Y. Huang, T. Li, J. Y. Huang, F. A. Ponce., "Origins of unintentional incorporation of gallium in AlInN layers during epitaxial growth, part I: Growth of AlInN on AlN and effects of prior coating," *J. Cryst. Growth*, 388, 137, 2014.

[12] S. Iwata, Y. Nanjo, T. Okuno, S. Kurai, and T. Taguchi, "Growth and luminescence properties of subsequently grown AlInN layers on AlN homoepitaxial layers by ammonia gas source molecular beam epitaxy," *Japanese J. Appl. Physics, Part 1 Regul. Pap. Short Notes Rev. Pap.*, 46, 6 A, 3394, 2007.

[13] T. Fujimori, H. Imai, A. Wakahara, H. Okada, A. Yoshida, T. Shibata, and M. Tanaka., "Growth and characterization of AlInN on AlN template," *J. Cryst. Growth*, 272, 381, 2004.

[14] J. Kim, Z. Lochner, M. Ji, S. Choi, H. J. Kim, J. S. Kim, R. D. Dupuis, A. M.

Fischer, R. Juday, Y. Huang, T. Li, J. Y. Huang, F. A. Ponce, and J. H. Ryou., "Origins of unintentional incorporation of gallium in InAlN layers during epitaxial growth, part II: Effects of underlying layers and growth chamber conditions," *J. Cryst. Growth*, 388, 143, 2014.

[15] N. Hatui, M. Frentrup, A. A. Rahman, A. Kadir, S. Subramanian, M. Kneissl, and A. Bhattacharya., "MOVPE growth of semipolar $(11\bar{2}2)$ $Al_{1-x}In_xN$ across the alloy composition range $(0 \leq x \leq 0.55)$," *J. Cryst. Growth*, 411, 106, 2015.

[16] M. M. Satter, H. J. Kim, Z. Lochner, J. H. Ryou, S. C. Shen, R. D. Dupuis, and P. D. Yoder., "Design and analysis of 250-nm AlInN laser diodes on AlN substrates using tapered electron blocking layers," *IEEE J. Quantum Electron.*, 48, 5, 703, 2012.

[17] C. Liu, Y. K. Ooi, and J. Zhang, "Proposal and physics of AlInN-delta-GaN quantum well ultraviolet lasers," *J. Appl. Phys.*, 119, 8, 21–25, 2016.

[18] J. Zhang, H. Zhao, and N. Tansu, "Effect of crystal-field split-off hole and heavy-hole bands crossover on gain characteristics of high Al-content AlGaN quantum well lasers," *Appl. Phys. Lett.*, 97, 111105, 2010.

[19] W. W. Chow and M. Kneissl, "Laser gain properties of AlGaN quantum wells," *J. Appl. Phys.*, 98, 114502, 2005.

CHAPTER 5: Polarization Properties of AlN-Delta-GaN Quantum Well Ultraviolet Light-Emitting Diodes

Previous chapters mention that it is difficult to realize large TE-polarized $\boldsymbol{R_{sp}}$ from conventional AlGaN QWs due to the insufficient C-HH transition, band mixing effect and the QCSE. In chapter 4, we investigate AlGaN-delta-GaN QWs and AlInN-delta-GaN QWs to address this issue. Nonetheless, both structures are extremely difficult to realize experimentally due to the epitaxial growth challenge. An alternative approach would be the use of AlN-delta-GaN QW structure which enables the straightforward epitaxial growth. Recently, several experimental works have been reported on the use of AlN/GaN superlattices [1] and AlN/GaN quantum dots [2]–[6] for DUV emissions. However, the physics and optical properties of these heterostructures are still relatively lacking, which are essential for further improving the device efficiency.

Therefore, this work proposes and investigates the physics and optical properties of AlN-delta-GaN QWs emitting at 234 nm, 246 nm, and 298 nm. The wavelengths were selected to address different issues causing the low TE-polarized emissions: (1) Insufficient C-HH transition or dominant CH subband for short emission wavelength (234 nm); (2) valence subband mixing effect for wavelength near 246 nm; and (3) QCSE for longer emission wavelength (298 nm). The band structures and spontaneous emission properties of the proposed structures are calculated by the self-consistent 6-band $\boldsymbol{k\cdot p}$ model and compared to that of the conventional AlGaN QWs. Several QW structures are also experimentally carried out by the use of plasma-assisted MBE. The light polarization properties from the structures are examined by an in-house polarization-dependent electroluminescence (EL) setup. In addition, a FDTD method was employed to investigate the polarization-dependent light extraction properties and the light radiation patterns from the investigated DUV LED structures to show the importance of the polarization control.

5.1 Physics and Optical Properties from AlN-Delta-GaN QW UV LEDs

5.1.1 Physics of AlN-delta-GaN QWs for deep- and mid-UV emissions

Based on the encouraging optical properties of the AlGaN-delta-GaN QWs and AlInN-delta-GaN QWs from previous chapter in the whole DUV range, we propose a QW structure consisting of a 2-nm AlN and ***d***-Å delta-GaN layer (***d*** = 3 – 11 Å), as shown in figure 5.1 (a). For AlGaN-delta-GaN QW, an ultra-thin GaN layer is inserted at the center of the conventional AlGaN QW, which separates the AlGaN layer into two AlGaN sub-QW regions. Note that the whole AlGaN/GaN/AlGaN structure serves as the QW region in the simulation. However, for AlN-delta-GaN QW, the AlN sub-QW can be regarded as an extremely high Al-content AlGaN sub-QW layer. Therefore, the design of the proposed AlN-delta-GaN QW structure has two advantages: (1) Remain the benefits of the delta-QW design: the insertion of the thin delta-GaN layer could provide a local minimum in the QW region, which enables the electron and hole wavefunctions to locate at the QW center; the thin delta-GaN layer could also rearrange the valence subbands ordering, push the HH back on the top of the valence band with large energy separation to the ground state CH band; (2) The use of AlN sub-QW instead of the AlGaN sub-QW can pursue a much more straightforward epitaxy growth.

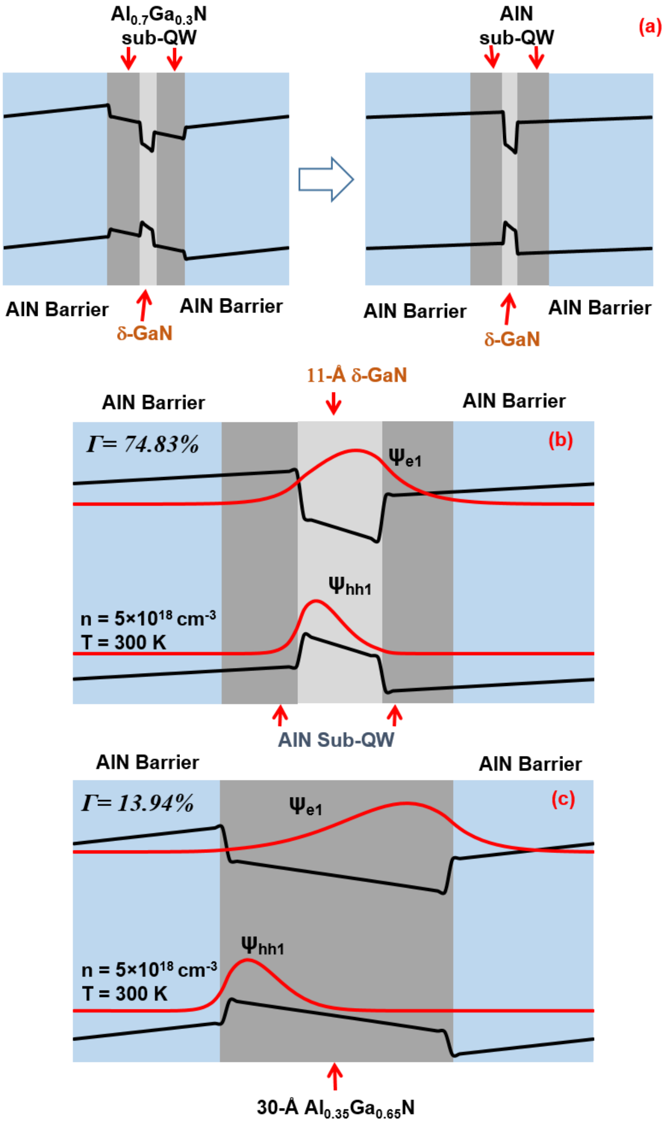

Figure 5.1: *(a) Band structure transitioned from $Al_{0.7}Ga_{0.3}N$-delta-GaN QW to AlN-delta-GaN QW, showing that the use of AlN sub-QW layer is to replace the AlGaN sub-QW region; Energy band lineups for the (b) AlN-delta-GaN QW with delta-GaN thickness of $\boldsymbol{d}$ = 11 Å; (c) 30-Å conventional $Al_{0.35}Ga_{0.65}N$ QW with ground state electron wave function (ψ_{e1}), heavy hole wave function (ψ_{hh1}) and electron and hole wave functions overlap ($\boldsymbol{\Gamma_{e1-hh1}}$). Carrier density is $\boldsymbol{n}$ = 5 × 10^{18} cm^{-3}.*

Figure 5.1 (b) plots the energy band lineups and the ground state wavefunctions of the proposed AlN-delta-GaN QW with $\boldsymbol{d}$ = 11 Å, which are compared to that of the conventional 3-nm $Al_{0.35}Ga_{0.65}N$ QW shown in figure 5.1 (c). The 35% Al-content is selected to achieve a similar emission wavelength with the proposed structure. For the conventional $Al_{0.35}Ga_{0.65}N$ QW, the severe QCSE leads to a large separation of the electron and hole wavefunctions and a small electron-hole wavefunction overlap ($\boldsymbol{\Gamma_{e\_hh}}$) of 13.94%. In contrast, the electron-hole wavefunction overlap is significantly improved to $\boldsymbol{\Gamma_{e\_hh}}$ = 74.83% using the AlN-delta-GaN design, attributed to the better confinement induced by the delta-GaN layer. Consequently, a large spontaneous emission recombination rate can be expected from the AlN-delta-GaN QW.

For shorter emission wavelengths, the delta-QW designs are used not only to improve the electron-hole wavefunction overlap, but more importantly, to modify the valence band structures. Note that to achieve emission wavelengths of 232 nm and 243 nm, 3-nm conventional $Al_xGa_{1-x}N$ QW with Al-content $\boldsymbol{x}$ = 74% and $\boldsymbol{x}$ = 67% must be used, which are, as mentioned previously, very close to valence band crossover Al-content. Consequently, the $Al_{0.67}Ga_{0.33}N$ QW suffers from severe band mixing effect and the carriers equally populate at all the three valence subbands, which result in low TE-polarized $\boldsymbol{R_{sp}}$. However, for the $Al_{0.74}Ga_{0.26}N$ QW, most of the emission photons are TM-polarized due to the dominant C-CH transition. Here we proposed the AlN-delta-GaN QW with $\boldsymbol{d}$ = 3 - 4 Å to address these issues. Figure 5.2 inset (a) plots the band structure from the AlN-delta-GaN QW with $\boldsymbol{d}$ = 3 Å at carrier density of $\boldsymbol{n} = 5\times10^{18}$ cm^{-3}. It's clear that the ground state HH is on the top of valence band with large energy separation to the ground state CH subband, which ensures the dominant C-HH transition and TE-polarized emission. Similar valence band structure can be achieved from the AlN-delta-GaN QW with $\boldsymbol{d}$ = 4 Å. To theoretically confirm the polarization and optical property from the structures, figure 5.2 compares the TE- and TM-polarized spontaneous emission spectra from the AlN-delta-GaN QWs with ***d*** = 3 – 11 Å. By selecting different delta-GaN thicknesses, the emission wavelengths from the AlN-delta-GaN QWs are engineered to ***λ*** = 232 nm, 243 nm and 298 nm. As expected, large TE-polarized while minimum TM-polarized spontaneous emission rates are achieved from all the three QW structures due to the improved electron-hole wave function overlap, as well as the dominant and

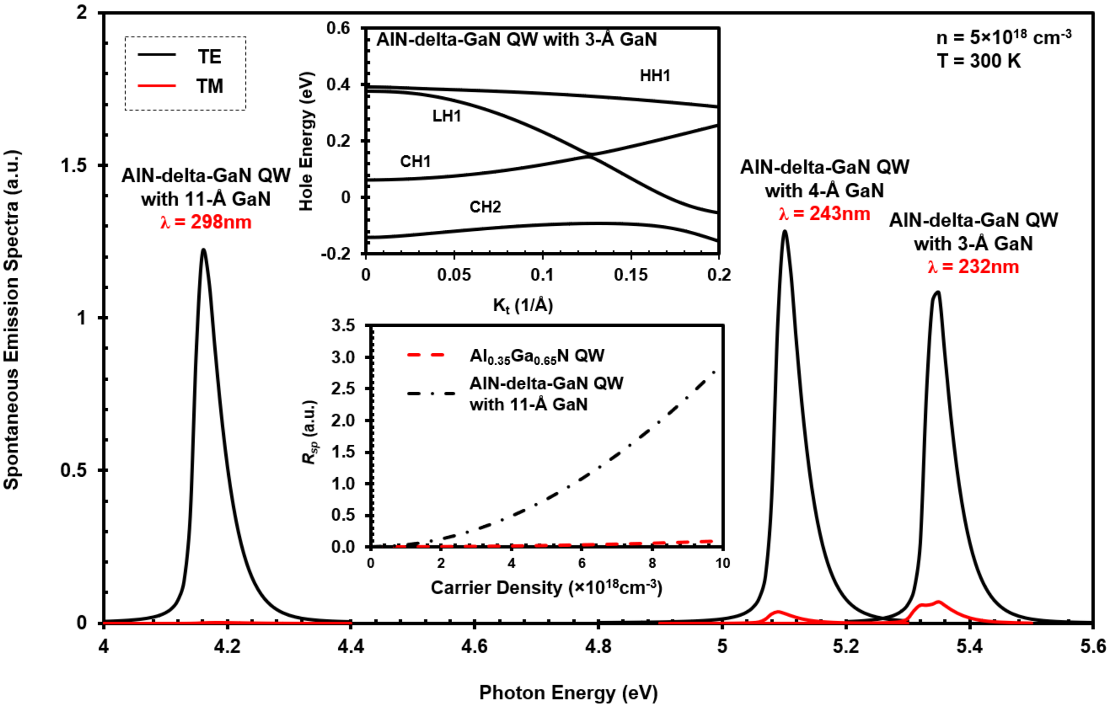

***Figure 5.2**: TE- (black) and TM-polarized (red) Spontaneous emission spectra of AlN-delta-GaN QWs with delta-GaN thickness of **d** = 3 - 11 Å at a carrier density of **n** =5×10^{18} cm^{-3}. Inset (a): Valence band structure from the AlN-delta-GaN QWs with **d** = 3 Å. (b) Total **R_{sp}** as a function of carrier density for AlN-delta-GaN QW with **d** = 11 Å (black) and 3-nm Al$_{0.35}$Ga$_{0.65}$N QW (red).*

To show the enhancement by using the AlN-delta-GaN QW, as compared to the conventional AlGaN QW, figure 5.2 inset (b) plots ***R_{sp}*** as a function of carrier density up to 1 × 10^{19} cm^{-3} for the AlN-delta-GaN QW with ***d*** = 11 Å and the 3-nm Al$_{0.35}$Ga$_{0.65}$N QW. For the conventional Al$_{0.35}$Ga$_{0.65}$N QW, relatively low ***R_{sp}*** was obtained as expected due to the severe QCSE. In contrast, the insertion of the delta-GaN layer in the AlN-delta-GaN QW significantly improves the electron-hole wavefunction overlap which leads to the increase in spontaneous emission rate up to 30 times as compared to that of the conventional $Al_{0.35}Ga_{0.65}N$ QW, demonstrating the use of AlN-delta-GaN QW is promising for the mid-UV regime. Similarly, large $\boldsymbol{R_{sp}}$ enhancements can also be realized by the use of AlN-delta-GaN QW with $\boldsymbol{d}$ = 3 - 4 Å. Specifically, the total $\boldsymbol{R_{sp}}$ from AlN-delta-GaN QW are 7.11 and 1.43 times larger as compared to the conventional AlGaN QW at $\boldsymbol{\lambda}$ = 243 nm and 232 nm, respectively. Note that the relatively low enhancement ratio from the 232 nm QW structure is because of large TM-polarized $\boldsymbol{R_{sp}}$ is generated from the conventional AlGaN QW.

5.1.2 Optical Properties of MBE-grown AlN-delta-GaN QW UV LEDs

Considering the large enhancement in TE-polarized $\boldsymbol{R_{sp}}$ predicted by the calculation and the consequent potential in improving UV LED IQE, several AlN-delta-GaN QW UV LEDs are grown and fabricated in this study [2]–[6]. Specifically, the LED heterostructures were grown on AlN/sapphire templates with a dislocation density of 1×10^{10} cm^{-2} by GENxplor plasma-assisted MBE. Figure 5.3 (a) shows the schematic of the MBE-grown AlN-delta-GaN QW LED targeting at $\boldsymbol{\lambda}$ = 298 nm. Specifically, the active region consists of 8-period 2.5-nm AlN/GaN QW and sandwiched by a 100-nm Mg-doped $Al_{0.5}Ga_{0.5}N$ and 200-nm Si-doped $Al_{0.77}Ga_{0.23}N$ cladding layers. More epitaxy growth and device fabrication details can be found in ***ref***. [2], [3]. The ultra-thin GaN layer is controlled to be 3-4 monolayer (ML) and confirmed by a cross-sectional TEM image shown in figure 5.3 (a).

Room temperature EL measurements were performed on a 300 µm × 300 µm top-emitting device at different current densities (***j*** = 2-23 A/cm^2), showing the peak emission wavelength at 298 nm which is similar with the simulation results, as presented in figure 5.3 (b). Note that there is another peak around 308 nm due to the delta-GaN layer thickness fluctuation within the range of 3-4 ML.

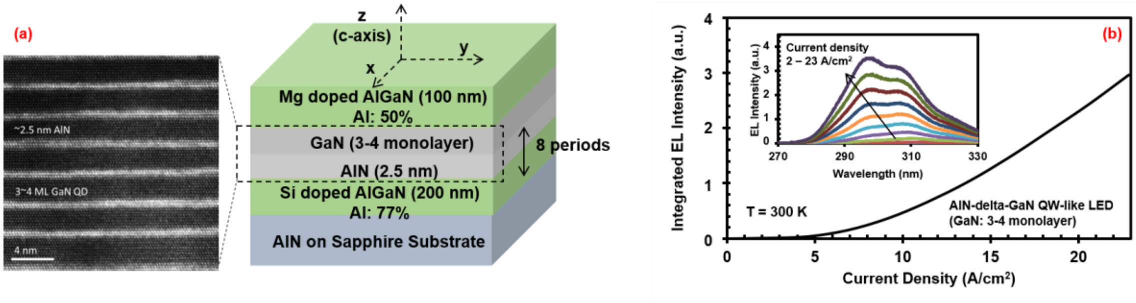

***Figure 5.3**: (a) Schematic of MBE-grown AlN-delta-GaN QW UV-LED heterostructure and cross-sectional TEM image of the active region. The thickness of the delta-GaN region is 3-4 monolayer (ML). (b) Integrated EL intensity as a function of current density. Inset: EL spectra from the AlN/GaN QW-like LED with different current densities (**j** = 2 – 23 A/cm^2).*

Figure 5.4 shows the schematic of the MBE-grown AlN-delta-GaN QW UV LEDs emitting at shorter emission wavelengths. Specifically, the active regions include 20-period AlN/GaN QWs with the AlN/GaN thicknesses of 2-nm/1-2ML and 1.75-nm/2-3ML to realize 234 nm and 246 nm emissions, respectively, as evidenced by cross-sectional TEM images shown in figure 5.4.

To optimize the carrier injections, polarization-induced doping technique was used in n- and p-typed carrier injection layers [3], [6]. After the heterostructure growth, the samples were fabricated to 300 µm × 300 µm top-emitting devices. Room-temperature EL measurements with current density of ***j*** = 16.67 A/cm^2 were performed on those UV LEDs, showing 234-nm emission with the full width at half maximum (FWHM) of 10.24

nm from the 1-2 ML GaN QW and 246-nm emission with the FWHM of 11.5 nm from the 2-3 ML QW, which are consistent with the calculation results. Note that there is a side peak at 280 nm from both LED structures, which is attributed to the 50% Al-content AlGaN in the buffer layer. The output powers of both LEDs were measured without using an integrating sphere. As shown in figure 5.4 inset, the output power were measured as 0.4 mW/cm^2 for 234 nm LED and 12 mW/cm^2 for 246 nm LED at $\boldsymbol{j}$ = 40 A/cm^2, respectively.

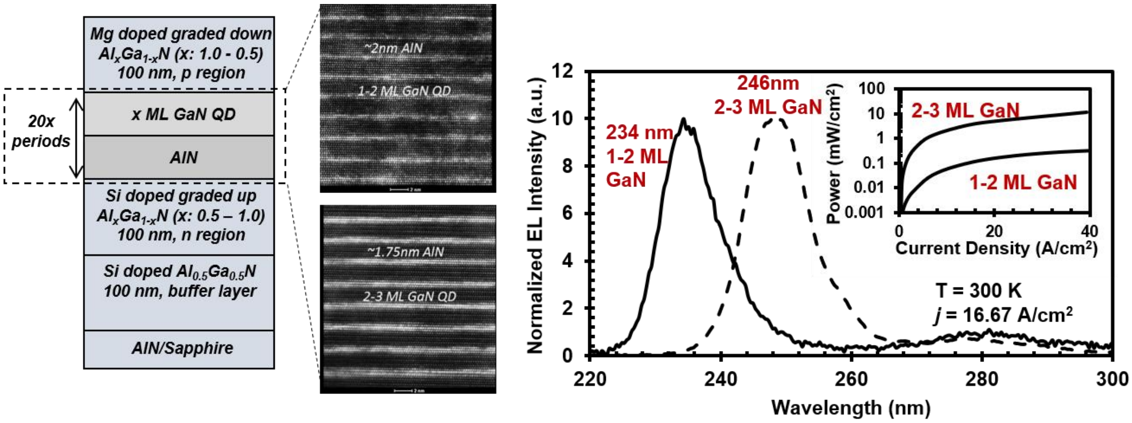

***Figure* 5.4**: *Schematic of the MBE-grown AlN-delta-GaN QW LEDs and cross-sectional TEM images of the active regions. Normalized EL spectra from AlN-delta-GaN QW LEDs with current density of* $\boldsymbol{j}$*=16.67 A/cm*^{2}*. (Inset) Output power as a function of current density up to* $\boldsymbol{j}$ *= 40 A/cm*^{2} *from AlN-delta-GaN QW LEDs. The TEM images are taken from figure.2d and 2e of reference [6].*

5.2 Polarization Properties from AlN-Delta-GaN QW UV LEDs

5.2.1 Optical polarization measurements setup

To study the light polarization properties from the UV LED structures, we built a polarization-dependent EL setup. A schematic illustration of the setup is shown in figure 5.5. Specifically, the LED sample is placed on a stationary stage while a Glan-Taylor polarizer and an optical fiber are fixed on a rotatable holder which can be rotated about the x-axis with angle $\boldsymbol{\theta}$ representing the angle between the c-axis and the collecting fiber. The polarizer can also be rotated about the light emitting direction to resolve the $\boldsymbol{E}_{\parallel}$ (electric field in $\boldsymbol{y}$-$\boldsymbol{z}$ plane) and $\boldsymbol{E}_{\perp}$ (electric field along the x-axis), corresponding to the intensities $\boldsymbol{I}_{\parallel}$ and $\boldsymbol{I}_{\perp}$. Note that the two intensities are not sole TE and TM components, which have the expressions as:

$$I_{\parallel} = I_{TEy} cos^2\theta + I_{TM} sin^2\theta$$

$$I_{\perp} = I_{TEx} \tag{5-1}$$

where I_{TM} is the intensity of TM-polarized emission. $\boldsymbol{I_{TEx}}$ and $\boldsymbol{I_{TEy}}$ represent the intensities of TE-polarized emissions along $\boldsymbol{x}$ and $\boldsymbol{y}$ directions. Ideally, there is no anisotropic emission in the $\boldsymbol{x}$-$\boldsymbol{y}$ plane, $\boldsymbol{I_{TEx}}$ and $\boldsymbol{I_{TEy}}$ are identical. Therefore, the total $\boldsymbol{I_{TE}}$ and $\boldsymbol{I_{TM}}$ can be given as:

$$I_{TE}(Total) = I_{TEx} + I_{TEy} cos^2\theta = I_{\perp} \ \ (1 + cos^2\theta)$$

$$I_{TM}(Total) = I_{TM} sin^2\theta = I_{\parallel} - I_{\perp} cos^2\theta \tag{5-2}$$

Note that at $\boldsymbol{\theta} = 90°$, the measured intensities $\boldsymbol{I}_{\parallel}$ and $\boldsymbol{I}_{\perp}$ are directly identified as TM- and TE-polarized components and hence several groups fabricate edge-emitted devices to study the polarization properties [7]–[9]. Unlike other polarization measurement setups, we add a rotatable stage for the polarizer and the collecting fiber, which enables us to achieve polarization-dependent light radiation patterns.

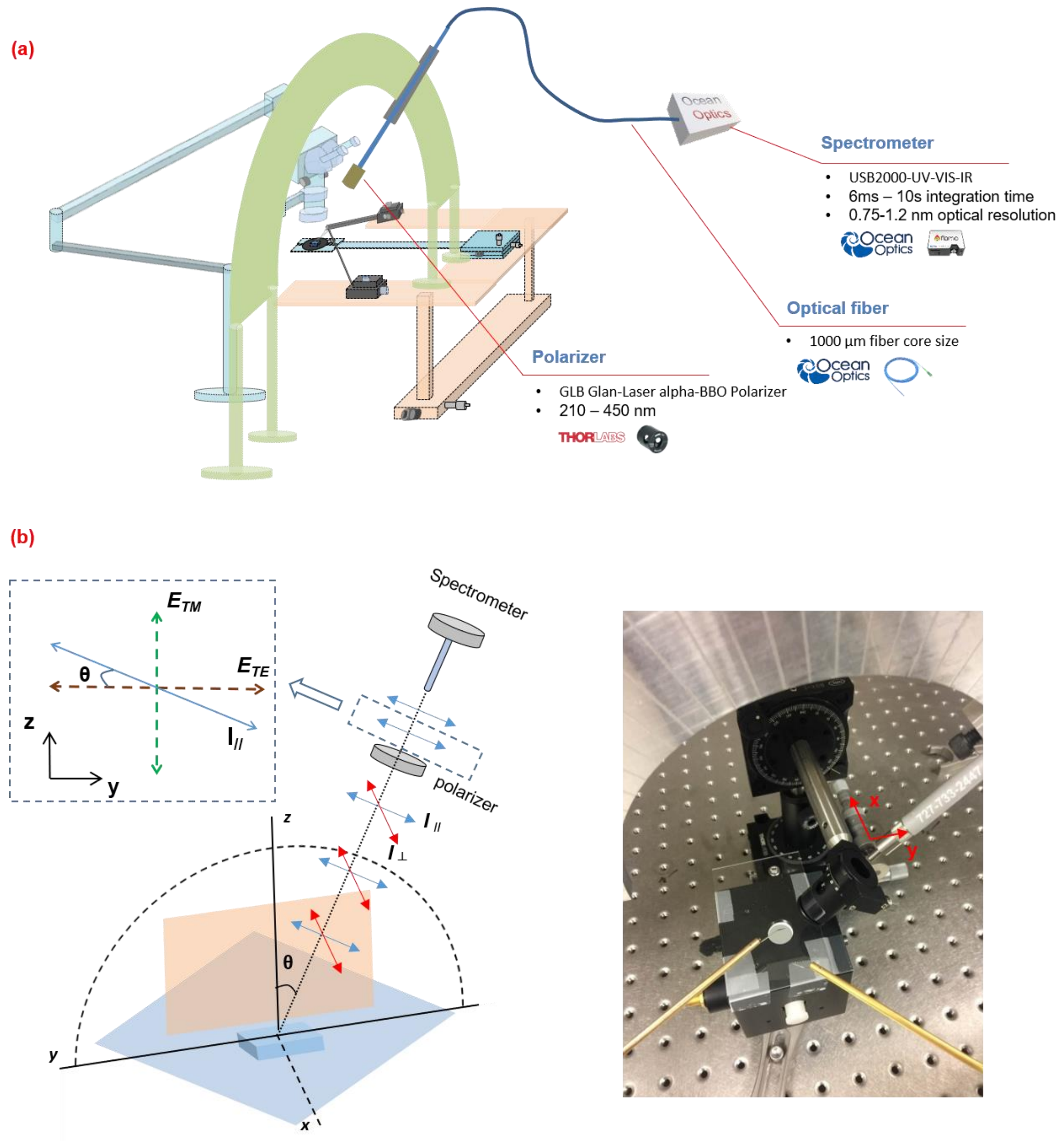

__Figure 5.5__: (a) Schematic of the polarization-dependent EL measurements setup. (b) Schematic illustration of the polarization-dependent measurements

5.2.2 Optical polarization from AlN-delta-GaN QW UV LEDs

The polarization characteristics of the AlN-delta-GaN QW UV LEDs were investigated in this study by using the polarization-dependent EL setup under pulsed current injections with the frequency of 10 kHz and duty cycle of 5%. The current density is fixed at $\boldsymbol{j}$ = 40 A/cm^2. Two angles $\boldsymbol{\theta} = 30°$ and $\boldsymbol{\theta} = 45°$ are selected in this study because the radiation pattern is Lambertian-like with a large intensity observed at small angles ($\boldsymbol{\theta} < 30°$) for TE-polarization while the pattern has a ribbon-shape with peak intensity at a larger angle of ($\boldsymbol{\theta} \sim 50°$) for TM-polarization. As shown in figure 5.6, $\boldsymbol{I_\perp/I_\parallel}$ ratios were measured as 1.157 and 1.149 at $\boldsymbol{\theta} = 30°$ and $\boldsymbol{\theta} = 45°$for 298-nm AlN-delta-GaN UV LEDs, respectively, corresponding to the $\boldsymbol{I_{TE}/I_{TM}}$ ratios of 15.3 for $\boldsymbol{\theta} = 30°$ and 4.05 for $\boldsymbol{\theta} = 45°$. Strong TE-polarized emissions are observed at both angles with the degree of polarization of 0.87 for $\boldsymbol{\theta} = 30°$ and 0.60 for $\boldsymbol{\theta} = 45°$. The dominant TE-polarized emission can be attributed to the prevailing C-HH transition and the improved electron-hole wavefunction overlap.

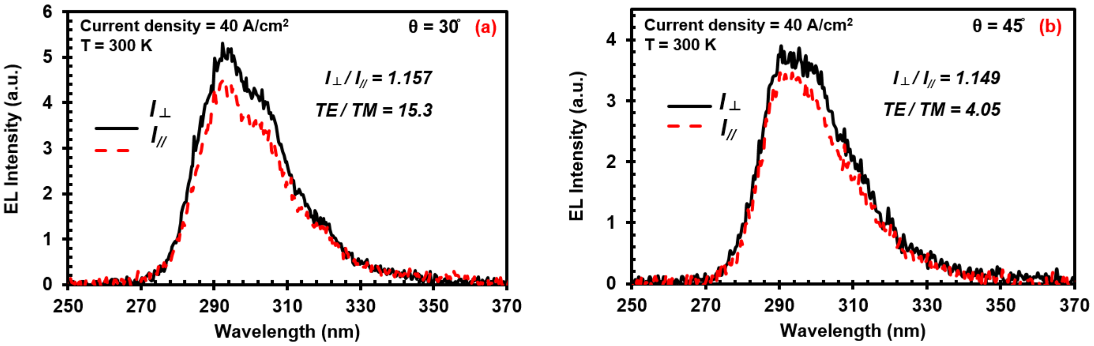

Figure 5.6: *Polarization-dependent EL spectra from the 298-nm AlN-delta-GaN QW UV LED at (a) $\boldsymbol{\theta}$ = 30˚and (b) $\boldsymbol{\theta}$ = 45˚ with current density of 40 A/cm^2.*

Similarly, the polarization properties from 234-nm and 246-nm AlN-delta-GaN QW UV LEDs were measured. The polarization-dependent EL measurements results are presented in figure 5.7, showing the dominant TE-polarized emissions from both UV LEDs at two angles $\boldsymbol{\theta} = 30°$ and $\boldsymbol{\theta} = 45°$. Specifically, for 234-nm LED, $\boldsymbol{I_\perp/I_\parallel}$ ratios were measured as 1.23 at $\boldsymbol{\theta} = 30°$ and 1.48 at $\boldsymbol{\theta} = 45°$, which result in $\boldsymbol{I_{TE}}/\boldsymbol{I_{TM}}$ ratios of 27.77 and 8.55, respectively. The corresponding degrees of polarization are extracted as 0.93 and 0.79. For 246-nm LED, $\boldsymbol{I_{TE}}/\boldsymbol{I_{TM}}$ ratios are calculated as 17.731 and 5.45 and the degrees of polarization are calculated as 0.89 and 5.45 at $\boldsymbol{\theta} = 30°$ and $\boldsymbol{\theta} = 45°$, respectively, which experimentally confirms the TE-dominant emission from the devices, attributed to the topmost HH subband and delta-GaN layer-induced large energy separation between HH and CH subbands. The agreement from the measured and simulated results indicates the proposed AlN-delta-GaN QWs enable to mitigate the band mixing effect and are proven as promising candidates to realize high-efficiency DUV LEDs.

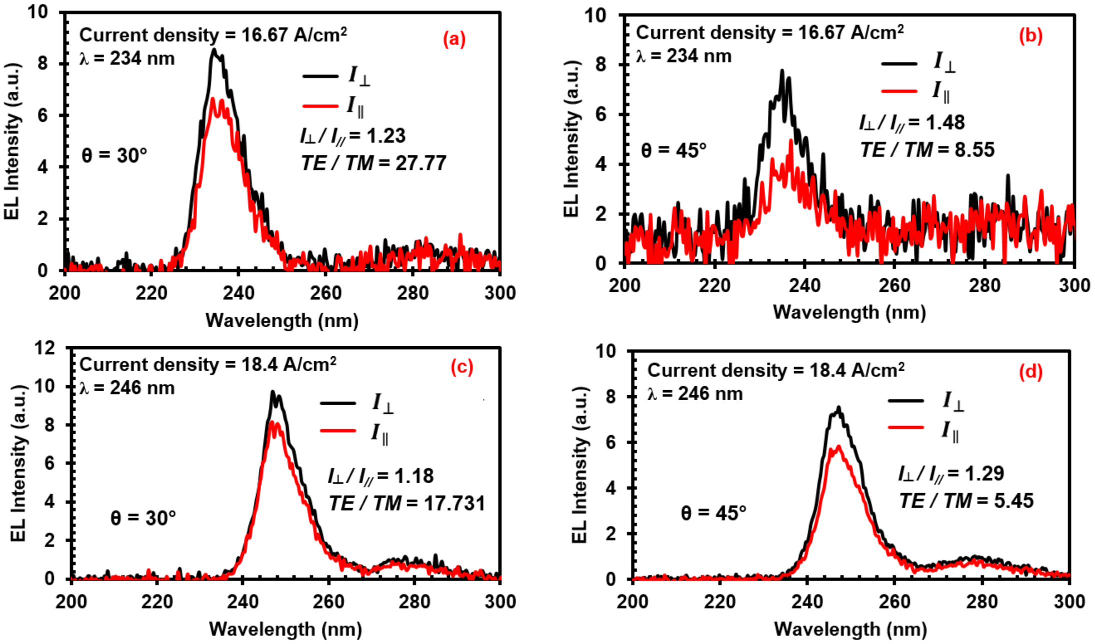

***Figure 5.7**: Polarization-dependent EL spectra from the (a)-(b) 234-nm and (c)-(d) 246-nm AlN-delta-GaN QW UV LEDs at θ=30° and θ=45°.*

Furthermore, it is important to understand the advantages of the dominant TE-polarized emission from UV LEDs with short emission wavelengths. Here we studied emission profiles with a three-dimensional (3D) FDTD simulation software (RSOFT). Details of the FDTD simulations and parameters can be found in *Ref.* [10]–[12]. In short, a single dipole source was placed at the center of the active region with the TE- and TM-polarization defined as electric fields travel in-plane ($\boldsymbol{E} \perp \boldsymbol{c}$) and out-of-plane ($\boldsymbol{E} \parallel \boldsymbol{c}$). A field monitor was positioned at 200 nm away from the top surface of the device to track the light radiation patterns. The polarization-dependent light radiation patterns from 234-nm and 246-nm AlN-delta-GaN QW LEDs are plotted in figure 5.8. Both structures exhibit significantly stronger TE-polarized emissions with Lambertian-like shapes, as compared to the TM-polarized emissions with ribbon-like shapes, which have peak intensity at $\boldsymbol{\theta} \sim 50°$. For the 234-nm LED, the TE-polarized pattern has a more pointed-tip observed at $\boldsymbol{\theta} = 0°$, indicating the majority of photons are traveling at small angles. In addition, the light extraction efficiencies ($\boldsymbol{\psi_{ext}}$) were also estimated from the simulations by calculating the ratio of the light output power measured from the top of the device to the dipole power in the active region, showing the higher efficiency for TE-polarized photons ($\boldsymbol{\psi_{ext}}$ ~ 5%) as compared to that for TM-polarized photons ($\boldsymbol{\psi_{ext}}$ ~ 0.5%).

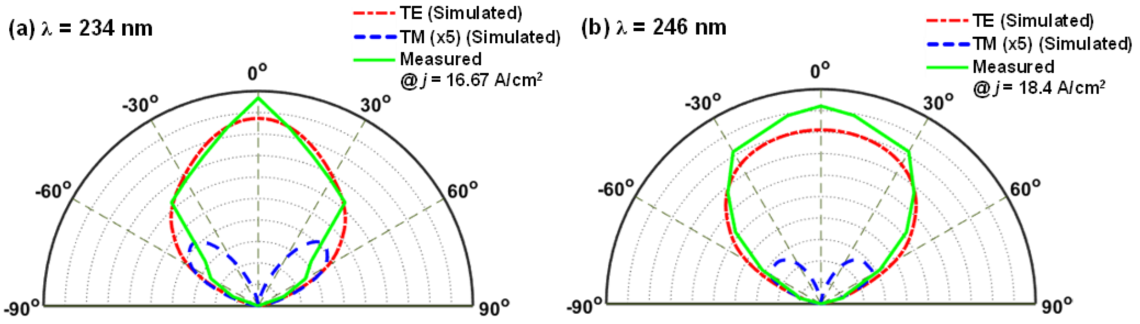

Figure 5.8*: FDTD simulated and measured light radiation patterns of the (a) 234 nm, and (b) 246 nm AlN-delta-GaN UV LEDs.*

To compare with the FDTD simulation results, unpolarized light radiation patterns from both 234-nm and 246-nm AlN-delta-GaN QW LEDs were experimentally extracted out based on angle-dependent EL measurements. The results are plotted in figure 5.8 and compared to the calculated patterns. The measured light radiation patterns from both LEDs show the highest intensity at $\theta = 0°$ and the intensities drop with collecting angle increases. As shown in figure 5.8, the measured patterns show great consistency with the calculated TE-polarized radiation pattern, indicating the dominant TE-polarized emission from the proposed AlN-delta-GaN UV LEDs. Therefore, the use of the AlN-delta-GaN QWs ensures the dominant easy-escaped TE-polarized emission, together with the improved $\boldsymbol{R_{sp}}$ value, will lead to larger total efficiencies as compared to the conventional AlGaN QWs below 250 nm

5.3 Summary

In summary, the physics and polarization properties of the AlN-delta-GaN QW emitted at 234 nm, 246 nm and 298 nm are investigated in this study. The insertion of the ultra-thin delta-GaN layer could significantly improve the electron-hole wave function overlap. For example, as high as 74.83% of electron-hole wave function overlap were achieved by using the AlN-delta-GaN QW with delta-GaN thickness of $\boldsymbol{d}$ = 11 Å, (13.94% for the conventional AlGaN QW), which leads to a 30 times enhancement in the spontaneous emission recombination rate. In addition, the use of AlN-delta-GaN QW largely separates the HH and CH subbands and ensures the dominant C-HH transition, which results in large TE-polarized $\boldsymbol{R_{sp}}$ at short emission wavelength ($\boldsymbol{\lambda} < 250$ nm).

To experimentally verify the optical properties from the AlN-delta-GaN QW, we grew several AlN-delta-GaN QW UV LEDs by using MBE system. The heterostructures were fabricated into top-emitting devices. By selecting the delta-GaN thicknesses, 234 nm, 246 nm and 298 nm UV LEDs were carried out. In this work, we also developed a polarization-dependent EL measurements setup to study the polarization properties from the AlN-delta-GaN QW UV LEDs. The measurements were performed at two different angles $\boldsymbol{\theta} = 30°$ and $\boldsymbol{\theta} = 45°$. Dominant TE-polarized emissions were observed from all the AlN-delta-GaN UV LEDs.

In addition, we also used FDTD simulations to study the light radiation profile from the 234-nm and 246-nm AlN-delta-GaN UV LEDs and compared the results to the experimental data collected by the angle-dependent EL measurements setup. From the results, the TE-polarized light radiation patterns from FDTD simulations are consistent with the measured unpolarized results, indicating the dominant TE-polarized emissions from both AlN-delta-GaN QW structures. Meanwhile, the light extraction efficiencies for TE-polarized photons are much larger than that for TM-polarization, showing the importance of the polarization control in the LED efficiency. Therefore, the theoretical prediction, combining with experimental observations, demonstrates the use of AlN-delta-GaN QWs holds high promise for high-efficiency mid- and DUV LEDs applications.

Reference for Chapter 5:

[1] Y. Taniyasu and M. Kasu, “Polarization property of deep-ultraviolet light emission from C-plane AlN/GaN short-period superlattices,” *Appl. Phys. Lett.*, 99, 251112, 2011.

[2] J. Verma, P. K. Kandaswamy, V. Protasenko, A. Verma, H. Grace Xing, and D. Jena, “Tunnel-injection GaN quantum dot ultraviolet light-emitting diodes,” *Appl. Phys. Lett.*, 102, 041103, 2013.

[3] J. Verma, S. M. Islam, V. Protasenko, P. Kumar Kandaswamy, H. Xing, and D. Jena, “Tunnel-injection quantum dot deep-ultraviolet light-emitting diodes with polarization-induced doping in III-nitride heterostructures,” *Appl. Phys. Lett.*, 104, 021105, 2014.

[4] B. Daudin *et al.*, “Sub-230 nm deep-UV emission from GaN quantum disks in AlN grown by a modified Stranski – Krastanov mode diodes Sub-230 nm deep-UV emission from GaN quantum disks in AlN grown by a modified Stranski – Krastanov mode,” *Jpn. J. Appl. Phys.*, 55, 05FF06, 2016.

[5] S. M. Islam *et al.*, “Deep-UV emission at 219 nm from ultrathin MBE GaN/AlN quantum heterostructures,” *Appl. Phys. Lett.*, 111, 091104, 2017.

[6] S. M. Islam *et al.*, “MBE-grown 232-270 nm deep-UV LEDs using monolayer thin binary GaN/AlN quantum heterostructures,” *Appl. Phys. Lett.*, 110, 041108, 2017.

[7] M. Kneissl and J. Rass, *III-Nitride Ultraviolet Emitters*, 227. Springer International

Publishing Cham, 2016.

[8] X. Chen, C. Ji, Y. Xiang, X. Kang, B. Shen, and T. Yu, “Angular distribution of polarized light and its effect on light extraction efficiency in AlGaN deep-ultraviolet light-emitting diodes,” *Opt. Express*, 24, 10, A935, 2016.

[9] J. Shakya, K. Knabe, K. H. Kim, J. Li, J. Y. Lin, and H. X. Jiang, “Polarization of III-nitride blue and ultraviolet light-emitting diodes,” *Appl. Phys. Lett.*, 86, 091107, 2005.

[10] C. H. Yan, H. Yao, J. M. Van Hove, A. M. Wowchak, P. P. Chow, and J. M. Zavada, “Ordinary optical dielectric functions of anisotropic hexagonal GaN film determined by variable angle spectroscopic ellipsometry,” *J. Appl. Phys.*, 88, 3463, 2000.

[11] Y. K. Ooi, C. Liu, and J. Zhang, “Analysis of Polarization-Dependent Light Extraction and Effect of Passivation Layer for 230-nm AlGaN Nanowire Light-Emitting Diodes,” *IEEE Photonics J.*, 9, 4, 2017.

[12] Y. K. Ooi and J. Zhang, “Light Extraction Efficiency Analysis of Flip-Chip Ultraviolet Light-Emitting Diodes With Patterned Sapphire Substrate,” *IEEE Photonics J.*, 10, 4, 2018.

CHAPTER 6: MBE Growth of AlGaN-Delta-GaN Quantum Wells

Deep-ultraviolet (DUV) light-emitting diodes (LEDs) could potentially replace conventional low- and medium-pressure mercury lamps for applications such as water purification/disinfection, sterilization, and free-space communications because of their compact size, long lifetimes, and short turn-on/off time [1]–[4]. Photons of energy 4.43 - 4.77 eV (~ 260 nm – 280 nm) are found to be the most effective for disinfection at which the maximum absorption through DNA from bacteria is typically realized [1]–[6] . AlGaN ternary alloys are well suited for interband optical transitions at such high energies. However, increasing the emission efficiencies of AlGaN-based active regions will accelerate its adaption and usage [1]. Although Takayoshi Takano *et. al.*, reported a record 20% external quantum efficiency (EQE) at 275 nm in 2017 [7], most practical DUV LEDs are limited below 10% EQE, and the efficiency drops as the emission wavelength decreases [1]–[4]. One of the reasons is the low internal quantum efficiency (IQE) from the AlGaN QW active regions [1]. Most 260 nm – 280 nm UV LEDs use AlN/sapphire templates, which have a large threading dislocation density (TDD) of ~10^{10} cm^{-2} due to the lattice mismatch between AlN and sapphire. Previous research demonstrated that the IQE of AlGaN DUV LED can be boosted from 1% to 60% by reducing the TDD from 10^{10} cm^{-2} down to 5×10^{8} cm^{-2} due to the significantly reduced non-radiative recombination rate [1]. However, such high quality AlN/sapphire templates or AlN substrates currently prohibitive in mass production. A complementary way to improve the IQE is to engineer the radiative recombination rate in the quantum well (QW) active region. For DUV LEDs emitting at 260 nm – 280 nm, AlGaN alloy quantum wells suffer from severe quantum confined stark effect (QCSE) caused by the large internal polarization field. Therefore, alternate QW heterostructures that obtain a larger electron and hole wave function overlap could potentially deliver a much higher radiative recombination rate and IQE.

In previous chapter, we have proposed an AlGaN-delta-GaN QW as a possible solution to improve the electron and hole wave function overlap for DUV emission [8]–[10]. Specifically, an ultra-thin GaN layer (several Å) is inserted in the center of a conventional QW to form the delta-QW structure. Our theoretical study predicted that the insertion of this thin layer could push the ground state electron and hole wave functions toward the QW center, enhancing their overlap integral. As a result, the spontaneous emission rate per unit volume ($\boldsymbol{R_{sp}}$) from the AlGaN-delta-GaN QW is significantly enhanced, as compared to the conventional AlGaN QW at similar emission wavelength. This prediction has not been experimentally tested due to challenges in epitaxy. Recently, we experimentally demonstrated AlN-delta-GaN QW UV LEDs with a few Å delta-GaN layer thickness emitting at 234 nm, 246 nm and 298 nm by using molecular beam epitaxy (MBE) [11], [12]. In this work, we report the successful epitaxial growth of the AlN-delta-GaN QW structure and observe a very high IQE as predicted by theory. The same growth techniques to achieve monolayer and uniform thickness control were also developed in our lab for GaN resonant tunneling diodes (RTDs) [13]; record-performing RTDs have been demonstrated with device peak densities up to 220 kA/cm^2 [13].

6.1 Concept and Physics of 260-nm AlGaN-delta-GaN Quantum Well

In this work, we designed and grew an $Al_{0.9}Ga_{0.1}N$-delta-GaN QW structure with 5-Å (2 monolayer) delta-GaN layer thickness to target at 260 nm emission. The band structure and optical properties from this structure were investigated by a self-consistent 6-band ***k·p*** model as introduced in appendix B. The barrier thickness is set to be 3 nm on each side of the QWs while the carrier density is kept at n = 5×10^{18} cm^{-3}. The structural and optical properties of the $Al_{0.9}Ga_{0.1}N$-delta-GaN QW with 5-Å delta-GaN thickness were calculated by using a self-consistent 6-band ***k·p*** model and compared to that of a conventional 3-nm AlGaN QW with similar emission wavelength. The barrier thickness is set to be 3 nm on each side of the QWs while the carrier density is kept at n = 5×10^{18} cm^{-3}. Figure 6.1 plots the band lineups and wave functions from $Al_{0.9}Ga_{0.1}N$-delta-GaN QW and $Al_{0.58}Ga_{0.42}N$ QW. It is clear that the electron and hole wave functions are pushed toward to the QW center for the $Al_{0.9}Ga_{0.1}N$-delta-GaN QW structure due to the insertion of the ultra-thin delta-GaN layer, while large separation of the electron and hole wave functions was observed for conventional $Al_{0.58}Ga_{0.42}N$ QW because of the large polarization electric field. As a result, the large enhancement in the electron-hole wave function overlap ($\boldsymbol{\Gamma_{e\text{-}hh}}$ = 82.58% vs. 15.5%) leads to a significant boost in the spontaneous emission rate with peak emission wavelength of $\lambda \sim 258$ nm, as shown in figure 6.1. Specifically, the spontaneous emission rate per unit volume ($\boldsymbol{R_{sp}}$) of the $Al_{0.9}Ga_{0.1}N$-delta-GaN QW was calculated as 1.82×10^{26} $s^{-1}cm^{-3}$, which corresponds to IQE =78.44% by using ABC-model with SRH coefficient ($\boldsymbol{A}$) of $\boldsymbol{A} = 1\times10^{7}$ s^{-1} and Auger coefficient ($\boldsymbol{C}$) of $\boldsymbol{C} = 1\times10^{-33}$ cm^{6}/s [14]. On the contrary, only 12.66% of IQE was expected from the conventional $Al_{0.58}Ga_{0.42}N$ QW under the same condition.

In addition, previous study mentioned the flexibility of the delta-QW design for deep-UV LEDs by adjusting the delta-GaN QW thickness and the Al-composition in AlGaN sub-QW region. Therefore, this work also calculates another AlGaN-delta-GaN QW structure with 3-Å delta-GaN layer for 260 nm emission and is compared with conventional AlGaN QWs with different QW thickness at similar emission wavelength. The results show much larger $\boldsymbol{R_{sp}}$ from both delta-QW designs, as compared to conventional AlGaN QWs even with the QW thickness down to 2 nm, which indicates the delta-QW is a promising alternative active region for high-efficiency UV LEDs at 260 nm.

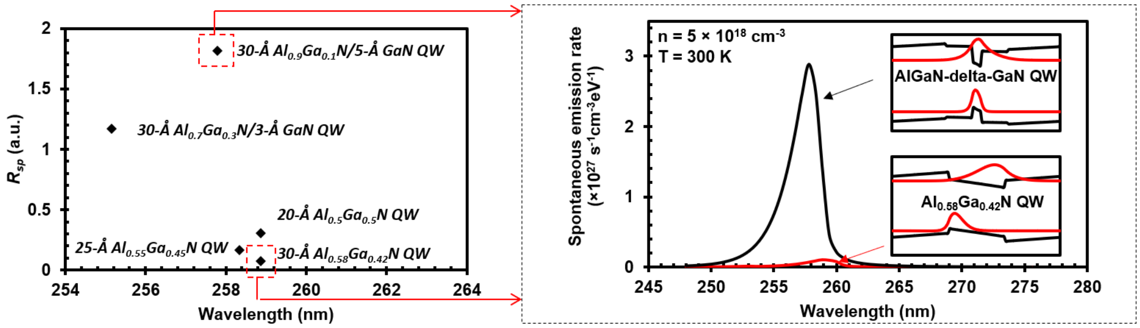

***Figure 6.1**: Spontaneous emission recombination rate per unit volume ($\boldsymbol{R_{sp}}$) for 30-Å $Al_{0.9}Ga_{0.1}N$/5-Å GaN QW, 30-Å $Al_{0.7}Ga_{0.3}N$/3-Å GaN QW, and AlGaN QWs with QW thickness of 2 nm, 2.5 nm and 3 nm at room temperature. The carrier density is $n = 5\times10^{18}$ cm^{-3}; Spontaneous emission spectra, band lineups and wave functions from $Al_{0.9}Ga_{0.1}N$-delta-GaN QW and 3-nm $Al_{0.58}Ga_{0.42}N$ QW.*

6.2 MBE-grown 260-nm AlGaN-delta-GaN Quantum Well

To experimentally study the AlGaN-delta-GaN QW, we used a Veeco Gen-10 plasma assisted MBE system to epitaxially grew the heterostructure. In this work, a 5-period $Al_{0.9}Ga_{0.1}N$-delta-GaN QW was grown on the AlN/sapphire template with threading dislocation density of 10^{10} cm^{-2}. The samples were diced into 1 cm × 1cm and cleaned by acetone, methanol, and isopropanol in an ultrasonic bath to remove the contaminations from the surface. The cleaned substrate is then indium-mounted on a 3-inch Si wafer and loaded into the system. The substrate is first baked at 200℃ for at least 5 hours in the load lock chamber and follow by a 500℃ bake for 2 hours in the buffer chamber. The substrate after the 2-step bake is ready for epitaxy growth. The samples were then transferred into the growth chamber consisting 1 standard Al and two standard Ga effusion cells. A N_2 plasma power of 200 W with 1.65 sccm gas flow was used for all the growths which corresponds to an effective nitrogen beam equivalent pressure (BEP) of 4.5×10^{-7} Torr and a growth rate of ~300 nm/h. The chamber pressure and substrate temperature were maintained at ~1.83×10^{-5} Torr and 800°C throughout the growths.

Figure 6.2 schematically plots the epitaxial layer structure and growth flow diagram. A 100-nm AlN buffer layer was first grown on the template prior to the QW epitaxy. The MQW region consists of 5 periods of $Al_{0.9}Ga_{0.1}N$-delta-GaN/AlN structure. Each layer has a 2-ML GaN layer sandwiched by two 1.5-nm $Al_{0.9}Ga_{0.1}N$ sub-QW layers and followed by a 3-nm AlN barrier. Since the thickness and the quality of the ultra-thin delta-GaN layer strongly determines device emission wavelength and overall efficiency, precise control on the 2-ML GaN growth is critical to the $Al_{0.9}Ga_{0.1}N$-delta-GaN epitaxy. In this work, each cycle loop started with the ultra-thin GaN growth and followed by the 1.5-nm $Al_{0.9}Ga_{0.1}N$ layer. Note that two different Ga effusion cells were used for these two layers to have different Ga fluxes. For the AlN layer, we used migration-enhanced epitaxy (MEE) technique to counter the low Al adatom mobility and smoothen the surface. Specifically, instead of opening both Al and N_2 shutters at the same time, we deposited the Al first and then consumed it by opening the N_2 shutter. An interruption

(No shutter open) was added in the middle of the process to desorb excess Ga adatoms left from the AlGaN growth. After the second $Al_{0.9}Ga_{0.1}N$ sub-QW layer formation, there is another interruption added to desorb the excess Ga. The RF plasma power was turned off during this interruption as well to prevent unintentional GaN formation. Throughout the growth, the sample was monitored in-situ by reflection high-energy electron diffraction (RHEED), as shown in figure 6.2, presenting a long streaky pattern, which indicates a very smooth morphology during the epitaxy.

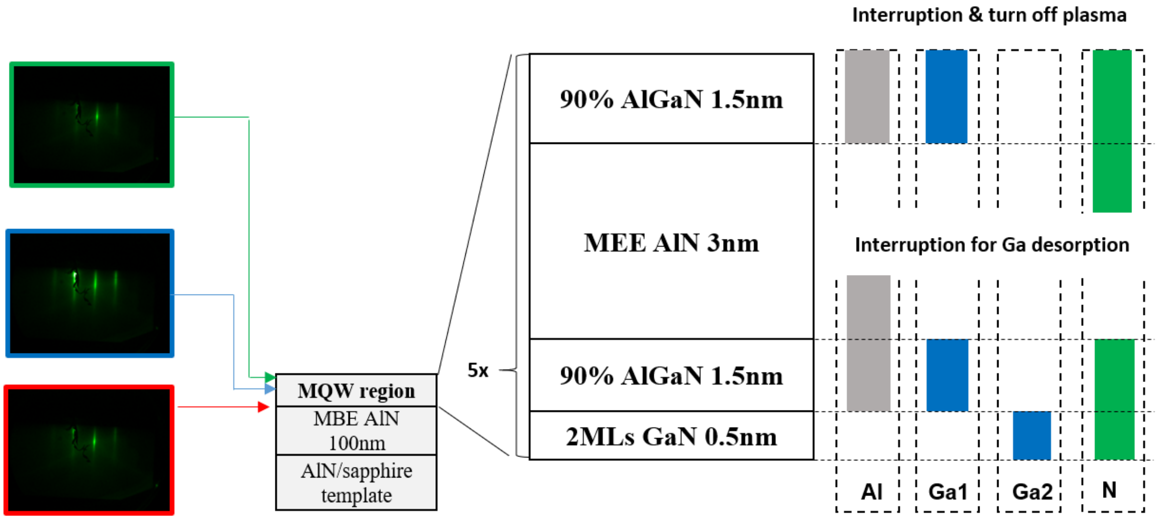

***Figure 6.2**: Schematic of the structure with 5 periods of $Al_{0.9}Ga_{0.1}N$-delta-GaN QWs, RHEED patterns before, during and after the active region growth; flux control during the active region growth*

6.3 Characterizations of MBE-grown 260-nm AlGaN-delta-GaN Quantum Well

6.3.1 Structural properties from the MBE-grown AlGaN-delta-GaN QW

To verify the morphology of the MBE-grown sample, an atomic force microscope (AFM) image was taken after the active region growth, as shown in figure 6.3 (a) inset, showing the sample surface is smooth after the whole epitaxy process. To confirm the 2-ML GaN incorporation, X-ray diffraction (XRD) 2θ-ω scan was performed on the epitaxial $Al_{0.9}Ga_{0.1}N$-delta-GaN QW sample and compared to that of an $Al_{0.9}Ga_{0.1}N$ QW grown under the same growth condition. $Al_{0.9}Ga_{0.1}N$ QW show a shoulder peak next to the strong AlN substrate peak, which corresponds to the 90% AlGaN layer. For $Al_{0.9}Ga_{0.1}N$-delta-GaN QW, the XRD pattern is fitted well with a 5-period 2.5nm AlN/1.25nm $Al_{0.9}Ga_{0.1}N$/0.5nmGaN/1.25nm $Al_{0.9}Ga_{0.1}N$ structure and secondary peaks from the GaN layers were observed, indicating the formation of 2-ML GaN.

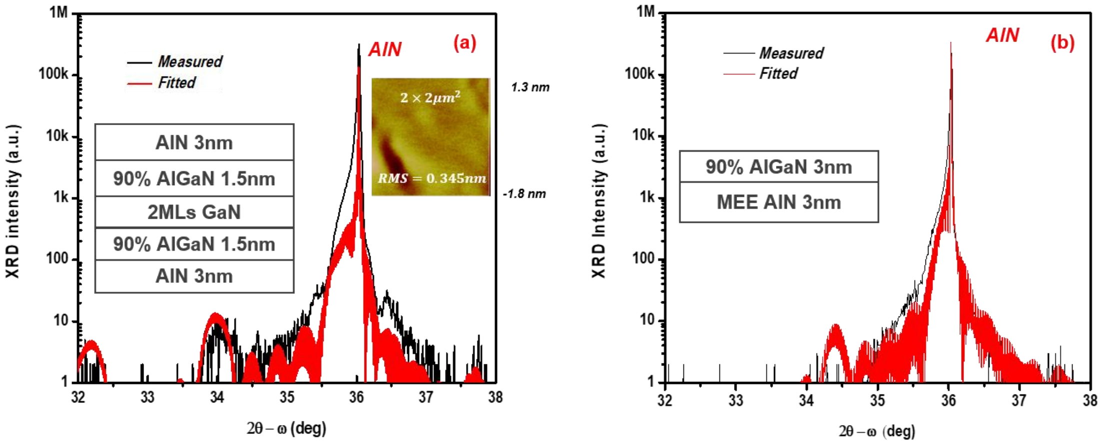

Figure 6.3*: ω-2θ HR-XRD spectra for (a) $Al_{0.9}Ga_{0.1}N$-delta-GaN QW and (b) $Al_{0.9}Ga_{0.1}N$ QW, showing the formation of $Al_{0.9}Ga_{0.1}N$ and 2 ML GaN layers. Inset: AFM image after the $Al_{0.9}Ga_{0.1}N$-delta-GaN active region growth*

Figure 6.4 inset compares the scanning transmission electron microscopy (STEM) images of the cross-section of the $Al_{0.9}Ga_{0.1}N$-delta-GaN QW and $Al_{0.9}Ga_{0.1}N$ QW. Due to the strong Z-contrast, the $Al_{0.9}Ga_{0.1}N$ and AlN can be easily distinguished in the images. The Energy-dispersive x-ray spectroscopy (EDX) from the $Al_{0.9}Ga_{0.1}N$ QW confirms the 90% Al-content from the structure. In addition, a thin bright layer is observed in between of the two $Al_{0.9}Ga_{0.1}N$ layers in figure 6.4 (a) while that is absent in figure 6.4 (b), which confirms the formation of 2-ML GaN in the MBE-grown $Al_{0.9}Ga_{0.1}N$-delta-GaN QWs.

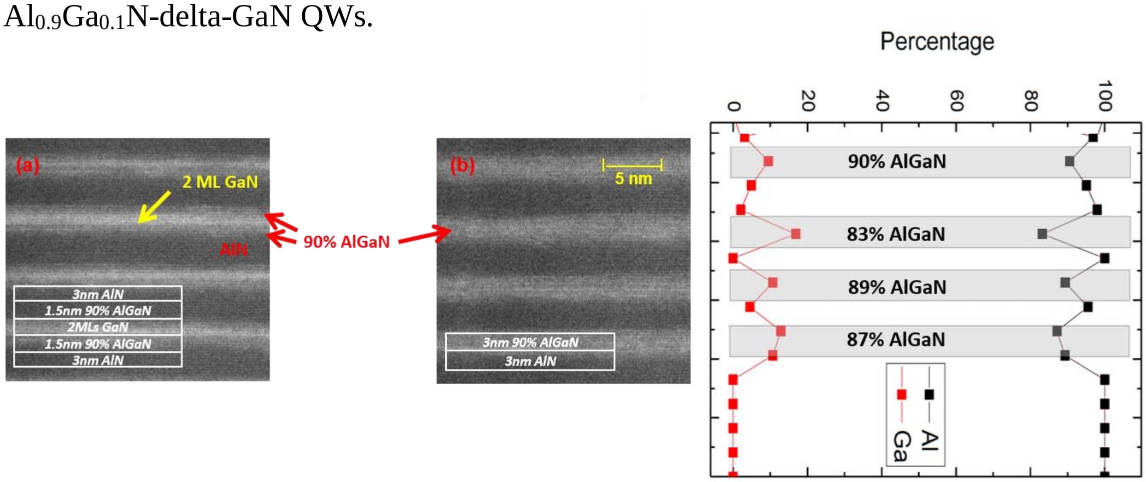

***Figure 6.4**: STEM images of (a) $Al_{0.9}Ga_{0.1}N$-delta-GaN QW and (b) 3-nm $Al_{0.9}Ga_{0.1}N$/3-nm AlN QW heterostructure.*

6.3.2 High Internal Quantum Efficiency from the MBE-grown AlGaN-delta-GaN QW

The optical properties were investigated through a temperature-dependent photoluminescence (PL) system. A pulsed Excimer laser source (λ = 193 nm, 5 ns pulse duration, 20 Hz repetition rate) was used for PL excitation. Figure 6.5 (a) shows PL spectra from grown $Al_{0.9}Ga_{0.1}N$-delta-GaN QW measured at low temperature (4 K) and room temperature (RT). The peak PL emission at 255 nm was observed for RT measurement which is consistent with the calculated results. Low-temperature PL measurement show a 2-nm PL peak wavelength blue-shift which agrees with the Varshni trend [15]. Previous studied have shown the PL linewidth and peak emission wavelength is sensitive to the thickness fluctuations of the GaN Layer. The full width at half maximum is measured as 12.8 nm from RT PL spectrum, which indicates a uniform 2-ML GaN from the epitaxial $Al_{0.9}Ga_{0.1}N$-delta-GaN QW structure. The temperature-dependent PL spectra are usually used to estimate the internal quantum efficiency. In this study, the IQE is calculated from the integrated PL intensity ratio (300 K/4 K) with assuming that non-radiative recombination is negligible at 4K, which means 100% IQE from low temperature PL. For the $Al_{0.9}Ga_{0.1}N$-delta-GaN QW, the IQE value reaches 85.8%, which is extremely high for DUV LEDs especially for the structure grown on the typical AlN template with dislocation density of 1×10^{10} cm^{-2}. For comparison, a 3-nm $Al_{0.6}Ga_{0.4}N$ QW was grown on the same AlN template and characterized by the temperature-dependent PL system in this study. As shown in figure 6.5 (b), the peak emission wavelength is observed at 260 nm. The PL intensity measured at room temperature drops significantly as compared to the low temperature value, which translates to a low IQE value of 18.23%. The IQE values from the $Al_{0.9}Ga_{0.1}N$-delta-GaN QW structure at different laser energy are plotted in figure 6.5 (c), which corresponds to different carrier densities. The results show that IQE increases as the laser energy and reaches the maximum value of 85.71%, whose trend is consistent with previous reports. Figure 6.5 (d) summarizes the IQE values reported in the literature over the range of 200 nm -300 nm in comparison to the IQE collected from this work [16]–[24]. In general, the IQE value drops for as emission wavelength becomes smaller, which typical requires higher Al-content AlGaN for the QW active region. This is because lower band offset induced carrier leakage and more edge-emissions as Al-content increases. It is encouraging that by the use of $Al_{0.9}Ga_{0.1}N$-delta-GaN QW, the IQE value is comparable to the record at similar emission wavelength, even though a conventional AlN template with high dislocation density of 1×10^{10} cm^{-2} was used. As discussed in previous studies, the proposed structure also significantly increases the TE/TM ratio, enables more photons being extracted out from the structure. The improved light extraction, combining with the high IQE value, should lead to a much higher EQE, as compared to the conventional AlGaN QW LEDs. Note that the IQE and hence the EQE can be further improved by employing the high-quality substrate, which is promising for DUV LED applications.

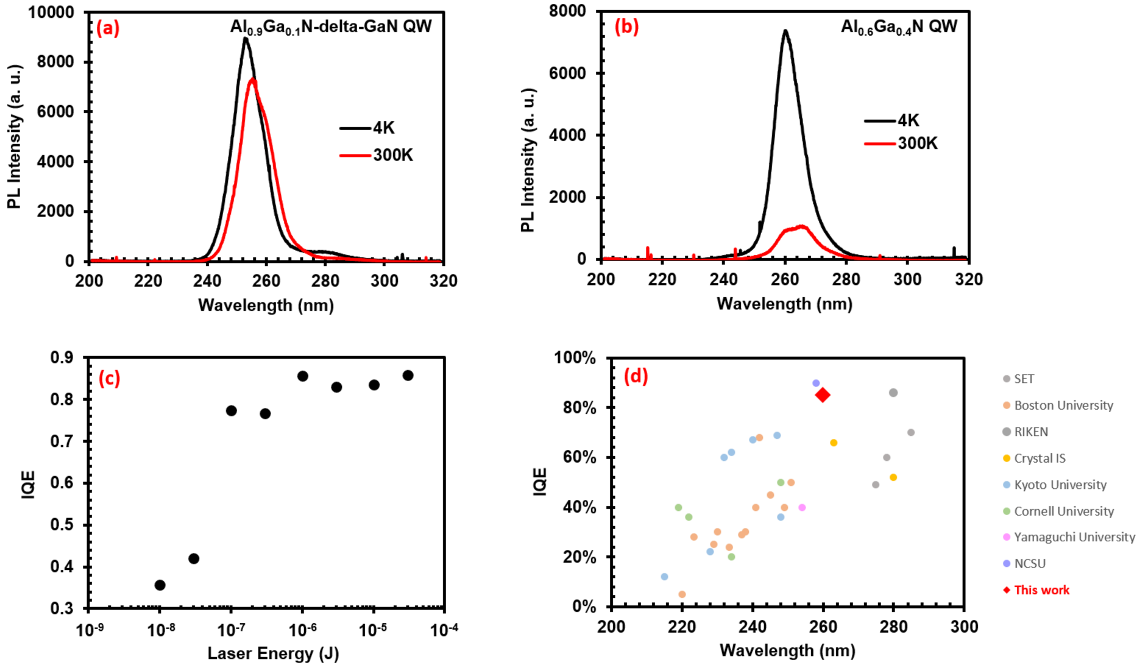

***Figure 6.5**: Photoluminescence (PL) spectra from (a) Al$_{0.9}$Ga$_{0.1}$N-delta-GaN QW and (b) 3-nm Al$_{0.6}$Ga$_{0.4}$N/3-nm AlN QW at low and room temperature; (c) IQE value from Al$_{0.9}$Ga$_{0.1}$N-delta-GaN QW as a function of laser energy; (d) Reported IQE value from DUV LEDs at different wavelengths*

6.4 Summary

In conclusion, an Al$_{0.9}$Ga$_{0.1}$N-delta-GaN QW with 5-Å delta-GaN is proposed and grew in this work to achieve 260-nm emission. Theoretical calculation shows that using the Al$_{0.9}$Ga$_{0.1}$N-delta-GaN QW, the electron-hole wave function overlap is significantly enhanced from 15.5% to 82.58%, as compared to the conventional 3-nm Al$_{0.58}$Ga$_{0.42}$N QW, which results in the 24 times and 5.2 times enhancements in the spontaneous emission rate and IQE, respectively. The proposed Al$_{0.9}$Ga$_{0.1}$N-delta-GaN QW was also developed epitaxially by using PAMBE and characterized by XRD and STEM in order to confirm the 2-ML GaN formation. A strong 260-nm emission with up to 85.71% IQE was collected from the $Al_{0.9}Ga_{0.1}N$-delta-GaN QW by performing the temperature-dependent PL measurements, indicating the AlGaN-delta-GaN QW would be a possible solution to realize high-efficiency DUV LEDs.

Reference for Chapter 6:

[1] M. Kneissl and J. Rass, *III-Nitride Ultraviolet Emitters*, 227. Springer International Publishing Cham, 2016.

[2] M. Kneissl, T. Y. Seong, J. Han, and H. Amano, "The emergence and prospects of deep-ultraviolet light-emitting diode technologies," *Nat. Photonics*, 13, 4, 233–244, 2019.

[3] M. Kneissl *et al.*, "Advances in group III-nitride-based deep UV light-emitting diode technology," *Semicond. Sci. Technol.*, 26, 1, 014036, 2011.

[4] T.-Y. Seong, H. Jung, H. Amano, and H. Morkoc, *III-Nitride Based Light Emitting Diodes and Applications*, (2nd Ed.)., 133. Dordrecht: Springer Netherlands, 2017.

[5] S. Vilhunen, H. Särkkä, and M. Sillanpää, "Ultraviolet light-emitting diodes in water disinfection," *Environ. Sci. Pollut. Res.*, 16, 4, 439, 2009.

[6] M. A. Würtele *et al.*, "Application of GaN-based ultraviolet-C light emitting diodes - UV LEDs - for water disinfection," *Water Res.*, 45, 3, 1481, 2011.

[7] T. Takano, T. Mino, J. Sakai, N. Noguchi, K. Tsubaki, and H. Hirayama, "Deep-ultraviolet light-emitting diodes with external quantum efficiency higher than 20% at 275 nm achieved by improving light-extraction efficiency," *Appl. Phys. Express*, 10, 031002, 2017.

[8] C. Liu, K. Lee, S. M. Islam, H. Xing, D. Jena, and J. Zhang, "Demonstration of AlGaN-delta-GaN QW by plasma-assisted molecular beam epitaxy for 260-nm ultraviolet light emitting diodes," February 2018, 31, 2018.

[9] J. Zhang and N. Tansu, "Engineering of AlGaN-delta-GaN quantum-well gain media for mid- and deep-ultraviolet lasers," *IEEE Photonics J.*, 5, 2, 2013.

[10] J. Zhang, H. Zhao, and N. Tansu, "Large optical gain AlGaN-delta-GaN quantum wells laser active regions in mid- and deep-ultraviolet spectral regimes," *Appl. Phys. Lett.*, 98,

171111, 2011.

[11] C. Liu, Y. K. Ooi, S. M. Islam, H. G. Xing, D. Jena, and J. Zhang, “234 nm and 246 nm AlN-Delta-GaN quantum well deep ultraviolet light-emitting diodes,” *Appl. Phys. Lett.*, 112, 1, 2018.

[12] C. Liu *et al.*, “Physics and polarization characteristics of 298 nm AlN-delta-GaN quantum well ultraviolet light-emitting diodes,” *Appl. Phys. Lett.*, 110, 071103, 2017.

[13] J. Encomendero *et al.*, “Room temperature microwave oscillations in GaN/AlN resonant tunneling diodes with peak current densities up to 220 kA/cm2,” *Appl. Phys. Lett.*, 112, 10, 2018.

[14] H. Zhao, G. Liu, J. Zhang, R. A. Arif, and N. Tansu, “Analysis of internal quantum efficiency and current injection efficiency in III-nitride light-emitting diodes,” *IEEE/OSA J. Disp. Technol.*, 9, 4, 212–225, 2013.

[15] S. M. Islam *et al.*, “Deep-UV emission at 219 nm from ultrathin MBE GaN/AlN quantum heterostructures,” *Appl. Phys. Lett.*, 111, 091104, 2017.

[16] S. M. Islam, V. Protasenko, S. Rouvimov, H. G. Xing, and D. Jena, “Sub-230 nm deep-UV emission from GaN quantum disks in AlN grown by a modified Stranski – Krastanov mode diodes Sub-230 nm deep-UV emission from GaN quantum disks in AlN grown by a modified Stranski – Krastanov mode,” *Jpn. J. Appl. Phys.*, 55, 05FF06, 2016.

[17] M. Shatalov *et al.*, “AlGaN deep-ultraviolet light-emitting diodes with external quantum efficiency above 10%,” *Appl. Phys. Express*, 5, 8, 28–31, 2012.

[18] Z. Bryan, I. Bryan, J. Xie, S. Mita, Z. Sitar, and R. Collazo, “High internal quantum efficiency in AlGaN multiple quantum wells grown on bulk AlN substrates,” *Appl. Phys. Lett.*, 106, 14, 1–5, 2015.

[19] M. Shatalov *et al.*, “Efficiency of light emission in high aluminum content AlGaN quantum wells,” *J. Appl. Phys.*, 105, 7, 2009.

[20] H. Murotani, D. Akase, K. Anai, Y. Yamada, H. Miyake, and K. Hiramatsu, “Dependence of internal quantum efficiency on doping region and Si concentration in Al-rich AlGaN quantum wells,” *Appl. Phys. Lett.*, 101, 4, 2012.

[21] T. Y. Wang, C. T. Tasi, C. F. Lin, and D. S. Wuu, “85% internal quantum efficiency of 280-nm AlGaN multiple quantum wells by defect engineering,” *Sci. Rep.*, 7, 1, 1–8, 2017.

[22] P. Sun *et al.*, “Advantages of AlGaN-based deep ultraviolet light-emitting diodes with a superlattice electron blocking layer,” *Superlattices Microstruct.*, 85, 59, 2015.

[23] T. D. Moustakas *et al.*, “Deep UV-LEDs with high IQE based on AlGaN alloys with strong band structure potential fluctuations,” *Light. Diodes Mater. Devices, Appl. Solid State Light. XVI*, 8278, February, 82780L, 2012.

[24] C. Frankerl *et al.*, “Challenges for reliable internal quantum efficiency determination in AlGaN-based multi-quantum-well structures posed by carrier transport effects and morphology issues,” *J. Appl. Phys.*, 126, 7, 2019.

CHAPTER 7: Concepts for Improving DUV Light-Emitting Diodes Efficiency

7.1 Light Extraction Properties of the UV LEDs with Self-Assembled Microsphere Arrays

As discussed in chapter 2, light extraction efficiency remains a big challenge for high-efficiency deep-UV LEDs due to the high refractive index contrast between AlN (sapphire) and air To address this issue and improve the η_{ext} of UV LEDs, various nanostructuring approaches have been proposed [1]–[8]. One possible solution is to change the angle between the photon emission direction and the surface normal by using encapsulation [1], photonic crystal structure [2], front side and back side surface roughening, patterned sapphire substrate [3], [7] and nanowire structure [8]. Several research groups also tried to collect the light emitted in the opposite directions toward the p-AlGaN layer for the bottom-emitting UV LEDs by using UV-reflective metal and UV-transparent P-AlGaN layer [2], [4], [5]. Up to 20% η_{EQE} has been reported by employing these techniques recently[4]. However, all of those include complex and expensive fabrication processes. Instead, a low-cost, large-yield and easy controlled approach by using microsphere arrays to improve device light extraction efficiency has been developed and demonstrated for visible LEDs [9]–[13]. Specifically, self-assembled two-dimensional close-packed SiO_2 microsphere arrays are coated on top/bottom of the devices, serve to scatter light emitted from the active region of the LED, allowing light which would normally be subject to total internal reflection to escape the device into air. The use of intermediate refractive index materials such as SiO_2 or polystyrene to form this nanostructured array also serves to reduce Fresnel reflection, further improving the light extraction efficiency of the device. As a result, up to 1.85 times light extraction efficiency enhancement can be realized. However, this concept has not been demonstrated in deep-UV regime, where photons with different polarizations should be considered separately [9]–[13].

Therefore, in this work, we used both experimental and simulation approaches to test the feasibility of increasing light extraction efficiency through the use of a self-assembled, close-packed monolayer of SiO_2 microspheres for deep-UV LEDs. A flip-chip UV LED with emission wavelength of 280 nm was examined. The light extraction characteristics from the LEDs were examined by an angle-dependent EL setup and compared with those of UV LEDs without microsphere arrays. Due to the lower refractive index from SiO_2 as compared to sapphire substrate and the sphere shape of the SiO_2 array, the TE-polarized light intensities are enhanced at the small angles with respect to the c-axis. In addition, here we also employed a FDTD method to theoretically study device near-filed electric field distribution and light radiation properties. The results show great consistency with the measurement results, confirming the use of SiO_2 microsphere arrays could enhance device intensities at small angles.

7.1.1 Experimental setup and results discussion

The schematic of the 280-nm UV LED structure is shown in Figure 7.1 (a). The sample was grown on AlN/sapphire substrate, consisting of a 2-nm $Al_{0.6}Ga_{0.4}N$/2-nm AlN superlattice (SL) buffer layer, a 2-μm n-$Al_{0.55}Ga_{0.45}N$ layer, a five-period 3-nm $Al_{0.35}Ga_{0.65}N$/10-nm $Al_{0.43}Ga_{0.57}N$ MQW active region and a 40-nm p-$Al_{0.55}Ga_{0.45}N$ with

160 nm p-GaN layer. After the growth, the epitaxial structure was fabricated to be a flip-chip LED and mounted on a commercial device holder. To study the use of a self-assembled, close-packed monolayer of SiO_2 microspheres for deep-UV LEDs, we prepared several double-side polished sapphire pieces with SiO_2 microspheres coating on the surface and placed the sphere coated sapphire onto the UV LED sample, as shown in Figure 7.1 (b). Figure 7.1 (c) shows the scanning electron microscopy (SEM) image of the 700-nm close-packed monolayer of SiO_2 microspheres. The UV LED samples with sapphire piece on top were then measured by an in-house angle-dependent EL measurements setup, as shown in Figure 7.1(d). Specifically, the sample was placed at the center of the stage while the optical fiber, which is connected to the spectrometer, was fixed on a rotatable stage. By rotating the fiber holder, the EL spectra at different angles can be collected and further translated into light radiation pattern.

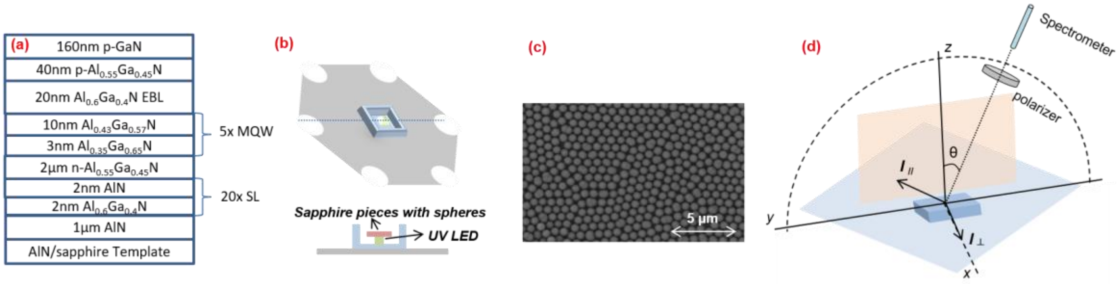

***Figure 7.1**: (a) Schematic of 280-nm UV LED heterostructure (b) Experimental setup for measurement of light emission from the LED device, showing the commercial UV LED beneath sphere coated sapphire. (c) SEM image of the close-packed microsphere array deposited on sapphire. (d) Schematic representation of the angle dependent EL setup used to measure light extraction and far field radiation patterns of the device.*

The sapphire pieces with and without the microspheres array were placed on the LED samples and compared under the same test conditions. From the EL spectra as shown in Figure 7.2 (a) inset, both devices show strong emissions at 280 nm. Figure 7.2

plots the integrated EL intensities as a function of current for the structures with and without microsphere arrays. At θ = 0°, the sample with microsphere array show 8% enhancement of the integrated EL intensity as compared to that from the structure without microsphere array. Further investigate the influence of the microsphere array on the light extraction efficiency of the UV LED, the EL intensities at different emitting angles were collected. Figure 7.2 (b) plots the light radiation patterns for the structures with and without the microsphere arrays. The results show at smaller angle (θ < 30°), the light intensities from the structure with microsphere array are larger than that from the structure without the microspheres while at larger angles (30° < θ < 60°), the intensities decrease by the use of the microsphere arrays.

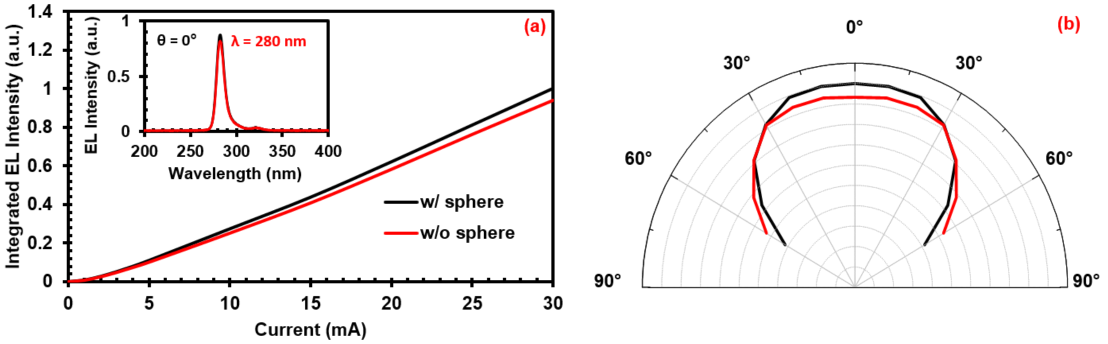

***Figure 7.2**: (a) Integrated EL intensity as a function of current for the structure with microsphere arrays (black) and without microsphere arrays (red) Inset: EL spectra of the structures with (black) and without (red) the 700-nm microspheres array at θ = 0°. (b) Light radiation pattern from the structures with microsphere arrays (black) and without microsphere arrays (red), showing the EL intensity enhancements at small angles θ < 30°.*

7.1.2 Physics and Simulation results

To investigate the physics of the influence of the microsphere arrays on the UV LED light extraction profiles, several FDTD simulations were performed and analyzed using Synopsys R-soft. Layer thicknesses and material constants are assigned according to Table 1. A hexagonal close-packed array of SiO_2 spheres of variable defined diameter was located atop and adjacent to the sapphire layer. A perfect electric conductor (PEC) boundary condition was assigned to the free surface of the p-GaN layer to represent the metal current spreading layer which would exist in this location in a real device. All other simulation boundaries were assigned as perfectly matched layers (PMLs). The simulation domain was set to be 6 µm x 6 µm and a single isotropically emitting point source was used to produce 280 nm UV light. More simulation results can be found in ref. [14].

Table 7.1: Refractive index and absorption coefficient used in the simulations

$\lambda = 280$ nm	n	α (cm^{-1})
Sapphire	1.82	0
AlN buffer	2.42	0
n-AlGaN	2.49	10
AlGaN MQW	2.54	10
AlGaN EBL	2.43	7
p-AlGaN	2.49	10
p-GaN	2.63	170544
SiO_2	1.49	0

The simulation was completed for four distinct device structures, one with no SiO_2 spheres, and then with 280, 500, and 700 nm diameter spheres. The simulated cross-sectional electric fields from the four structures are presented in Figure 7.3. For the planar structure without SiO_2 spheres, the electric field from TE-polarized light shows large intensities at smaller angles while most of the E-fields are kept within the LED structure at larger angles which indicates the lambertian radiation pattern from the structure. For the structures with the spheres, the results show a marked increase in light emission intensity at smaller angles for TE-polarized light, while a slight decrease in intensity at intermediate angles is also evident. The SiO_2 spheres appear to act as resonant cavities, serving to amplify extraction of light normal to the surface of the sapphire. This can be seen most readily for the TE-polarized 500 nm SiO_2 spheres in Figure 7.3. TM-polarized light also appears to benefit from the addition of the sphere monolayer to the sapphire substrate. The cross-sectional electric fields shown in Figure 7.3 indicate enhanced light extraction at multiple angles, and for the 280 and 500 nm sphere arrays in particular.

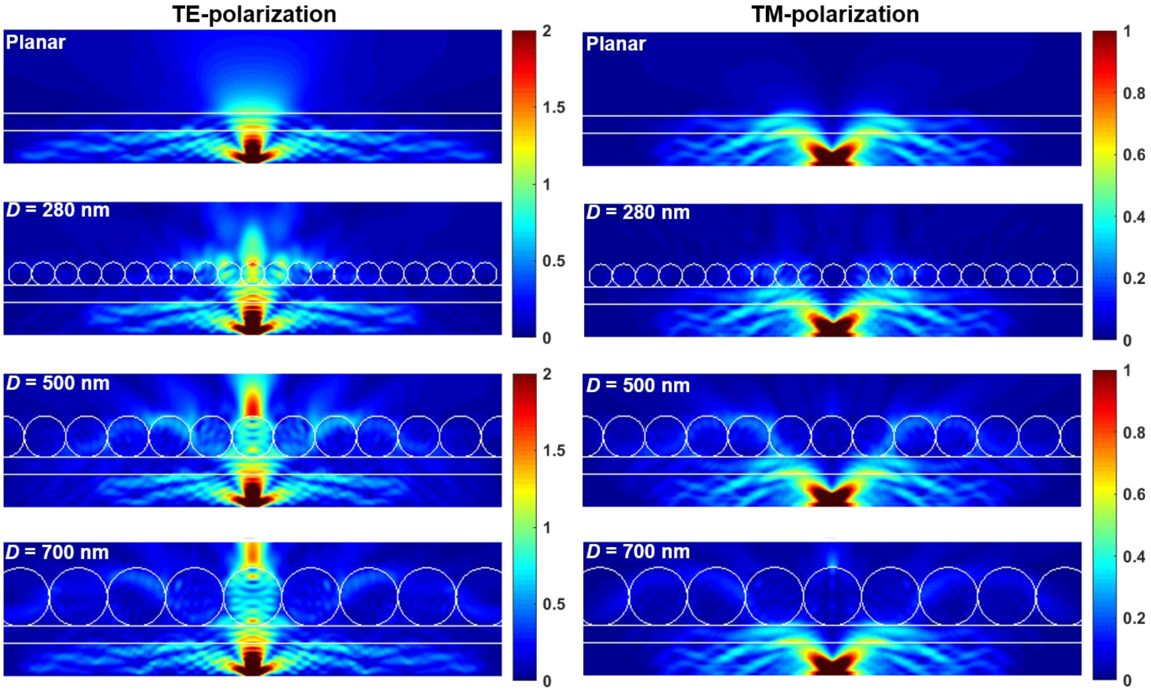

***Figure 7.3**: Cross-sectional electric field maps produced by FDTD simulation for the structures without spheres, with 280 nm spheres, 500 nm spheres and 700 nm spheres.*

Figure 7.4 plots both TE- and TM-polarized far-field patterns of the structures. The results clearly show the large intensities enhancements at smaller angles as compared to the planar structure for the TE-polarized light, which show great consistency with the measurements results and the intensities reach the highest with the use of the 700 nm spheres. For TM-polarization, the donut-shape radiation patterns are observed for all the structures. Instead of the perfect donut shape for the planar structure, the spheres scatter the light and enhance the intensities only at several angles which are determined by the spheres size, while the intensities drop at other angles. The simulation results verify that the use of SiO_2 microspheres array resulted in scattering of photons at the sapphire/SiO_2 microspheres interface, which eventually leads to enhanced TE-photons extraction at small-angles.

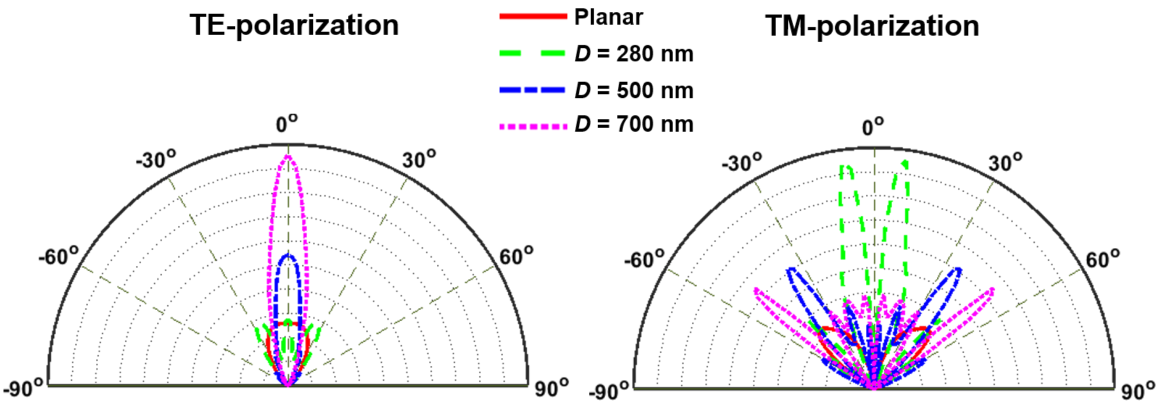

***Figure 7.4**: Polarized light radiation patterns produced by FDTD simulation for the structures without spheres, with 280 nm spheres, 500 nm spheres and 700 nm spheres.*

In summary, the feasibility of using 700-nm SiO_2 microspheres arrays on 280 nm flip-chip UV LEDs to improve light extraction efficiency was investigated in this study. Angle-dependent EL measurements have been compared for the LEDs with and without microspheres, showing light intensities are enhanced at small angles and decreased at larger angles with respect to the c-axis. Cross-sectional near-filed electric field and light radiation patterns from FDTD simulation confirm the use of microspheres array results in scattering of photons at the sapphire/ SiO_2 interface and hence the light intensities enhancement at small angles.

7.2 The Use of AlGaN Substrates for DUV Emissions

AlGaN-based deep-ultraviolet (DUV) lasers and light-emitting diodes (LEDs) with emission wavelength of 240 - 260 nm have shown great potential in various applications such as water purification, sterilization, space communication and sensing systems [1-5]. Although tremendous progress have been achieved during the past decade [1], [19], such III-nitride DUV emitters are still challenging because of their low efficiency [1], [20]. A significant contribution to the low efficiencies is the high defect density in III-nitride materials. Specifically, most of the AlGaN-based UV lasers and LEDs are grown on AlN/sapphire template which yield large threading dislocation densities (TDD) in the level of 10^{10} cm^{-2}. These threading dislocations are responsible for some of the non-radiative recombination centers, leading to the low internal quantum efficiency (IQE) [1]. To reduce the dislocation density, different approaches have been proposed. For example, H. Hirayama *et al*. developed an ammonia pulsed-flow technique on patterned sapphire substrate to reduce the threading dislocation density from 1×10^{10} cm^{-2} down to 5×10^{8} cm^{-2} [1], [21]. As a result, the IQE was significantly enhanced from 1% to 60% [1]. However, even though the substrate/buffer is optimized, there are still some unavoidable defects generated throughout the thick n-AlGaN layer growth. Alternatively, several research groups used AlN as the barrier layer to control the defects, but the fact whether it sacrifices the injection efficiency is still under debate [10-12]. Besides the lack of suitable substrates, another factor limiting the performance of DUV lasers and LEDs with emission wavelengths of 240 - 260 nm is the valence band mixing effect [1], [25], as discussed in chapter 2.. To address this issue, our previous studies have proposed several structures such as Al(Ga)N-delta-GaN [13-15] in chapter 4-6 and AlInN-delta-GaN quantum wells (QWs) [29] in chapter 4 to realize high-efficiency TE-polarized DUV emissions. However, all these proposed structures require complex epitaxial growths. Therefore, there is a strong need to develop new techniques overcoming such limitations from conventional AlGaN-based UV lasers and LEDs. The use of $Al_xGa_{1-x}N$ substrates with proper Al-content (x) would be a possible solution to address this issue [30]. Recently, several research groups and companies have already developed high-quality free-standing AlGaN substrates [18-20], which enables the further development in optical applications. However, the physics and optical properties of AlGaN-based lasers and LEDs on such AlGaN substrates with considering the strain effect are still relatively lacking.

In this work, we theoretically investigated the band structures and optical properties of $Al_xGa_{1-x}N/Al_yGa_{1-y}N$ QWs on $Al_yGa_{1-y}N$ substrate by using a self-consistent 6-band ***k·p*** model [21-24] introduced in appendix B. All the parameters used in this study are taken from Ref. [34] under room-temperature condition and listed in appendix A. The quantum well and barrier thickness were kept at 3-nm throughout the simulations. Both TE- and TM-polarized optical gains and spontaneous emission rates were calculated based on the Fermi’s Golden Rule for all the structures by taking into account all the transitions from the conduction band to ground state valence subbands (HH, LH and CH).

7.2.1 Physics and Simulation results

Figure 7.5(a) plots the in-plane ($\varepsilon_{xx}/\varepsilon_{yy}$) strains in the active region as a function of Al-content (x) in the $Al_xGa_{1-x}N$ QW. Two different substrate types, $Al_{0.72}Ga_{0.28}N$ and AlN were calculated and compared. In general, by the use of AlGaN substrate, the QW regions have smaller lattice mismatch as compared to that on AlN substrate. Therefore, the in-plane strains are significantly reduced by the use of AlGaN substrate, which leads to the reductions of the piezoelectric polarization and internal electrostatic field in the QW. Specifically, $Al_{0.48}Ga_{0.52}N/Al_{0.72}Ga_{0.28}N$ QW and $Al_{0.51}Ga_{0.49}N$/AlN QW were designed to realize 260-nm emission on $Al_{0.72}Ga_{0.28}N$ substrate and AlN substrate, respectively. The in-plane strain for $Al_{0.48}Ga_{0.52}N/Al_{0.72}Ga_{0.28}N$ QW is reduced by 51.09%, as compared to the $Al_{0.51}Ga_{0.49}N$/AlN QW. With the significant reduction of the in-plane strain and internal electric field, the charge separation will be significantly improved by the use of AlGaN substrate.

To verify the influence of the reduced in-plane strain on QW properties, the band energy lineups of $Al_{0.48}Ga_{0.52}N/Al_{0.72}Ga_{0.28}N$ QW on $Al_{0.72}Ga_{0.28}N$ substrate and $Al_{0.51}Ga_{0.49}N$/AlN on AlN substrate, as well as the ground state electron and hole wave functions were simulated and compared in Figures 7.5(b)-(c). All the results were calculated at carrier density of $n = 5\times10^{19}\ cm^{-3}$. For the $Al_{0.51}Ga_{0.49}N$/AlN QW, there is a large strain effect exists in the structure, which translates into a large Quantum Confined Stark Effect (QCSE) for the structure, pushing the ground state electron and hole wave functions to the opposite sides of the QWs. Therefore, only 27.45% electron-hole wave function overlap can be achieved for this structure. As a comparison, once the Al-content in the barrier and substrate decreases down to 72%, the 51.09% reduction of the in-plane strain result in a much larger wave function overlap (55.75%). As a result, relatively larger spontaneous emission rates and optical gain can be expected from this structure, as compared to that of the $Al_{0.51}Ga_{0.49}N$/AlN QW. The valence band structures from both QWs were also calculated, showing the dominant transition from both structures is the ground state conduction band (C1) to the ground state heavy hole (HH1), which indicates the majority of the photons generated from the active regions are TE-polarized.

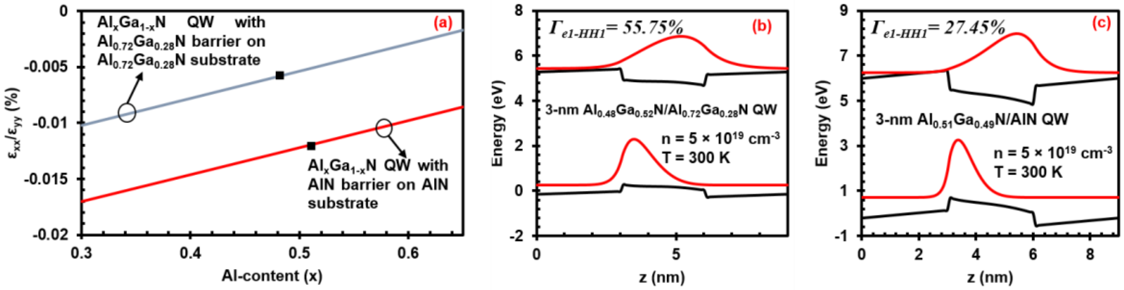

***Figure 7.5**: (a) In-plane ($\varepsilon_{xx}/\varepsilon_{yy}$) strains in the active region as a function of Al-content (x) in the $Al_xGa_{1-x}N$ QW. Band energy lineups with ground state electron and hole wave functions from (b) $Al_{0.48}Ga_{0.52}N/Al_{0.72}Ga_{0.28}N$ QW on $Al_{0.72}Ga_{0.28}N$ substrate and (c) $Al_{0.51}Ga_{0.49}N$/AlN QW on AlN substrate.*

Integrated spontaneous emission rate ($\boldsymbol{R_{sp}}$) is a key determinant of LED $\boldsymbol{\eta_{Rad}}$, which in turn decides device IQE. Therefore, the $\boldsymbol{\eta_{Rad}}$ from the $Al_{0.48}Ga_{0.52}N$/ $Al_{0.72}Ga_{0.28}N$ QW and the $Al_{0.51}Ga_{0.49}N$/AlN QW at different carrier densities were calculated and plotted in Figure 7.6 (a). In general, both TE- and TM-polarized $\boldsymbol{R_{sp}}$ shown great enhancements by the use of AlGaN substrate. Specifically, at carrier density of n = 5×10^{19} cm^{-3}, the TE-polarized $\boldsymbol{R_{sp}}$ was calculated as 7.09 × 10^{26} $s^{-1}cm^{-3}$ from the $Al_{0.48}Ga_{0.52}N$/ $Al_{0.72}Ga_{0.28}N$ QW, which is 4.1 times larger than that from the $Al_{0.51}Ga_{0.49}N$/AlN QW. As discussed earlier, the enhanced $\boldsymbol{R_{sp}}$ value is attributed to the reduced in-plane strain (~51.09%) and therefore improved wave function overlap (55.75% vs. 27.45%). Note that TM-polarized

$\boldsymbol{R_{sp}}$ is comparable to TE-polarized $\boldsymbol{R_{sp}}$ for Al$_{0.48}$Ga$_{0.52}$N/ Al$_{0.72}$Ga$_{0.28}$N QW, but not for Al$_{0.51}$Ga$_{0.49}$N/AlN QW. This is because that the strain effect influences the valence band crossover point, at which HH and CH subbands have same energy level. Specifically, the Al$_{0.48}$Ga$_{0.52}$N/ Al$_{0.72}$Ga$_{0.28}$N QW is more close to the valence band crossover point, and therefore the C1-CH1 transition is unneglectable in this structure, which generates TM-polarized photons.

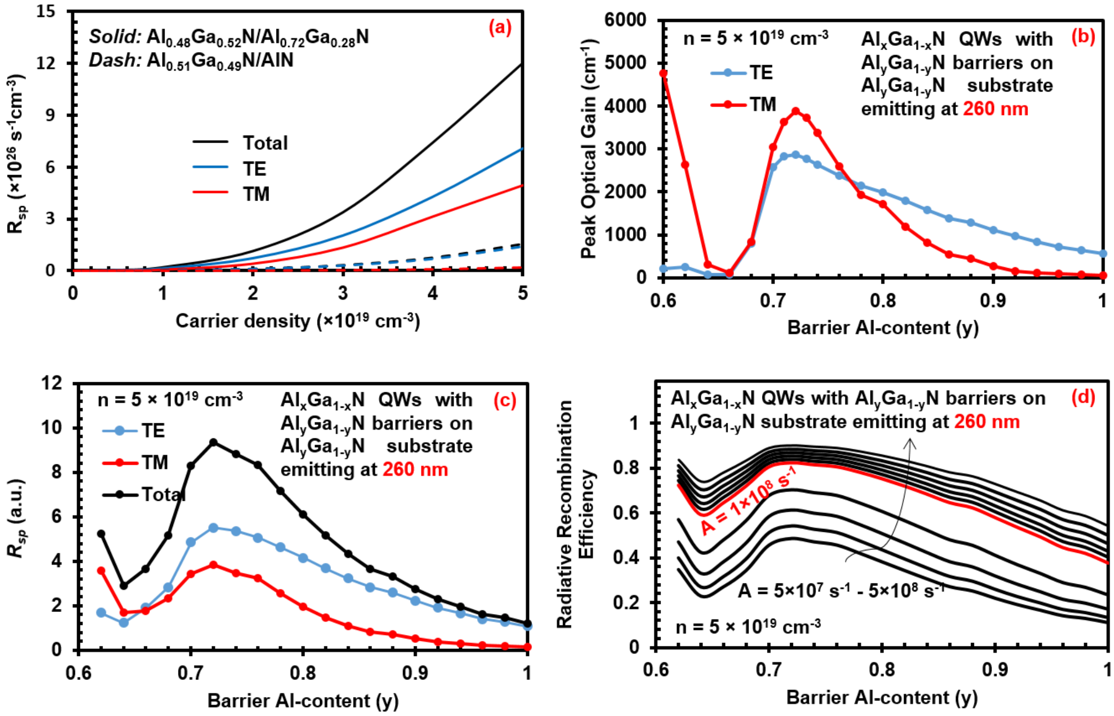

Figure 7.6*: (a) TE-polarized (blue), TM-polarized (red) and total (black) spontaneous emission rate per unit volume (*$\boldsymbol{R_{sp}}$*) as a function of carrier density from Al*$_{0.48}$*Ga*$_{0.52}$*N/Al*$_{72}$*Ga*$_{28}$*N QW (solid line) and Al*$_{0.51}$*Ga*$_{0.49}$*N/AlN QW (dash line). (b) TE- (blue) and TM-polarized (red) peak optical gains from Al*$_x$*Ga*$_{1-x}$*N/Al*$_y$*Ga*$_{1-y}$*N QW with different substrate/barrier Al-contents (y) for 260-nm emissions. (c) TE-polarized (blue), TM-polarized (red) and total (black)* $\boldsymbol{R_{sp}}$ *from Al*$_x$*Ga*$_{1-x}$*N/Al*$_y$*Ga*$_{1-y}$*N QW with different substrate/barrier Al-contents (y) for 260-nm emissions. (d) Radiative recombination efficiencies at different SRH coefficient (A) levels from Al*$_x$*Ga*$_{1-x}$*N/Al*$_y$*Ga*$_{1-y}$*N QW on different substrate/barrier Al-contents for 260-nm emissions. Carrier density level from the simulations is n = 5 × 10*^{19} *cm*$^{-3}$*.*

The use of $Al_{0.72}Ga_{0.28}N$ substrate is demonstrated to be capable of improving ***R_{sp}*** from the AlGaN/AlGaN QW structures. Furthermore, the influence of Al-content (x) from $Al_xGa_{1-x}N$ substrate on device optical properties is also studied in this work. Figures 7.6 (b) and 7.6 (c) plot the polarized optical gain characteristics and ***R_{sp}*** for the QWs emitting at 260 nm with different barrier (substrate) Al-compositions at carrier density of $n = 5\times10^{19}$ cm^{-3}, respectively. The Al-contents (x) from those $Al_xGa_{1-x}N$ QWs are selected to aim for 260 nm emission at $n = 5\times10^{19}$ cm^{-3}. For most of the QWs on $Al_xGa_{1-x}N$ substrate (except those QWs close to Al-content of x=0.64), both optical gains and ***R_{sp}*** are largely enhanced, as compared to that from the structure with AlN barrier (substrate) due to the reduced strain effect/QCSE and therefore improved electron-hole wave function overlaps. Specifically, TE- and TM-polarized optical gains from the $Al_{0.48}Ga_{0.52}N/Al_{0.72}Ga_{0.28}N$ QW on $Al_{0.72}Ga_{0.28}N$ substrate were calculated as 2875 cm^{-1} and 3877 cm^{-1} which correspond to ~5.2 times and ~60 times as large of that from the $Al_{0.51}Ga_{0.49}N$/AlN QW on AlN substrate, respectively. Note that both peak optical gain and ***R_{sp}*** drop significantly when the barrier Al-content decreases from 0.72 to 0.6. One of the reasons is the reduced electron-hole wave function overlap due to the lower barrier height and carrier screening effect. But more importantly, the structure suffers from severe band mixing effect in this regime. For the structure with the barrier Al-content of 0.64, the QW Al-content for realizing 260-nm emission is near the valence band crossover point. Therefore, the carriers are equally populated at all the three valence subbands, which results in insufficient C-HH or C-CH transitions. Consequently, the optical gains and ***R_{sp}*** were significantly reduced for the structures near the crossover point.

In addition, the $\boldsymbol{R_{sp}}$ values were also translated into $\boldsymbol{\eta_{\mathrm{Rad}}}$ by using ABC-model and plotted in Figure 7.6 (d) ($\boldsymbol{\eta_{Rad}} = \frac{R_{sp}}{A \cdot n + R_{sp} + C \cdot n^3}$) [38]. Here, coefficient A represents SRH recombination coefficient while C stands for the Auger coefficient. The SRH recombination coefficient is strongly influenced by the defect density in the materials and inverse proportional to the SRH recombination lifetime. Typical value for the SRH recombination lifetime is a few tens of picoseconds, while up to 10 ns lifetime can be achieved if high-quality bulk AlN substrate is used, which corresponds to 1×10^{8} s^{-1} [1]. For the Auger coefficient, it is still being heavily debated, especially for AlGaN-based DUV LEDs. The reported value ranges from 2×10^{-30} cm^6/s to 3.4×10^{-34} cm^6/s [1], [39]. In this study, the Auger coefficient was set to be 1×10^{-33} cm^6/s while SRH recombination coefficient varied from 5×10^{7} s^{-1} - 5×10^{8} s^{-1} [1]. Figure 7.6 (c) plots $\boldsymbol{\eta_{\mathrm{Rad}}}$ values for the QW structures on different AlGaN substrates. It is clear that $\boldsymbol{\eta_{\mathrm{Rad}}}$ values are improved by the use of AlGaN substrates with different SRH recombination coefficient because of the enhanced $\boldsymbol{R_{sp}}$. Specifically, at $A = 1\times10^{8}$ s^{-1}, the radiative recombination efficiency increases from 37.7% for the $Al_{0.51}Ga_{0.49}N$/AlN QW on AlN substrate to 82.4% for the $Al_{0.48}Ga_{0.52}N/Al_{0.72}Ga_{0.28}N$ QW on $Al_{0.72}Ga_{0.28}N$ substrate. Besides improving $\boldsymbol{R_{sp}}$ value, the use of AlGaN substrate instead of AlN substrate can further reduce the dislocation density during the thick n-AlGaN layer growth, which in turn leads to a lower A value. For example, the radiative recombination efficiency from the $Al_{0.48}Ga_{0.52}N/Al_{0.72}Ga_{0.28}N$ QW will reached 90.12% if low dislocation density is observed during the growth ($A = 5\times10^{7}$ s^{-1}). The boost of the radiative recombination efficiency and therefore the internal quantum efficiency indicates the $Al_xGa_{1-x}N/Al_yGa_{1-y}N$ QWs on $Al_yGa_{1-y}N$ templates are promising for deep-UV applications.

The use of AlGaN substrate does not only show promising results at 260 nm, but also at shorter wavelengths (240 - 250 nm) at which the conventional AlGaN QW suffers from the severe band mixing effect. Figure 7.7 (a) plots the critical Al-contents, at which ground state HH and CH subbands have same energy level, for different substrates. The Al-contents (x) from those $Al_xGa_{1-x}N$ QWs are selected to aim for λ ~ 240 nm, 250 nm, and 260 nm emissions at $n = 5\times10^{19}$ cm^{-3}, respectively. The results show an increasing trend with the increase of the barrier Al-content due to the combined strain effect and barrier height adjustment [40]. Near the crossover point, the carriers are equally populating the top valence subbands which results in insufficient electron to hole transitions. In addition to the crossover points, the Al-contents required to realize λ ~ 240 - 260 nm emissions for different barriers/substrates are also plotted in Figure 7.7 (a) as dash lines. The intersection points of the solid line and each dash lines, at which the structures suffer from severe band mixing effect are observed at x = 0.64, 0.74 and 0.87 for 260nm, 250 nm and 240 nm emissions, respectively. Figures 7.7 (b)-4(c) present the peak optical gains of QWs with different barrier/substrate Al-contents at carrier density of $n = 5 \times 10^{19}$ cm^{-3}. The emission wavelengths were controlled at λ ~ 250 nm for Figure 7.7 (a). Similar to the results at 260 nm, both TE and TM-polarized optical gains were enhanced by the use of AlGaN substrates except near the crossover point, especially for TM-polarized optical gains. For example, the TM-polarized optical gain from the $Al_{0.59}Ga_{0.41}N/Al_{0.78}Ga_{0.22}N$ QW on $Al_{0.78}Ga_{0.22}N$ substrate is 38 times larger than that from the $Al_{0.72}Ga_{0.28}N$/AlN QW. For 240 nm, since TE-polarized optical gains for different substrates are almost identical to that for the structure on AlN substrate, the enhancements of the optical properties are mainly observed for TM-polarized emissions.

By carefully selecting barrier/substrate Al-content, the TM-polarized optical gain can achieve as high as 9766 cm^{-1}, which again proves the potential of AlGaN substrate for deep-UV emitters.

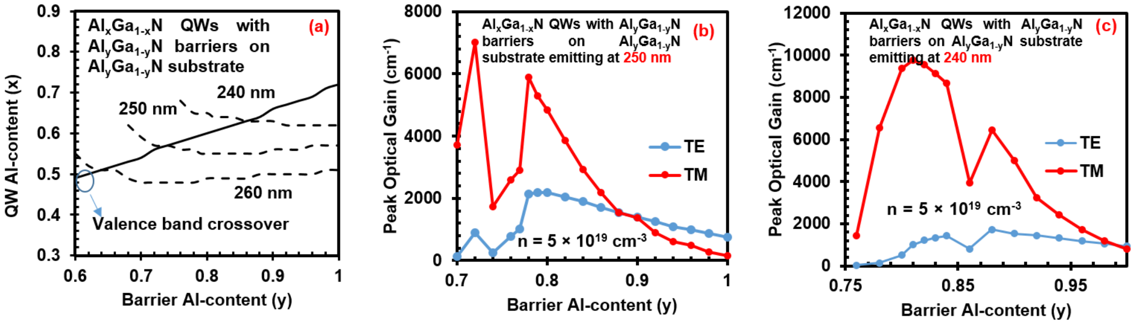

***Figure 7.7**: (a) Critical Al-content at which HH and CH subbands have same energy level (solid line) and QW Al-contents for 240nm, 250 nm and 260 nm emissions (dash lines); TE-polarized (blue) and TM-polarized (red) peak optical gains from $Al_xGa_{1-x}N/Al_yGa_{1-y}N$ QW on different substrate/barrier Al-contents for (b) 250-nm and (c) 240-nm emissions with carrier density of n = 5 × 10^{19} cm^{-3}.*

7.2.2 Summary

This work theoretically investigates the optical properties and quantum efficiencies of the AlGaN-based QW on AlGaN substrates. The physics analysis based on a self-consistent 6-band ***k·p*** model shows the transverse electric (TE)-polarized optical gain increases from 558 cm^{-1} by using $Al_{0.51}Ga_{0.49}N$/AlN QW on AlN substrate to 2875 cm^{-1} by using $Al_{0.48}Ga_{0.52}N/Al_{0.72}Ga_{0.28}N$ QW on $Al_{0.72}Ga_{0.28}N$ substrate at 260 nm, which is attributed to the reduced strain effect and valence band rearrangement by using the AlGaN substrate. Correspondingly, the radiative recombination efficiency increases 1.66 - 4.43 times base on different Shockley-Read-Hall coefficients, indicating the promising potential of the use of AlGaN substrate for high-efficiency DUV lasers and LEDs.

7.3 Current Spreading Layer Based on Nanosphere Lithography

Due to the poor p-type doping in AlGaN material, several methods have been proposed to improve the hole injection efficiency. Some reports engineered the p-AlGaN layer to address this issue such as polarization-doping [1], [41], tunnel junction or superlattice structure [1]. In addition, the injection can be further improved by the use of the current spreading layer or unique mask design. However, some complicated fabrication techniques such as e-beam lithography are associated with these methods, which make it difficult to accomplish. Recently, several groups directly deposited an ultra-thin metal layer as a current spreading layer to help the hole injection [23], [41]. Nevertheless, there is a trade-off between the hole injection and light absorption by the thin metal layer. Therefore, here we use microsphere lithography to form the current spreading layer (CSL) which can minimize the optical loss from the metal while maintaining the benefit in hole injection.

Figure 7.8 plots the fabrication process flow. After rinsing the samples with acetone, isopropyl alcohol (IPA) and deionized (DI) water, 1-2 µm AZ MiR 701 positive photoresist is spin-coated on the samples with the spin speed of 3000 rpm and follow by a soft-bake at 90 ℃ for 1min and 100 ℃ for another minute. Karl Suss MA56 contact aligner with broad band mercury lamp is used to form the mesa pattern. After developing in CD-26 for 1 min, the sample is baked at 140 ℃ for 5min. A Plasmatherm Inductively Coupled Plasma (ICP) with chlorine-based gases is used to etch III-nitride materials with a etch rate of 450 nm/min. Specifically, gases composed of 40 standard cubic centimeter per minute (sccm) of Cl_2, and 10 sccm Ar flow into the chamber with RF/ICP power of 500W/100 W and a chamber pressure of 5 mTorr to enable a smooth etch. The photoresist left on the sample is then removed by NMP-1-Methyl-2-pyrrolidinone (NMP) and the sample is ready for second layer lithography.

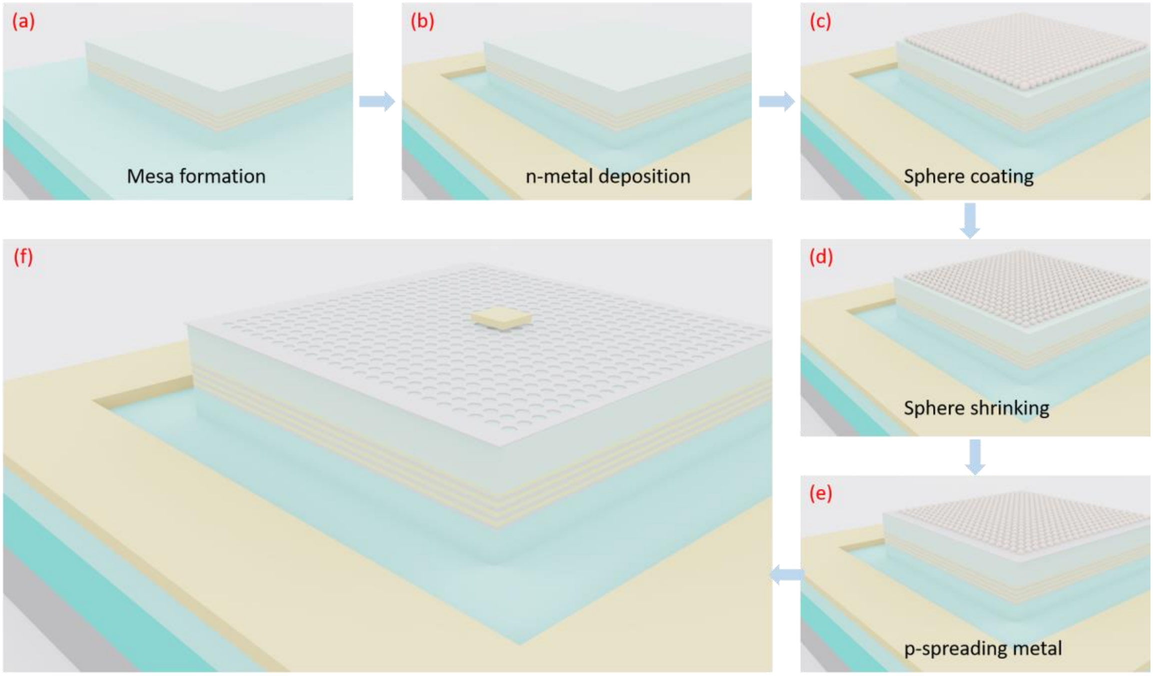

***Figure 7.8**: Fabrication process flow of sphere current spreading LEDs.*

The n-contact pattern is achieved by the standard lithography process with the use of LOR-5A liftoff resist and AZ MiR 701 resist. After the patterning, the sample is then loaded into a thermal evaporator for the Ti/Al/Ni/Ag (14/140/30/100 nm) metal deposition and lifted off by NMP.

To achieve nano-scale patterns, several techniques have been developed, such as Electron-beam lithography or direct write. However, the complexity of the processes and the high equipment cost make the techniques are unfavorable for many researchers. Instead, the use of low-cost nanosphere lithography (self-assembled nanosphere arrays) can also achieve large-scale nano-scale patterns. In this study, we use the self-assembled monolayers of spheres, typically made of polystyrene. The diameter of individual sphere is 385 nm. For the experiments, O_2 surface treatment is required prior to spin-coating nano-spheres on the device. Upon drying, a hexagonal-close-packed (HCP) monolayer spheres is formed. Then the sample is loaded into an oxygen-based plasma etcher to shrink the sphere size. An ultra-thin 20-nm Ni layer is deposited on the sample by the use of electron-beam (E-beam) evaporator. After the metal liftoff, the sphere spreading p-metal is formed, as shown in figure 7.9. The last step is the p-contact pad formation, which consist of a 50 -nm Ni layer.

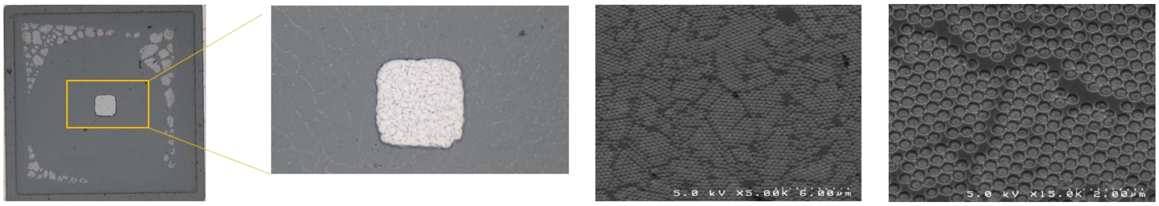

Figure 7.9: *SEM images of sphere current spreading LEDs.*

The transmission properties from this sphere CSL are investigated and shown in figure 7.10 (a). Compare to the 50-nm silver continuous film, the sphere CSL with same thickness shows much better transparency after the sphere liftoff. The transmissibility of the sphere CSL with different metal thicknesses are examined and plotted, showing good transparency in a wavelength range of 300 nm to 500 nm, which indicates the light extraction efficiency is not strongly reduced by using the sphere CSL.

Prior to utilize this technique on the UV LEDs, we first verified the effects in visible range, i.e. on green LEDs. Figure 7.10 (b) shows the EL spectrum from the green LEDs with and without the sphere CSL. Although the light extraction efficiency is slightly reduced due to the thin metal layer, the device with CSL presents a 50%

enhancement in EL intensity as compared to the conventional LEDs, which is attributed to the much better carrier injection.

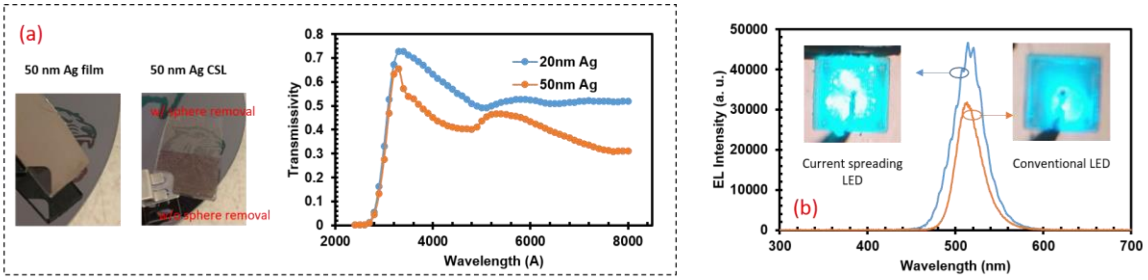

Figure 7.10: *(a) Photos of the glass slides with silver continuous film or sphere CSL, transmissivity of the glass slides with 20-nm and 50-nm sphere CSL at normal incident. (b) EL intensity from the green LEDs with and without sphere CSL.*

The preliminary data shows the promising results by the use of sphere CSL on green LEDs. However, there are many remaining experiments need to be done to examine the sphere CSL LEDs, i.e. the electric properties from the device, transmissivity from the device with different Ni film thicknesses, the use of CSL layer on UV LEDs. In addition, the sphere CSL layer could be used as a hard mask to form the photonics crystals or increase device surface roughness, which can further improve device light extraction efficiency.

7.4 III-Nitride Top-Down Nanowire LEDs

Another application of the nanosphere lithography is to fabricate III-nitride nanowires. Previous studies have reported promising performances from nanowire-based power and optoelectronic devices due to the low defects density, large surface-to-volume ratios and two-dimensional carrier confinement from the nanowire structures [8]. Instead of bottom-up nanowire growth, which is a complex and expensive process, this study developed a top-down nanowire fabrication. Specifically, a monolayer of silica spheres is coated on the device surface and shrank by fluorine-based dry etch. The sphere shrinking process is employed to open up the space between the adjacent spheres, which could minimize the nanowire bridging effect. The nanowires are then formed by a chlorine-based dry etch. Although by adjusting the etching conditions, such as chamber pressure, RF power, gases flow rate, the nanowire geometry and etch rate can be engineered, as shown in figure 7.11, the yield and uniformity of the sphere coating still need to be optimized. Alternatively, we developed another method to generate uniform pattern array by using Heiderburg laser writer with a resolution down to 0.8 μm.

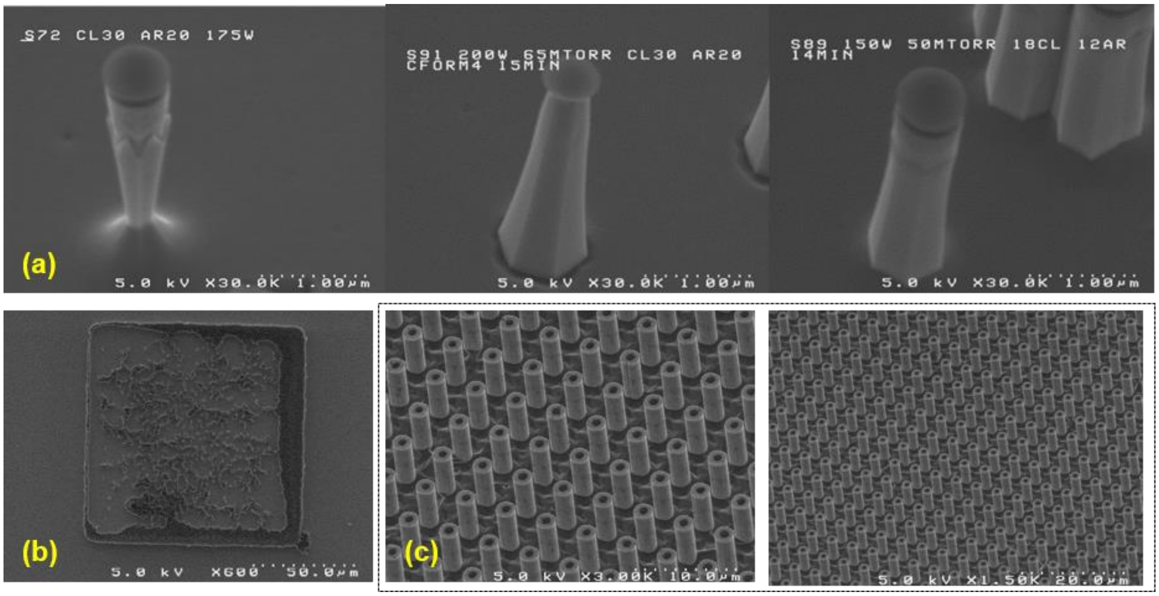

Figure 7.11*: (a) SEM images of GaN nanowires with different geometry (b) SEM image of nanowire LED by using nanosphere lithography showing nonuniform coating. (c) SEM image of nanowire green LED by using Heiderburg laser writer*

Figure 7.12 plots the nanowire LED fabrication process flow. After the chlorine-based dry etch, the nanowire sample was dipped into an AZ 400K KOH-based solution under 80 ℃ to smooth the side wall surface of the nanowire and shrink the diameter of the nanowire. The mechanism of the wet etch on GaN nanowire is presented in *Ref.*[42]. After the n-metal deposition, the sample is coated with a 7-µm-thick PDMS layer, which is further etched back to just expose the tip of the nanowire by fluorine-based dry etch. The purpose of this PDMS layer is to fill out and planarize the device, getting ready for p-metal contact deposition. To have a better light extraction efficiency from the nanowire LED, p-contact here consist of an ultra-thin (10-nm) Ni current spreading layer and a square thick (50-nm) Ni contact pad.

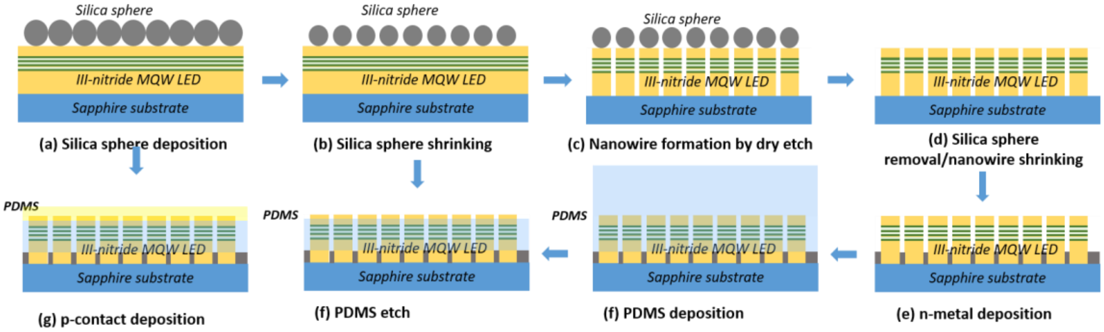

***Figure 7.12**: Process flow of nanowire LED fabrication*

This work has already developed a process flow to fabricate the nanowire LEDs and verified by using GaN wafers. The future work is applying the technique on DUV LEDs. The light radiation patterns and light intensities will be characterized and compared with the conventional planar devices with same mesa size. The influence of pitch size and nanowire diameter will be investigated as well.

Reference for Chapter 7:

[1] M. Kneissl and J. Rass, *III-Nitride Ultraviolet Emitters*, 227. Springer International Publishing Cham, 2016.

[2] S. I. Inoue, T. Naoki, T. Kinoshita, T. Obata, and H. Yanagi, "Light extraction enhancement of 265 nm deep-ultraviolet light-emitting diodes with over 90 mW output power via an AlN hybrid nanostructure," *Appl. Phys. Lett.*, 106, 131104, 2015.

[3] A. Armstrong and S. Rajan, "Enhanced Light Extraction in Tunnel Junction Enabled Top Emitting UV LEDs Yuewei Zhang," 052102, 1011, 10–13, 1882.

[4] T. Takano, T. Mino, J. Sakai, N. Noguchi, K. Tsubaki, and H. Hirayama, "Deep-ultraviolet light-emitting diodes with external quantum efficiency higher than 20% at 275 nm achieved by improving light-extraction efficiency," *Appl. Phys. Express*, 10, 031002, 2017.

[5] M. Jo, N. Maeda, and H. Hirayama, "Enhanced light extraction in 260 nm light-emitting diode with a highly transparent p-AlGaN layer," *Appl. Phys. Express*, 9, 012102, 2016.

[6] M. Jo, N. Maeda, and H. Hirayama, "Enhanced light extraction in 260 nm light-emitting diode with a highly transparent p-AlGaN layer," *Appl. Phys. Express*, 9, 1, 012102, 2016.

[7] T.-Y. Seong, H. Jung, H. Amano, and H. Morkoc, *III-Nitride Based Light Emitting*

Diodes and Applications, (2nd Ed.)., 133. Dordrecht: Springer Netherlands, 2017.

[8] Y. K. Ooi, C. Liu, and J. Zhang, “Analysis of Polarization-Dependent Light Extraction and Effect of Passivation Layer for 230-nm AlGaN Nanowire Light-Emitting Diodes,” *IEEE Photonics J.*, 9, 4501712, 2017.

[9] P. Zhu, G. Liu, J. Zhang, and N. Tansu, “FDTD analysis on extraction efficiency of GaN light-emitting diodes with microsphere arrays,” *IEEE/OSA J. Disp. Technol.*, 9, 5, 317–323, 2013.

[10] P. Zhu and N. Tansu, “Effect of packing density and packing geometry on light extraction of III-nitride light-emitting diodes with microsphere arrays,” 3, 4, 184–191, 2015.

[11] X. H. Li, R. Song, Y. K. Ee, P. Kumnorkaew, J. F. Gilchrist, and N. Tansu, “Light extraction efficiency and radiation patterns of III-nitride light-emitting diodes with colloidal microlens arrays with various aspect ratios,” *IEEE Photonics J.*, 3, 3, 489–499, 2011.

[12] Y.-K. Ee, R. A. Arif, N. Tansu, P. Kumnorkaew, and J. F. Gilchrist, “Enhancement of light extraction efficiency of InGaN quantum wells light emitting diodes using SiO2/polystyrene microlens arrays,” *Appl. Phys. Lett.*, 91, 221107, 2007.

[13] Y. K. Ee *et al.*, “Optimization of light extraction efficiency of III-nitride LEDs with self-assembled colloidal-based microlenses,” *IEEE J. Sel. Top. Quantum Electron.*, 15, 4, 1218, 2009.

[14] Y. K. Ooi and J. Zhang, “Light Extraction Efficiency Analysis of Flip-Chip Ultraviolet Light-Emitting Diodes With Patterned Sapphire Substrate,” *IEEE Photonics J.*, 10, 4, 2018.

[15] M. A. Würtele *et al.*, “Application of GaN-based ultraviolet-C light emitting diodes - UV LEDs - for water disinfection,” *Water Res.*, 45, 3, 1481, 2011.

[16] S. Vilhunen, H. Särkkä, and M. Sillanpää, “Ultraviolet light-emitting diodes in water disinfection,” *Environ. Sci. Pollut. Res.*, 16, 4, 439, 2009.

[17] J. Hodgkinson and R. P. Tatam, “Optical gas sensing: A review,” *Meas. Sci. Technol.*, 24, 1, 2013.

[18] Z. Xu and B. M. Sadler, “Ultraviolet communications: Potential and state-of-the-art,” *IEEE Commun. Mag.*, 46, 5, 67, 2008.

[19] H. Hirayama, N. Maeda, and M. Jo, “Recent Progress and Future Prospects of AlGaN Deep-UV LEDs,” *Jpn. J. Appl. Phys.*, 53, 100209, 2014.

[20] M. Kneissl *et al.*, “Advances in group III-nitride-based deep UV light-emitting diode technology,” *Semicond. Sci. Technol.*, 26, 014036, 2011.

[21] H. Hirayama, T. Yatabe, N. Noguchi, T. Ohashi, and N. Kamata, “231-261 nm AlGaN deep-ultraviolet light-emitting diodes fabricated on AlN multilayer buffers grown by ammonia pulse-flow method on sapphire,” *Appl. Phys. Lett.*, 91, 071901, 2007.

[22] J. Verma, P. K. Kandaswamy, V. Protasenko, A. Verma, H. Grace Xing, and D.

Jena, "Tunnel-injection GaN quantum dot ultraviolet light-emitting diodes," *Appl. Phys. Lett.*, 102, 041103, 2013.

[23] S. M. Islam *et al.*, "MBE-grown 232-270 nm deep-UV LEDs using monolayer thin binary GaN/AlN quantum heterostructures," *Appl. Phys. Lett.*, 110, 041108, 2017.

[24] Y. Taniyasu and M. Kasu, "Polarization property of deep-ultraviolet light emission from C-plane AlN/GaN short-period superlattices," *Appl. Phys. Lett.*, 99, 251112, 2011.

[25] J. Zhang, H. Zhao, and N. Tansu, "Effect of crystal-field split-off hole and heavy-hole bands crossover on gain characteristics of high Al-content AlGaN quantum well lasers," *Appl. Phys. Lett.*, 97, 111105, 2010.

[26] J. Zhang, H. Zhao, and N. Tansu, "Large optical gain AlGaN-delta-GaN quantum wells laser active regions in mid- and deep-ultraviolet spectral regimes," *Appl. Phys. Lett.*, 98, 171111, 2011.

[27] C. Liu *et al.*, "Physics and polarization characteristics of 298 nm AlN-delta-GaN quantum well ultraviolet light-emitting diodes," *Appl. Phys. Lett.*, 110, 071103, 2017.

[28] C. Liu, Y. K. Ooi, S. M. Islam, H. G. Xing, D. Jena, and J. Zhang, "234 nm and 246 nm AlN-Delta-GaN quantum well deep ultraviolet light-emitting diodes," *Appl. Phys. Lett.*, 112, 011101, 2018.

[29] C. Liu, Y. K. Ooi, and J. Zhang, "Proposal and physics of AlInN-delta-GaN

quantum well ultraviolet lasers," *J. Appl. Phys.*, 119, 8, 21–25, 2016.

[30] M. Gladysiewicz, M. Rudzinski, D. Hommel, and R. Kudrawiec, "Emission and material gain spectra of polar compressive strained AlGaN quantum wells grown on virtual AlGaN substrates: Tuning emission wavelength and mixing TE and TM mode of light polarization," *Semicond. Sci. Technol.*, 33, 075003, 2018.

[31] S. V. Novikov *et al.*, "Wurtzite Alxga1-xN bulk crystals grown by molecular beam epitaxy," *J. Cryst. Growth*, 322, 23–26, 2011.

[32] S. V. Novikov, C. R. Staddon, S. L. Sahonta, R. A. Oliver, C. J. Humphreys, and C. T. Foxon, "Growth of free-standing bulk wurtzite AlxGa1−xN layers by molecular beam epitaxy using a highly efficient RF plasma source," *J. Cryst. Growth*, 456, 151–154, 2016.

[33] S. V. Novikov, A. J. Kent, and C. T. Foxon, "Molecular beam epitaxy as a growth technique for achieving free-standing zinc-blende GaN and wurtzite AlxGa1-xN," *Prog. Cryst. Growth Charact. Mater.*, 63, 25–39, 2017.

[34] H. Zhao, R. A. Arif, Y. K. Ee, and N. Tansu, "Self-consistent analysis of strain-compensated InGaN-AlGaN quantum wells for lasers and light-emitting diodes," *IEEE J. Quantum Electron.*, 45, 1, 66, 2009.

[35] S. Chuang and C. Chang, "k·p method for strained wurtzite semiconductors," *Phys. Rev. B - Condens. Matter Mater. Phys.*, 54, 4, 2491, 1996.

[36] S. L. Chuang and C. S. Chang, "A band-structure model of strained quantum-well

wurtzite semiconductors," *Semicond. Sci. Technol.*, 12, 3, 252, 1997.

[37] S. L. Chuang, *Physics of photonic devices*. John Wiley & Sons, 2009.

[38] H. Zhao, G. Liu, R. A. Arif, and N. Tansu, "Current injection efficiency induced efficiency-droop in InGaN quantum well light-emitting diodes," *Solid. State. Electron.*, 54, 10, 1119–1124, 2010.

[39] J. Hader *et al.*, "On the importance of radiative and Auger losses in GaN-based quantum wells," *Appl. Phys. Lett.*, 92, 261103, 2008.

[40] C. Liu and J. Zhang, "Influence of quantum well design on light polarization switching in AlGaN ultraviolet emitters," *AIP Adv.*, 8, 085125, 2018.

[41] J. Verma, S. M. Islam, V. Protasenko, P. Kumar Kandaswamy, H. Xing, and D. Jena, "Tunnel-injection quantum dot deep-ultraviolet light-emitting diodes with polarization-induced doping in III-nitride heterostructures," *Appl. Phys. Lett.*, 104, 021105, 2014.

[42] M. Hartensveld, G. Ouin, C. Liu, and J. Zhang, "Effect of KOH passivation for top-down fabricated InGaN nanowire light emitting diodes," *J. Appl. Phys.*, 126, 18, 2019.

CHAPTER 8: Future Work

The influences of optical polarization on device efficiencies from conventional AlGaN QW heterostructure are discussed in this work. Specifically, it is really difficult to realize large TE-polarized $\boldsymbol{R_{sp}}$ in DUV regime while large TM-polarized $\boldsymbol{R_{sp}}$ can be noticed at short emission wavelength regime. However, the light extraction efficiency for TM-polarized photon (< 2%) is much smaller than that for TE-polarized photons. There are several ways to engineer the optical polarization properties from the AlGaN QWs, as discussed in this work. Strain effect, quantum confinement (QW thickness for example) are determinants for the optical polarization switching at which total number of TE-polarized photons equal to that of TM-polarized photons.

The target for the active region is to design a structure with large TE-polarized $\boldsymbol{R_{sp}}$. We proposed and investigated the use of AlGaN-delta-GaN and AlInN-delta-GaN QWs structures. There are three benefits of these designs: 1. Improve electron-hole wave function overlap; 2. Rearrange valence band ordering; 3. Engineer the emission wavelength by changing the delta-GaN thickness. The proposed structure can largely improve device internal quantum efficiency from 17% by using conventional AlGaN QW to > 75%.

To verify the ultra-thin GaN formation, as well as the dominant TE-polarized emission, we investigated AlN-delta-GaN QW UV LEDs in this work. 234 nm, 246 nm and 298 nm UV LEDs were carried out for this study. A polarization-dependent electroluminescence measurements setup is built to study the polarization properties. The results indicate the AlN-delta-GaN have promising properties as theoretical work predicted.

After the success of the AlN-delta-GaN structure, the AlGaN-delta-GaN epitaxy is developed in this work. A 255 nm UV emission with large IQE up to 85% is realized from the MBE-grown AlGaN-delta-GaN quantum well heterostructure, which confirms the delta-QW design is promising for the future of the DUV applications.

For the full LED structure, we also proposed a top-down nanowire structure and a current spreading LED to further improve device efficiency. The fabrication processes have been well-developed.

Although exciting results have been realized, there are still a lot of room for future improvement. The future work summarized below will focus on the remaining projects, such as the AlGaN-delta-GaN epitaxy, top-down nanowire LED and current spreading LEDs.

8.1 AlGaN-delta-GaN QW UV LEDs Epitaxy

As mentioned in chapter 6, the $Al_{0.9}Ga_{0.1}N$-delta-GaN QW heterostructure with 2-ML GaN have been successfully grown by MBE. A comprehensive study on the AlGaN-delta-GaN QW should be pursued. Theoretical studies have already predicted the thickness of the delta-GaN layer determines QW emission wavelength, which has already been demonstrated for the AlN-delta-GaN structure. The QW structures with different delta-GaN thicknesses and different Al-contents will be grown.

Although the $Al_{0.9}Ga_{0.1}N$-delta-GaN QW heterostructure has already shown up to 85% internal quantum efficiency, there are still a lot of unconquered territories in this work. For example, the IQE in this work is estimated by the I_{300K}/I_{4K} by assuming the 100% IQE at low temperature. This might not be 100% correct for the heterostructures especially considering roughness phonon scattering. Besides, the ABC values need to be extracted out by using both temperature-dependent PL and time-resolved PL measurements for future study.

Besides, the AlGaN-delta-GaN full LED structure will be epitaxially realized and compared to the conventional AlGaN QW LEDs. The polarization properties will be examined after the LED fabrications. It will be super helpful if multiple LEDs are fabricated for different emission wavelength with optical polarization properties examined.

8.2 Top-Down Nanowire DUV LEDs

Nanowire structure has been theoretically predicted to be effective to improve device light extraction efficiency. In this work, we developed a top-down nanowire fabrication process flow and demonstrated this method on several power devices. In this process, KOH-based chemical was critical to remove the dry-etch-damage, get vertical nanowire, shrink nanowire diameter for an InGaN-based blue or green LEDs. However, different profiles are realized on AlGaN-based DUV LEDs. Figure 8.1 shows the SEM images from a DUV nanowire sample at different KOH etch time. Different to the InGaN-based LEDs, which KOH solution etch faster in $<1\bar{1}01>$ than $<1\bar{1}00>$, the AZ400K will attack device $<1\bar{1}00>$ and form an inverted pyramid shape. The mechanisms and physics for this phenomenon is currently under investigation.

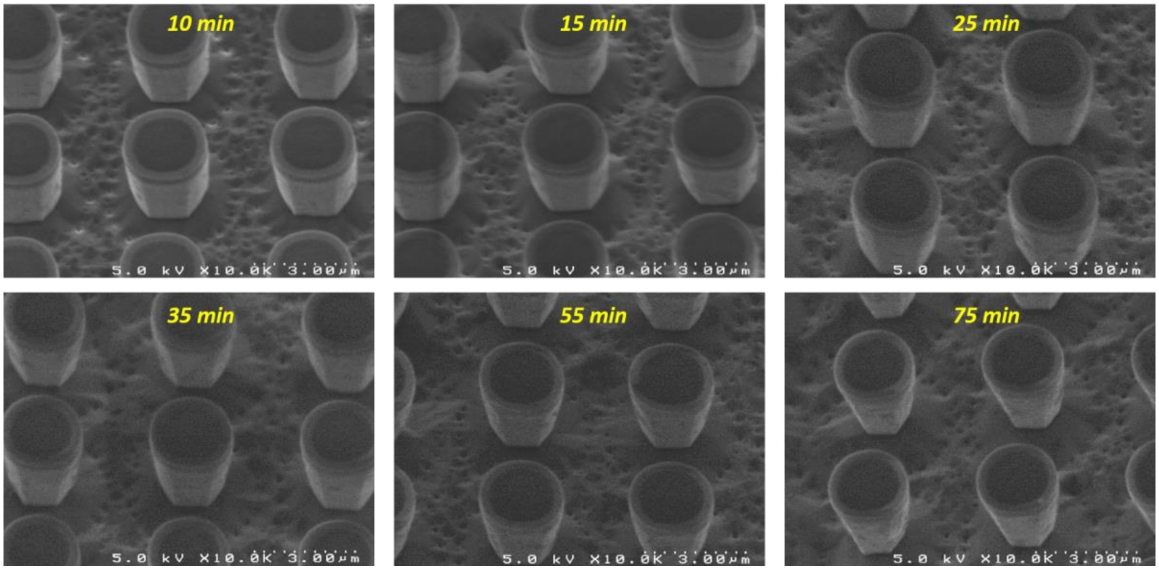

***Figure 8.1**: SEM images of AlGaN-based DUV LEDs after KOH wet etch at different times.*

Besides the wet etch, the use of PDMS is also critical to successfully fabricate the nanowire LEDs. PDMS was developed to fill out the nanowire spacing and isolate the p- and n-contact. However, during previous process, the PDMS coating and etch back process sometimes cause rough surface, which degrades device performance. New filling materials or improved process will be developed for future DUV nanowire LED fabrication. With all the process being developed, a full DUV nanowire LED will be fabricated and characterized.

8.3 Current Spreading DUV LEDs

Previous chapter describes a fabrication process to achieve sphere current spreading DUV LEDs, which has already been demonstrated on green LEDs. Future work would be focus on use this fabrication process on the DUV LEDs. More electrical properties and optical properties will be tested. Specifically, the transmission from the current spreading layer will be characterized and compared that from the thin film current spreading LEDs. For the IV test, there are three samples for comparison, one with sphere current spreading, one with thin film current spreading and one without current spreading. Furthermore, after the sphere current spreading layer formed, the layer can be used as a hard mask to have surface roughened, which is effective to further improve device light extraction efficiency.

APPENDIX A. Material Parameters for GaN and AlN

Parameters	GaN	AlN
a (Å) at $T = 300K$	3.189	3.112
c (Å) at $T = 300K$	5.185	4.982
E_g (eV) at $T = 300K$	3.44	6.00[a] / 6.16[b]
Δ_{cr} (eV)	0.010	-0.227[a] / -0.169[b]
Δ_{so} (eV)	0.017	0.036[a] / 0.019[b]
$m_e^{\parallel}/m_0$	0.21[a] / 0.20[b]	0.32
$m_e^{\perp}/m_0$	0.20	0.30
A_1	-7.21	-3.86
A_2	-0.44	-0.25
A_3	6.68	3.58
A_4	-3.46	-1.32
A_5	-3.40	-1.47
A_6	-4.90	-1.64
D_1 (eV)	-3.6[a] / -3.7[b]	-2.9[a] / -17.1[b]
D_2 (eV)	1.7[a] / 4.5[b]	4.9[a] / 7.9[b]
D_3 (eV)	5.2[a] / 8.2[b]	9.4[a] / 8.8[b]
D_4 (eV)	-2.7[a] / -4.1[b]	-4.0[a] / -3.9[b]
C_{11} (GPa)	390	396
C_{12} (GPa)	145	137
C_{13} (GPa)	106	108
C_{33} (GPa)	398	373
d_{13} (pm/V)	-1.0	-2.1
d_{33} (pm/V)	1.9	5.4

[a]: Parameters used for Chapter 2, 4-6 [1]

[b]: Parameters used for Chapter 3,7 [2]

Table A.1: Polarization and Bandgap of In$_x$Ga$_{1-x}$N, Al$_x$Ga$_{1-x}$N, and Al$_x$In$_{1-x}$N [2]

General Formula for Ternary Alloy Parameters ***P*** (Except Bandgap):

$$P(A_xB_{1-x}C) = xP(AC) + (1-x)P(BC)$$

Bandgap Energy

$$P(A_xB_{1-x}C) = xP(AC) + (1-x)P(BC) - bx(1-x)$$

$In_xGa_{1-x}N$

$$E_g(x) = xE_g(InN) + (1-x)E_g(GaN) - 1.4x(1-x)\ (eV)$$

$$P^{SP}(x) = [-0.042x - 0.034(1-x) + 0.037x(1-x)]\ (C/m^2)$$

$$P^{PZ}_{In_xGa_xN/InN}(x) = [-0.113(1-x) - 0.0276x(1-x)]\ (C/m^2)$$

$$P^{PZ}_{In_xGa_xN/GaN}(x) = [0.148x - 0.0424x(1-x)]\ (C/m^2)$$

$$P^{PZ}_{In_xGa_xN/AlN}(x) = [0.182x - 0.026(1-x) - 0.0456x(1-x)]\ (C/m^2)$$

$Al_xGa_{1-x}N$

$$E_g(x) = xE_g(AlN) + (1-x)E_g(GaN) - 0.7x(1-x)\ (eV)$$

$$P^{SP}(x) = [-0.090x - 0.034(1-x) + 0.021x(1-x)]\ (C/m^2)$$

$$P^{PZ}_{Al_xGa_xN/InN}(x) = [-0.28x - 0.113(1-x) + 0.42x(1-x)]\ (C/m^2)$$

$$P^{PZ}_{Al_xGa_xN/GaN}(x) = [-0.0525x + 0.0282x(1-x)]\ (C/m^2)$$

$$P^{PZ}_{Al_xGa_xN/InN}(x) = [0.026(1-x) - 0.0248x(1-x)]\ (C/m^2)$$

$Al_xIn_{1-x}N$

$$E_g(x) = xE_g(AlN) + (1-x)E_g(InN) - 2.5x(1-x)\ (eV)$$

$$P^{SP}(x) = [-0.090x - 0.042(1-x) + 0.070x(1-x)]\ (C/m^2)$$

$$P^{PZ}_{Al_xIn_xN/InN}(x) = [-0.28x + 0.104x(1-x)]\ (C/m^2)$$

$$P^{PZ}_{Al_xIn_xN/GaN}(x) = [-0.0525x + 0.148(1-x) + 0.938x(1-x)]\ (C/m^2)$$

$$P^{PZ}_{Al_xIn_xN/InN}(x) = [0.182(1-x) + 0.092x(1-x)]\ (C/m^2)$$

Reference for Appendix A

[1] H. Zhao, R. A. Arif, Y. K. Ee, and N. Tansu, “Self-consistent analysis of strain-compensated InGaN-AlGaN quantum wells for lasers and light-emitting diodes,” *IEEE J. Quantum Electron.*, 45, 1, 66, 2009.

[2] S. L. Chuang, *Physics of photonic devices*. John Wiley & Sons, 2012.

APPENDIX B: Numerical Simulation for Optical Properties of III-Nitride Quantum Wells

Wide band-gap III-nitride semiconductors such as GaN, AlN and InN and their ternary or quaternary alloys have attracted considerable attention due to their incredible potential in solid-state lightning throughout visible and ultraviolet regimes. Since these III-nitride alloys are stabilized in Wurtzite forms with direct bandgaps, the electronic and optical properties are strongly determined by the band structures near the Brillouin zone center. Therefore, the calculations of the semiconductor band structures including band energy lineup, wavefunction, and valence band structures are essential in order to provide a comprehensive understanding and useful guidance for optoelectronic devices. This appendix introduces a self-consistent 6-band ***k·p*** model for wurtzite III-nitride semiconductors to study the band edge profiles. Optical properties such as spontaneous emission rate and optical gain are also derived based on the band structure calculations and Fermi's Golden Rule. In addition, the numerical calculation details are also mentioned in this chapter.

B.1 *k·p* Method for Strained Wurtzite Semiconductors

In this study, the calculations of the band structures and electron and hole wavefunctions are based on a self-consistent 6-band ***k·p*** model with considering the strain effect, both piezoelectric polarization and spontaneous polarization, as well as the carrier screening effect. The six bands here correspond to the heavy hole (HH), light hole (LH) and crystal-field split-off (CH) bands, which have double degeneracy with considering spin counterparts. In addition, Kane's model is employed to determine the band-edge parameters and optical momentum-matrix element [1]–[5].

B.1.1 Kane's Model for Wurtzite Semiconductors

A. The Hamiltonian Matrix with spin-orbit Coupling

The Schrodinger equation for the periodic component of the Bloch function and the energy $E_n(\boldsymbol{k})$ near the band edge can be expressed as:

$$Hu_{\boldsymbol{nk}}(\boldsymbol{r}) = \left(H_0 + \frac{\hbar^2 k^2}{2m_0} + \frac{\hbar}{m_0} k \cdot p + H_{SO})\right) u_{\boldsymbol{nk}}(\boldsymbol{r}) = E_n(\boldsymbol{k}) u_{\boldsymbol{nk}}(\boldsymbol{r}) \qquad \text{B-1}$$

The total Hamiltonian near $k_0 = 0$ is:

$$H = H_0 + \frac{\hbar^2 k^2}{2m_0} + \frac{\hbar}{m_0} k \cdot p + H_{SO} \qquad \text{B-2}$$

where

$$H_0 = \frac{p^2}{2m_0} + V(\boldsymbol{r}) \qquad \text{B-3}$$

$$\nabla P = \nabla \cdot (P_{PZ} + P_{SP}) = -\rho_{pol} \qquad \text{B-4}$$

Here, H_{SO} is the spin-orbit interaction, ***V(r)*** accounts for the periodic potential, and σ is the Pauli spin matrix with three components:

$$\sigma_x = \begin{bmatrix} 0 & 1 \\ 1 & 0 \end{bmatrix} \quad \sigma_y = \begin{bmatrix} 0 & -i \\ i & 0 \end{bmatrix} \quad \sigma_z = \begin{bmatrix} 1 & 0 \\ 0 & -1 \end{bmatrix} \qquad \text{B-5}$$

and the spin operators are defined as:

$$\uparrow = \begin{bmatrix} 1 \\ 0 \end{bmatrix} \qquad \downarrow = \begin{bmatrix} 0 \\ 1 \end{bmatrix} \qquad \text{B-6}$$

The set of basis functions near the zone center are:

$$\begin{gathered}
|iS\uparrow\rangle\,, \quad u_1 = \left|-\frac{(X+iY)}{\sqrt{2}}\uparrow\right\rangle, \quad u_2 = \left|\frac{(X-iY)}{\sqrt{2}}\uparrow\right\rangle, \quad u_3 = |Z\uparrow\rangle \\
|iS\downarrow\rangle\,, \quad u_4 = \left|\frac{(X-iY)}{\sqrt{2}}\downarrow\right\rangle, \quad u_5 = \left|-\frac{(X+iY)}{\sqrt{2}}\downarrow\right\rangle, \quad u_6 = |Z\downarrow\rangle
\end{gathered} \tag{B-7}$$

Specifically, $|\boldsymbol{iS}\uparrow\rangle$ and $|\boldsymbol{iS}\downarrow\rangle$ are the basis functions for conduction band, and the rest are for valence band.

The Hamiltonian matrix can be written as:

$$H_{8\times 8} = \frac{\hbar^2 k^2}{2m_0} + \begin{bmatrix}
E_c & -\frac{k_+ p_2}{\sqrt{2}} & \frac{k_- p_2}{\sqrt{2}} & k_z p_1 & 0 & 0 & 0 & 0 \\
-\frac{k_- p_2}{\sqrt{2}} & E_v + \Delta_1 + \Delta_2 & 0 & 0 & 0 & 0 & 0 & 0 \\
\frac{k_+ p_2}{\sqrt{2}} & 0 & E_v + \Delta_1 - \Delta_2 & 0 & 0 & 0 & 0 & \sqrt{2}\Delta_3 \\
0 & 0 & 0 & E_v & 0 & 0 & \sqrt{2}\Delta_3 & 0 \\
0 & 0 & 0 & 0 & E_c & \frac{k_- p_2}{\sqrt{2}} & -\frac{k_+ p_2}{\sqrt{2}} & k_z p_1 \\
0 & 0 & 0 & 0 & \frac{k_+ p_2}{\sqrt{2}} & E_v + \Delta_1 + \Delta_2 & 0 & 0 \\
0 & 0 & 0 & \sqrt{2}\Delta_3 & -\frac{k_- p_2}{\sqrt{2}} & 0 & E_v + \Delta_1 - \Delta_2 & 0 \\
0 & 0 & \sqrt{2}\Delta_3 & 0 & k_z p_1 & 0 & 0 & E_v
\end{bmatrix} \tag{B-8}$$

where

$$k_\pm = k_x \pm i k_y \tag{B-9}$$

and the definitions for the energies are as shown below:

$$\begin{gathered}
\langle S|H_0|S\rangle = E_c \\
\langle X|H_0|X\rangle = \langle Y|H_0|Y\rangle = E_v + \Delta_1 \\
\langle Z|H_0|Z\rangle = E_v \\
\langle X|H_{SZ}|Y\rangle = -i\Delta_2
\end{gathered} \tag{B-10}$$

$$\langle Y|H_{SX}|Z\rangle = \langle Z|H_{SY}|X\rangle = -i\Delta_3$$

$\boldsymbol{P_1}$ and $\boldsymbol{P_2}$ are Kane’s parameters, which are related to the interband momentum-matrix elements, and defined as:

$$\left\langle iS\left|\frac{h}{i}\frac{\partial}{\partial z}\right|Z\right\rangle = \frac{m_0}{\hbar}P_1$$
$$\left\langle iS\left|\frac{h}{i}\frac{\partial}{\partial x}\right|X\right\rangle = \left\langle iS\left|\frac{h}{i}\frac{\partial}{\partial y}\right|Y\right\rangle = \frac{m_0}{\hbar}P_2 \qquad \text{B-11}$$

Not like the original Kane’s model for cubic crystal, all the three components of the $\boldsymbol{k}$ vector are considered for wurtzite structures. The sixfold symmetry on the ***x*-*y*** plane was used for the derivations of the matrix elements.

B. Band-edge energies and basis functions

At the zone center ($\boldsymbol{k_x} = \boldsymbol{k_y} = \boldsymbol{k_z} = 0$), we can get the band-edge energies and their corresponding basis functions from the eigenvalue and eigenvectors of the Hamiltonian matrix in (3-8):

$$\begin{array}{ccc}
E_c & |iS\uparrow\rangle & |iS\downarrow\rangle \\
E_1 = E_v + \Delta_1 + \Delta_2 & u_1 & u_4 \\
E_2 = E_v + \frac{\Delta_1-\Delta_2}{2} + \sqrt{\left(\frac{\Delta_1-\Delta_2}{2}\right)^2 + 2{\Delta_3}^2} & au_2 + bu_6 & bu_3 + au_5 \\
E_3 = E_v + \frac{\Delta_1-\Delta_2}{2} - \sqrt{\left(\frac{\Delta_1-\Delta_2}{2}\right)^2 + 2{\Delta_3}^2} & bu_2 - au_6 & -au_3 + bu_5
\end{array} \qquad \text{B-12}$$

where:

$$a = \frac{E_2}{\sqrt{{E_2}^2 + 2{\Delta_3}^2}} \qquad b = \frac{\sqrt{2}\Delta_3}{\sqrt{{E_2}^2 + 2{\Delta_3}^2}} \qquad \text{B-13}$$

For convenience, the reference energy is set at $E_v = 0$. The band-edge energies are described in figure B.1. Without the spin-orbit interaction ($\boldsymbol{\Delta_2} = \boldsymbol{\Delta_3} = 0$), we get $\boldsymbol{E_1} = \boldsymbol{E_2} = \boldsymbol{\Delta_1}$ while $\boldsymbol{E_3} = 0$. When taking into account the spin-orbit interaction effect, the nonvanishing $\Delta_2 = \Delta_3$ leads to an energy splitting, as shown in figure B.1 (b). Based on the cubic approximation, the energies $(\Delta_1, \Delta_2, \Delta_3)$ can relate with the crystal-field split energy, Δ_{cr}, and the spin-orbit split-off energy, Δ_{so}, by:

$$\Delta_1 = \Delta_{cr}, \qquad \Delta_2 = \Delta_3 = \frac{1}{3}\Delta_{so} \tag{B-14}$$

For GaN, $\Delta_1 > \Delta_2 > 0$, the three band energies from top to bottom can be labeled as HH, LH, and CH, respectively. While for AlN, Δ_1 has a negative value, which results in a different valence bands ordering: CH, LH, and HH. Note that the ordering of the valence band energies strongly determines the light polarization, which will be well-explained in Chapter 1.

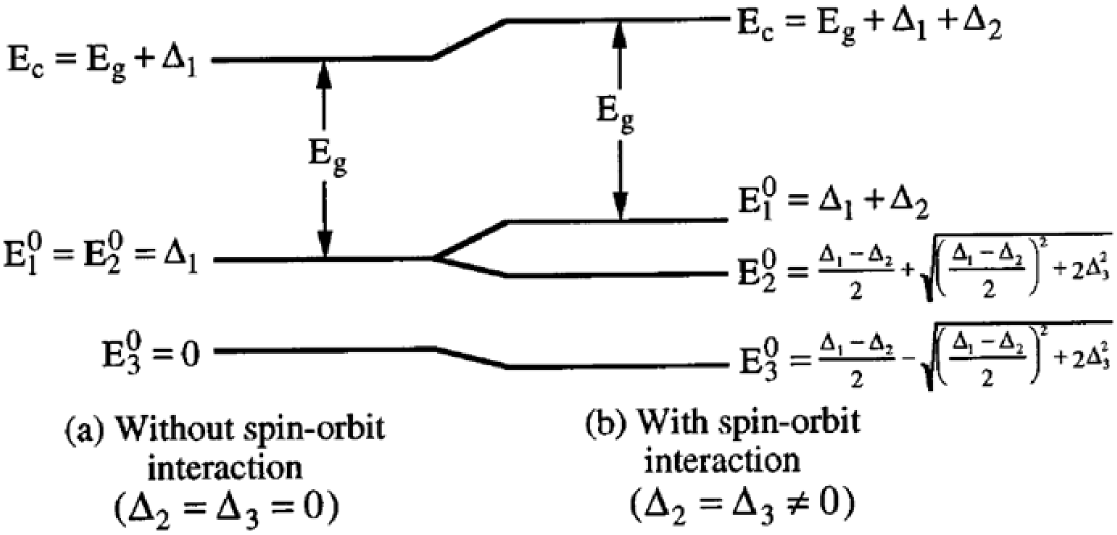

***Figure B.1**: The band-edge energies for wurtzite GaN (a) without spin-orbit interaction; (b) with spin-orbit interaction [2].*

B.1.2 ***k·p*** *Method for Strained Wurtzite Semiconductors*

Perturbation theory is widely used to study the coupling of the degenerate valence bands. For wurtzite semiconductors, an improved method called Lowdin's perturbation theory is used to provide the Hamiltonian to the second order in the ***k·p*** contributions.

A. General formulation

Using Lowdin's perturbation theory, the total Hamiltonian near $\boldsymbol{k_0} = 0$ from *Eq.* B-2 can be rewrite as:

$$H = H_0 + \frac{\hbar^2 k^2}{2m_0} + H' + H_{SO} \tag{B-15}$$

where:

$$H' = \frac{\hbar}{m_0} k \cdot \Pi, \qquad \Pi = p + \frac{\hbar}{4m_0 c^2} \sigma \times \nabla V \tag{B-16}$$

Therefore, the 6×6 Hamiltonian matrix for the valence bands can be written as a combination of a band-edge component and a ***k***-dependent contribution:

$$H_{6\times6,jj'}(\boldsymbol{k}) = H_{6\times6,jj'}(\boldsymbol{k} = 0) + D_{jj'} \tag{B-17}$$

where the k-dependent matrix is:

$$\begin{aligned} D_{jj'} &= \sum_{\alpha,\beta} D_{jj'}^{\alpha\beta}\, k_\alpha k_\beta \\ D_{jj'}^{\alpha\beta} &= \frac{\hbar^2}{2m_0}\left[\delta_{jj'}\delta_{\alpha\beta} + \sum_{\gamma}^{B} \frac{p_{j\gamma}^{\alpha} p_{\gamma j'}^{\beta} + p_{j\gamma}^{\beta} p_{\gamma j'}^{\alpha}}{m_0(E_0 - E_\gamma)}\right] \end{aligned} \tag{B-18}$$

It is noted that the six valence band wavefunctions in $Eq.$ B-7 are the bases for the interest and called class A, while the rest states of no interest are categorized as class B. For $Eq.$ B-18, $\boldsymbol{j}, \boldsymbol{j}' = 1,2 \ldots,6 \ \in A$, $\gamma \in B$, and $\boldsymbol{\alpha}, \boldsymbol{\beta} = x, y, z$. From Kane's model, the band-edge Hamiltonian matrix can be written as:

$$H_{6\times6}(\boldsymbol{k}=0) = \begin{bmatrix} E_v+\Delta_1+\Delta_2 & 0 & 0 & 0 & 0 & 0 \\ 0 & E_v+\Delta_1-\Delta_2 & 0 & 0 & 0 & \sqrt{2}\Delta_3 \\ 0 & 0 & E_v & 0 & \sqrt{2}\Delta_3 & 0 \\ 0 & 0 & 0 & E_v+\Delta_1+\Delta_2 & 0 & 0 \\ 0 & 0 & \sqrt{2}\Delta_3 & 0 & E_v+\Delta_1-\Delta_2 & 0 \\ 0 & \sqrt{2}\Delta_3 & 0 & 0 & 0 & E_v \end{bmatrix}$$

B-19

The D matrix can be obtained by the Luttinger-Kohn method:

$$D_{6\times6} = \begin{bmatrix} \begin{matrix} D_{11} & {D_{21}}^* & -{D_{23}}^* \\ D_{21} & D_{11} & D_{23} \\ -D_{23} & {D_{23}}^* & D_{ZZ} \end{matrix} & 0 \\ 0 & \begin{matrix} D_{11} & D_{21} & D_{23} \\ {D_{21}}^* & D_{11} & -{D_{23}}^* \\ {D_{23}}^* & -D_{23} & D_{ZZ} \end{matrix} \end{bmatrix} \qquad \text{B-20}$$

where:

$$\begin{aligned} D_{11} &= \left(\frac{L_1+M_1}{2}\right)\left({k_x}^2+{k_y}^2\right) \\ D_{ZZ} &= M_3\left({k_x}^2+{k_y}^2\right)+L_2{k_z}^2 \\ D_{21} &= -\frac{1}{2}\left[(L_1-M_1)\left({k_x}^2-{k_y}^2\right)+2iN_1k_xk_y\right] \\ &\qquad\qquad = -\frac{1}{2}(k_x+ik_y)^2 \\ D_{23} &= \frac{1}{\sqrt{2}}N_2\left(k_x+ik_y\right)k_z \\ L_1-M_1 &= N_1 \end{aligned} \qquad \text{B-21}$$

And we defined the band structure parameters as:

$$L_1 = \frac{\hbar^2}{2m_0}\left(1+\sum_{\gamma}^{B}\frac{2p^x_{X\gamma}p^x_{\gamma X}}{m_0(E_0-E_\gamma)}\right) = \frac{\hbar^2}{2m_0}\left(1+\sum_{\gamma}^{B}\frac{2p^y_{Y\gamma}p^y_{\gamma Y}}{m_0(E_0-E_\gamma)}\right) \qquad \text{B-22}$$

$$L_2 = \frac{\hbar^2}{2m_0}(1 + \sum_{\gamma}^{B} \frac{2p_{Z\gamma}^{z} p_{\gamma Z}^{z}}{m_0(E_0 - E_\gamma)})$$
$$M_1 = \frac{\hbar^2}{2m_0}(1 + \sum_{\gamma}^{B} \frac{2p_{X\gamma}^{y} p_{\gamma X}^{y}}{m_0(E_0 - E_\gamma)}) = \frac{\hbar^2}{2m_0}(1 + \sum_{\gamma}^{B} \frac{2p_{Y\gamma}^{x} p_{\gamma Y}^{x}}{m_0(E_0 - E_\gamma)})$$
$$M_2 = \frac{\hbar^2}{2m_0}(1 + \sum_{\gamma}^{B} \frac{2p_{X\gamma}^{z} p_{\gamma X}^{z}}{m_0(E_0 - E_\gamma)}) = \frac{\hbar^2}{2m_0}(1 + \sum_{\gamma}^{B} \frac{2p_{Y\gamma}^{z} p_{\gamma Y}^{z}}{m_0(E_0 - E_\gamma)})$$
$$M_3 = \frac{\hbar^2}{2m_0}(1 + \sum_{\gamma}^{B} \frac{2p_{Z\gamma}^{x} p_{\gamma Z}^{x}}{m_0(E_0 - E_\gamma)}) = \frac{\hbar^2}{2m_0}(1 + \sum_{\gamma}^{B} \frac{2p_{Z\gamma}^{y} p_{\gamma Z}^{y}}{m_0(E_0 - E_\gamma)})$$
$$N_1 = \frac{\hbar^2}{2m_0} \sum_{\gamma}^{B} \frac{p_{X\gamma}^{x} p_{\gamma Y}^{y} + p_{X\gamma}^{y} p_{\gamma Y}^{x}}{m_0(E_0 - E_\gamma)})$$
$$N_2 = \frac{\hbar^2}{2m_0} \sum_{\gamma}^{B} \frac{p_{X\gamma}^{x} p_{\gamma Z}^{z} + p_{X\gamma}^{z} p_{\gamma Z}^{x}}{m_0(E_0 - E_\gamma)}) = \frac{\hbar^2}{2m_0} \sum_{\gamma}^{B} \frac{p_{Y\gamma}^{y} p_{\gamma Z}^{z} + p_{Y\gamma}^{z} p_{\gamma Z}^{y}}{m_0(E_0 - E_\gamma)})$$

where $\boldsymbol{p_{X\gamma}^{y}} = \langle \boldsymbol{X} | \boldsymbol{p}^{\boldsymbol{y}} | \boldsymbol{\gamma} \rangle$, etc., and $\boldsymbol{p}^{\boldsymbol{y}} = (\hbar/\boldsymbol{i})(\boldsymbol{\partial}/\boldsymbol{\partial y})$ is the $\boldsymbol{y}$ component of the momentum operator. Therefore, the total Hamiltonian $H_{6\times 6}(\boldsymbol{k}) = H_{6\times 6}(\boldsymbol{k} = 0) + D_{jj'}$ can be written as:

$$H = \begin{bmatrix} F & -K^* & -H^* & 0 & 0 & 0 \\ -K & G & H & 0 & 0 & \Delta \\ -H & H^* & \lambda & 0 & \Delta & 0 \\ 0 & 0 & 0 & F & -K & H \\ 0 & 0 & \Delta & -K^* & G & -H^* \\ 0 & \Delta & 0 & H^* & -H & \lambda \end{bmatrix} \begin{matrix} |u_1\rangle \\ |u_2\rangle \\ |u_3\rangle \\ |u_4\rangle \\ |u_5\rangle \\ |u_6\rangle \end{matrix} \qquad \text{B-23}$$

where:

$$F = \Delta_1 + \Delta_2 + \lambda + \theta$$
$$G = \Delta_1 - \Delta_2 + \lambda + \theta$$
$$\lambda = \frac{\hbar^2}{2m_0}\left[A_1 {k_z}^2 + A_2({k_x}^2 + {k_y}^2)\right]$$
$$\theta = \frac{\hbar^2}{2m_0}\left[A_3 {k_z}^2 + A_4({k_x}^2 + {k_y}^2)\right]$$
$$K = \frac{\hbar^2}{2m_0} A_5 (k_x + ik_y)^2 \qquad \text{B-24}$$

$$H = \frac{\hbar^2}{2m_0} A_6 (k_x + ik_y) k_z$$
$$\Delta = \sqrt{2}\Delta_3$$

We relate the band structure parameters and the more commonly used $\boldsymbol{A_i}$ parameters as follow:

$$\frac{\hbar^2}{2m_0}A_1 = L_2, \qquad \frac{\hbar^2}{2m_0}A_2 = M_3, \qquad \frac{\hbar^2}{2m_0}A_3 = M_2 - L_2$$
$$\frac{\hbar^2}{2m_0}A_4 = \frac{L_1+M_1}{2} - M_3, \qquad \frac{\hbar^2}{2m_0}A_5 = \frac{N_1}{2}, \qquad \frac{\hbar^2}{2m_0}A_6 = \frac{N_2}{\sqrt{2}} \qquad \text{B-25}$$

*B. **k·p** method for strained wurtzite semiconductors*

For a strained-layer wurtzite semiconductor pseudomorphically grown along the (0001) ($\boldsymbol{z}$-axis) direction, the strain tensor is expressed as:

$$\varepsilon_{xx} = \varepsilon_{yy} = \frac{a_0 - a}{a}$$
$$\varepsilon_{zz} = -\frac{2C_{13}}{C_{33}}\varepsilon_{xx} \qquad \text{B-26}$$
$$\varepsilon_{xy} = \varepsilon_{yz} = \varepsilon_{zx} = 0$$

where $\boldsymbol{a_0}$ and a are the lattice constants of the substrate and the epitaxial layer material, $\boldsymbol{C_{13}}$ and $\boldsymbol{C_{33}}$ are the elastic stiffness constants.

When the lattice constant of the layer material a is smaller than that of the substrate a_0, it is named as the tensile strain with a positive $\boldsymbol{\varepsilon_{xx}}$ ($\boldsymbol{\varepsilon_{yy}}$). However, for the case $\boldsymbol{a} > \boldsymbol{a_0}$, it is called compressive strain with a negative $\boldsymbol{\varepsilon_{xx}}$ ($\boldsymbol{\varepsilon_{yy}}$).

Taking into consideration the strain effect, the 6×6 Hamiltonian matrix in *Eq.* B-23 can be expressed as following:

$$H = \begin{bmatrix} F & K_t & -iH_t & 0 & 0 & 0 \\ K_t & G & \Delta - iH_t & 0 & 0 & \Delta \\ iH_t & \Delta + iH_t & \lambda & 0 & \Delta & 0 \\ 0 & 0 & 0 & F & K_t & iH_t \\ 0 & 0 & \Delta & K_t & G & \Delta + iH_t \\ 0 & \Delta & 0 & -iH_t & \Delta - iH_t & \lambda \end{bmatrix} \qquad \text{B-27}$$

where:

$$\begin{aligned} F &= \Delta_1 + \Delta_2 + \lambda + \theta \\ G &= \Delta_1 - \Delta_2 + \lambda + \theta \\ \lambda &= \frac{\hbar^2}{2m_0}\left[A_1 {k_z}^2 + A_2 {k_t}^2\right] + D_1\varepsilon_{zz} + D_2\left(\varepsilon_{xx} + \varepsilon_{yy}\right) \\ \theta &= \frac{\hbar^2}{2m_0}\left[A_3 {k_z}^2 + A_4 {k_t}^2\right] + D_3\varepsilon_{zz} + D_4\left(\varepsilon_{xx} + \varepsilon_{yy}\right) \\ K_t &= \frac{\hbar^2}{2m_0} A_5 {k_t}^2 \\ H_t &= \frac{\hbar^2}{2m_0} A_6 k_t k_z \\ \Delta &= \sqrt{2}\Delta_3 \end{aligned} \qquad \text{B-28}$$

Therefore, the valence band-edge energies in *Eq*. B-12 can be adjusted as:

$$\begin{aligned} E_1 &= E_v + \Delta_1 + \Delta_2 + \theta_\epsilon + \lambda_\epsilon \\ E_2 &= E_v + \frac{\Delta_1 - \Delta_2 + \theta_\epsilon}{2} + \lambda_\epsilon + \sqrt{\left(\frac{\Delta_1 - \Delta_2 + \theta_\epsilon}{2}\right)^2 + 2{\Delta_3}^2} \\ E_3 &= E_v + \frac{\Delta_1 - \Delta_2 + \theta_\epsilon}{2} + \lambda_\epsilon - \sqrt{\left(\frac{\Delta_1 - \Delta_2 + \theta_\epsilon}{2}\right)^2 + 2{\Delta_3}^2} \end{aligned} \qquad \text{B-29}$$

while the conduction band edge has a hydrostatic energy shift:

$$P_{c\epsilon} = a_{cz}\varepsilon_{zz} + a_{ct}(\varepsilon_{xx} + \varepsilon_{yy}) \qquad \text{B-30}$$

C. Effective-mass equations in a strained quantum well

For strained wurtzite structures, the conduction band can be characterized by a parabolic model, and the effective-mass Schrodinger equation can be expressed as:

$$H^c(k_t, k_z) = \left(\frac{\hbar^2}{2}\right)\left(\frac{{k_t}^2}{m_e^t} + \frac{{k_z}^2}{m_e^z}\right) + V_e(z) + P_{c\epsilon} \qquad \text{B-31}$$

where $\boldsymbol{m_e^t}$ and $\boldsymbol{m_e^z}$ are the electron effective masses perpendicular ($\boldsymbol{t}$) and parallel ($\boldsymbol{z}$) to the growth direction. The wavevectors are given as $k_t = -i\nabla_t$ and $k_z = -\partial/\partial z$. $\boldsymbol{P_{c\epsilon}}$ is the strain-related factor in the quantum well region and is assumed to be 0 in the barriers. $\boldsymbol{V_e(z)}$ is the potential energy of the unstrained conduction-band edge $V_e(z) = E_c^0$. The electron wavefunction of the $\boldsymbol{n_{th}}$ conduction subband can be written as:

$$\psi_{n,k_t}^{c\eta}(z) = \frac{e^{-ik_t r_t}}{\sqrt{A}}\phi_n(z)|S,\eta\rangle \qquad \text{B-32}$$

where $\boldsymbol{r_t}$ is the two-dimensional position vector and $\boldsymbol{A}$ is the quantum well area in the $\boldsymbol{x}$-$\boldsymbol{y}$ plane. $\boldsymbol{\phi_n}$ is the envelop wavefunction of the $\boldsymbol{n_{th}}$ conduction subband and $\boldsymbol{\eta}$ is the electron spin (↑ and ↓).

The conduction band-edge energy $\boldsymbol{E_n^c = E_n^c(k_t = 0)}$ can be obtained by solving the effective-mass equation for electrons:

$$H^c(k_t = 0, k_z = -i\partial/\partial z)\phi_n(z) = E_n^c\phi_n(z) \qquad \text{B-33}$$

The envelop wavefunction is normalized as:

$$\int dz|\phi_n(z)|^2 = 1 \quad \text{B-34}$$

Then we can obtain the conduction band structure by using:

$$E_n^c(k_t) \approx E_n^c(k_t = 0) + \frac{\hbar^2 {k_t}^2}{2m_{e,w}^t} \quad \text{B-35}$$

where $\boldsymbol{m_{e,w}^t}$ is the electron effective mass in the well region perpendicular to the growth direction.

For the bulk valence band structure, it can be obtained by finding the eigenvalues of:

$$\det\left[H_{i,j}^v(k) - \delta_{i,j}E^v(k)\right] = 0 \quad \text{B-36}$$

And the 6×6 Hamiltonian can be expressed as:

$$H_{6\times 6}^v(k) = \begin{bmatrix} H_{3\times 3}^U(k) & 0 \\ 0 & H_{3\times 3}^L(k) \end{bmatrix} \quad \text{B-37}$$

where upper $H_{3\times 3}^U(k)$ and lower $H_{3\times 3}^L(k)$ are matrices defined as:

$$H^U = \begin{bmatrix} F & K_t & -iH_t \\ K_t & G & \Delta - iH_t \\ iH_t & \Delta + iH_t & \lambda \end{bmatrix}$$

$$H^L = \begin{bmatrix} F & K_t & iH_t \\ K_t & G & \Delta + iH_t \\ -iH_t & \Delta - iH_t & \lambda \end{bmatrix} \quad \text{B-38}$$

The hole wavefunction can be written as:

$$\Psi_m^U(z; k_t) = \frac{e^{ik_t r_t}}{\sqrt{A}} \left(g_m^{(1)}(z; k_t)|1\rangle + g_m^{(2)}(z; k_t)|2\rangle + g_m^{(3)}(z; k_t)|3\rangle\right) \quad \text{B-39}$$

$$\Psi_m^L(z;k_t) = \frac{e^{ik_t r_t}}{\sqrt{A}}\left(g_m^{(4)}(z;k_t)|4\rangle + g_m^{(5)}(z;k_t)|5\rangle + g_m^{(6)}(z;k_t)|6\rangle\right)$$

where $g_m^{(i)}$, $i = 1,2,3,4,5,6$ are the envelope functions of the $\boldsymbol{m_{th}}$ valence subbands, which follow the normalization:

$$\begin{aligned} \sum_{i=1}^{3}\int dz\left|g_m^{(i)}(z;k_t)\right|^2 = 1 \\ \sum_{i=4}^{6}\int dz\left|g_m^{(i)}(z;k_t)\right|^2 = 1 \end{aligned} \qquad \text{B-40}$$

The valence subband structure for the upper Hamiltonian can be achieved by solving:

$$\sum_{j=1}^{3}[H_{ij}^U\left(k_z = -i\frac{\partial}{\partial z}\right) + \delta_{i,j}E_v^0(z)]g_m^{(j)}(z;k_t) = E_m^U(k_t)g_m^{(i)}(z;k_t) \qquad \text{B-41}$$

Similarly, the band structure for the lower Hamiltonian can be obtained by the same method. Note that there is only a change of signs in front of all the terms with a single derivative with respect to $\boldsymbol{z}$ for $\boldsymbol{H^U}$ and $\boldsymbol{H^L}$. Therefore, the valence band structures for a quantum well satisfy $E_v^0(z) = E_v^0(-z)$ and $E_m^U(k_t) = E_m^L(k_t)$. The wavefunctions are related as:

$$\begin{aligned} g_m^{(1)}(z;k_t) = g_m^{(4)}(-z;k_t) \\ g_m^{(2)}(z;k_t) = g_m^{(5)}(-z;k_t) \\ g_m^{(3)}(z;k_t) = g_m^{(6)}(-z;k_t) \end{aligned} \qquad \text{B42}$$

The order of the HH, LH and CH subbands is determined by the wavefunctions at the band edge ($\boldsymbol{k_t} = 0$). If $\boldsymbol{g_m^{(1)}}$ or $\boldsymbol{g_m^{(4)}}$ is dominant, it should be labeled as HH. Similarly, $\boldsymbol{g_m^{(2)}}$ or $\boldsymbol{g_m^{(5)}}$ corresponds to LH while $\boldsymbol{g_m^{(3)}}$ or $\boldsymbol{g_m^{(6)}}$ is relate to CH. And it is worth to note that HH subbands are decoupled from the LH and CH subbands while LH and CH always couple to each other.

B.2 Self-Consistent 6-Band *k·p* Model for III-Nitride Band Structure Calculations

B.2.1 Incorporation of Spontaneous and Piezoelectric Polarization Fields

Another unique property of wurtzite III-nitride structure is large polarization fields including spontaneous electric field (***P_{sp}***) and piezoelectric polarization field (***P_{pz}***), which are also taken into account in this calculation. The spontaneous polarizations for ternary (quaternary) III-nitride alloys are calculated based on linear treatment. Specifically,

for $In_xGa_{1-x}N$ $$P_{sp} = x \cdot P_{sp}(InN) + (1-x) \cdot P_{sp}(GaN)$$

for $Al_xGa_{1-x}N$ $$P_{sp} = x \cdot P_{sp}(AlN) + (1-x) \cdot P_{sp}(GaN)$$

for $Al_xIn_{1-x}N$ $$P_{sp} = x \cdot P_{sp}(AlN) + (1-x) \cdot P_{sp}(InN)$$

for $Al_xIn_yGa_{1-x-y}N$ $$P_{sp} = x \cdot P_{sp}(AlN) + y \cdot P_{sp}(InN) + (1-x-y) \cdot P_{sp}(GaN) \qquad \text{B-43}$$

The piezoelectric polarization can be:

$$P_{pz} = 2d_{31}(C_{11} + C_{12} - \frac{2{C_{13}}^2}{C_{33}})\varepsilon_{xx} \qquad \text{B-44}$$

where $\boldsymbol{d_{31}}$ is piezoelectric coefficient. Therefore, the electrostatic fields in each layer (***j_{th}***) as a result of both polarization and piezoelectric polarizations can be expressed as:

$$E_j = \frac{\sum_k l_k P_k/\varepsilon_k - P_j \sum_k l_k/\varepsilon_k}{\varepsilon_j \sum_k l_k/\varepsilon_k} \qquad \text{B-45}$$

where ***P*** is the total polarization, $\boldsymbol{\varepsilon}$ and **l** are the dielectric constant and the thickness of each layer, respectively.

B.2.2 Carrier Screening Effect and Calculation Flowchart

The carrier screening effect is also considered in this study, the eigenenergies and wavefunctions are calculated based on a self-consistent model by solving the Poisson equation:

$$\frac{\partial}{\partial z}\left(\varepsilon \frac{\partial V_{sc}}{\partial z}\right) = -\rho(z) \qquad \text{B-46}$$

where $\boldsymbol{V_{sc}}$ stands for the potential caused by the polarization field and $\boldsymbol{\rho(z)}$ is the charge distribution given by:

$$\rho(z) = |e|[p(z) - n(z)] \qquad \text{B-47}$$

where $\boldsymbol{p(z)}$ and $\boldsymbol{n(z)}$ are hole and electron concentrations, which are related to the wavefunctions of the $\boldsymbol{m_{th}}$ valence subband and the $\boldsymbol{n_{th}}$ conduction subband:

$$\begin{aligned} p(z) &= \sum_m |g_m(z)|^2 P_m \\ n(z) &= \sum_n |\phi_n(z)|^2 N_n \end{aligned} \qquad \text{B-48}$$

where the $\boldsymbol{n_{th}}$ surface electron concentration ($\boldsymbol{N_n}$) and $\boldsymbol{m_{th}}$ hole concentration ($\boldsymbol{P_m}$) are expressed as:

$$\begin{aligned} N_n &= 2\int_0^{\infty} \frac{2\pi k_t}{(2\pi)^2} \frac{1}{1 + e^{[E_{en}(k_t) - F_c]/K_B T}} dk_t \\ P_m &= 2\int_0^{\infty} \frac{2\pi k_t}{(2\pi)^2} \frac{1}{1 + e^{[F_v - E_{hm}(k_t)]/K_B T}} dk_t \end{aligned} \qquad \text{B-49}$$

Therefore, the total potential profiles for electron and hole are modified by considering self-consistent electrostatic potential:

$$
\begin{aligned}
U_e(z) &= U_0^e(z) - |e|V_{sc}(z) \\
U_h(z) &= U_0^h(z) - |e|V_{sc}(z)
\end{aligned}
\qquad \text{B-50}
$$

And the Schrodinger equations can be updated as:

$$
\begin{aligned}
&\left[-\frac{\hbar^2}{2m_e^*}\frac{d^2}{dz^2} + U_e(z)\right]\phi(z) = E_e\phi(z) \\
&\left[-\frac{\hbar^2}{2m_h^*}\frac{d^2}{dz^2} + U_h(z)\right]g(z) = E_h g(z)
\end{aligned}
\qquad \text{B-51}
$$

The Schrodinger equations are solved by the finite-difference method in this study with the spatial of 1 Å. More details of the finite-difference method for strained wurtzite structure calculation can be found in ref. [5] In summary, the numerical flowchart is summarized in figure B.2. Specifically, the band-edge potential is solved self-consistently because of the interdependent of the carrier distribution and band-edge potential. Therefore, the Schrodinger equation and Poisson equation were solved alternatively until the eigenenergy converges, which is set such as the errors of the eigenenergy converge to less than 0.1%. Then the wavefunctions are solved simultaneously based on the final results of the Schrodinger equation and Poisson Equation.

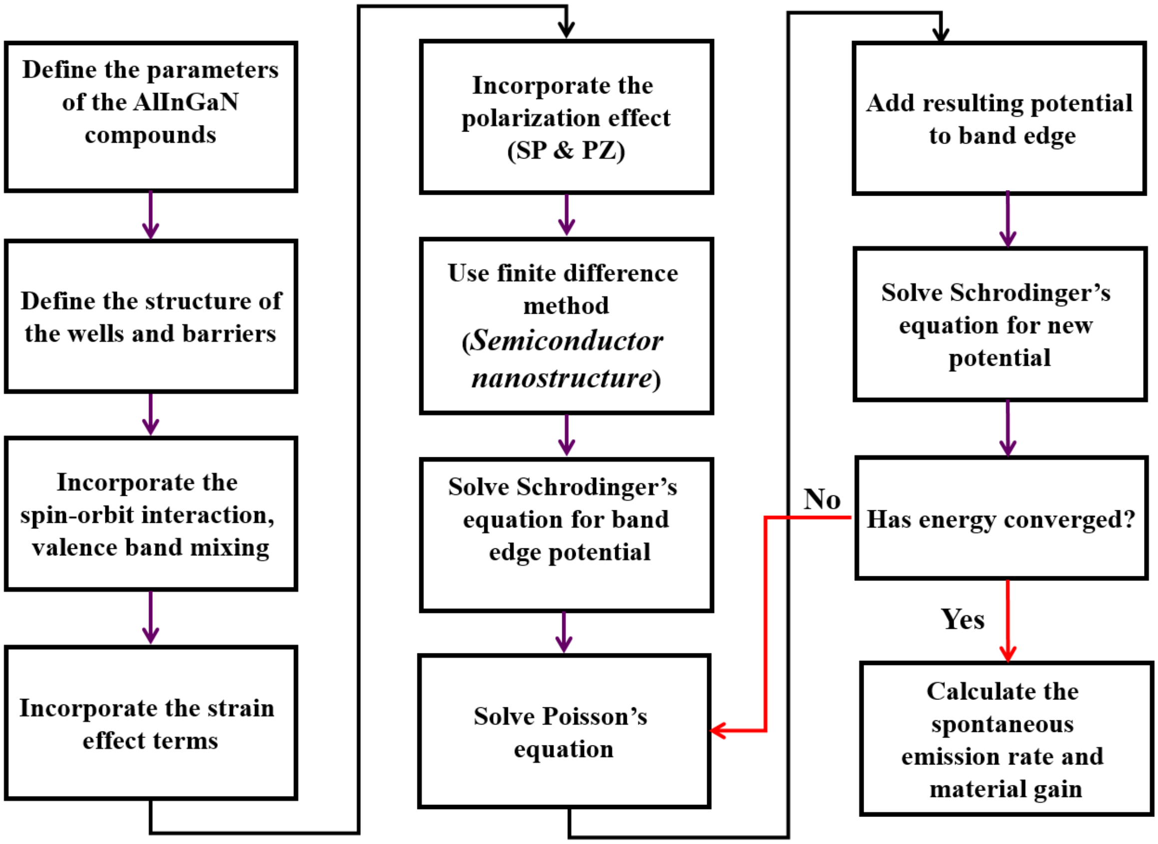

Figure B.2: *Numerical simulation flow chart for the self-consistent 6-band* ***k·p*** *model for wurtzite QW structure.*

B.3 Spontaneous Radiative Recombination Rate and Optical Gain of Strained Wurtzite III-Nitride QW

The polarization-dependent optical transition matrix element from the n_{th} state in conduction band to m_{th} state in the valence band can be obtained by:

TE-polarization ($\hat{e} = \hat{x}\ or\ \hat{y}\ \perp c$ axis):

$$
\begin{aligned}
|(M_x)_{nm}^{\sigma}(k_t)|^2 &= \frac{|\langle S|p_x|X\rangle|^2}{4}\left\{\left\langle \phi_n \middle| g_m^{(1)} \right\rangle^2 + \left\langle \phi_n \middle| g_m^{(2)} \right\rangle^2\right\} \qquad \text{for } \sigma = U \\
&= \frac{|\langle S|p_x|X\rangle|^2}{4}\left\{\left\langle \phi_n \middle| g_m^{(4)} \right\rangle^2 + \left\langle \phi_n \middle| g_m^{(5)} \right\rangle^2\right\} \qquad \text{for } \sigma = L
\end{aligned}
\tag{B-52}
$$

TM-polarization ($\hat{e} = \hat{z} \parallel c$ axis):

$$
\begin{aligned}
|(M_z)_{nm}^{\sigma}(k_t)|^2 &= \frac{|\langle S|p_z|Z\rangle|^2}{4}\left\{\left\langle \phi_n \middle| g_m^{(3)} \right\rangle^2\right\} \qquad \text{for } \sigma = U \\
&= \frac{|\langle S|p_z|Z\rangle|^2}{4}\left\{\left\langle \phi_n \middle| g_m^{(6)} \right\rangle^2\right\} \qquad \text{for } \sigma = L
\end{aligned}
\tag{B-53}
$$

Here we also define two equivalent energy parameters as:

$$
\begin{aligned}
\frac{m_0 E_{px}}{2} &= |\langle S|p_x|X\rangle|^2 \\
\frac{m_0 E_{pz}}{2} &= |\langle S|p_x|Z\rangle|^2
\end{aligned}
\tag{B-54}
$$

Based on Kane's model for wurtzite structure, these energy parameters can be related with the band structure parameters, as:

$$
\begin{aligned}
E_{px} &= \left(\frac{m_0}{m_e^t} - 1\right)\frac{E_g\left[\left(E_g + \Delta_1 + \Delta_2\right)\left(E_g + 2\Delta_2\right) - 2{\Delta_3}^2\right]}{\left(E_g + \Delta_1 + \Delta_2\right)\left(E_g + \Delta_2\right) - {\Delta_3}^2} \\
E_{pz} &= \left(\frac{m_0}{m_e^z} - 1\right)\frac{\left(E_g + \Delta_1 + \Delta_2\right)\left(E_g + 2\Delta_2\right) - 2{\Delta_3}^2}{\left(E_g + 2\Delta_2\right)}
\end{aligned}
\tag{B-55}
$$

Following the Fermi's Golden rule, the expression for optical gain is listed below:

$$
\begin{aligned}
g_{sp}^{e}(\hbar\omega) = {} & \frac{2q^2\pi}{n_r c \epsilon_0 {m_0}^2 \omega L_\omega} \sum_{\sigma=U,L} \sum_{n,m} \int \frac{k_t dk_t}{2\pi} |(M_e)_{nm}^{\sigma}(k_t)|^2 \\
& \times \frac{f_n^c(k_t)\left(1 - f_{\sigma m}^v(k_t)\right)(\gamma/\pi)}{\left(E_{\sigma,nm}^{cv}(k_t) - \hbar\omega\right)^2 + \gamma^2}
\end{aligned}
\tag{B-56}
$$

where $\boldsymbol{q}$, $\boldsymbol{m_0}$, $\boldsymbol{\epsilon_0}$, $\boldsymbol{c}$ stand for the magnitude of the electron charge, electron mass is free space, permittivity in free space, light velocity in free space, respectively. $\boldsymbol{n_r}$ and $\boldsymbol{L}$ are the refractive index and thickness of the quantum well region. It should be pointed out that the term $\boldsymbol{\hbar\gamma}$ is the half line width of the Lorentzian function, and we used $\boldsymbol{\tau_s} =$

$\mathbf{0.1\,ps}$ ($\boldsymbol{\gamma = (0.1\,ps)^{-1}}$) in the simulation. The expressions of the Fermi-Dirac distribution for the electrons in the conduction bands and valence bands are given by:

$$f_n^c(k_t) = \frac{1}{1 + \exp\left(\frac{E_n^c(k_t) - F_c}{k_B T}\right)}$$
$$f_{\sigma m}^v(k_t) = \frac{1}{1 + \exp\left(\frac{E_{\sigma,m}^v(k_t) - F_v}{k_B T}\right)} \qquad \text{B-57}$$

where F_c and F_v are quasi-Fermi levels for electrons and holes. Therefore, the electron and hole concentrations are given by:

$$n = \frac{2}{L_w}\sum_n \int \frac{k_t dk_t}{2\pi} f_n^c(k_t) = \frac{k_B T m_e^t}{\pi \hbar^2 L_w}\sum_n ln\left[1 + exp\left(\frac{F_c - E_n^c(0)}{k_B T}\right)\right]$$
$$p = \frac{1}{L_w}\sum_{\sigma=U,L}\sum_m \int \frac{k_t dk_t}{2\pi}(1 - f_{\sigma m}^v(k_t)) \qquad \text{B-58}$$

The momentum matrix element of the total spontaneous emission is the angular average of two TE-polarization components and a TM-polarization component, as:

$$\left|M_{sp}\right|^2 = \frac{1}{3}(2|M_x|^2 + |M_z|^2) \qquad \text{B-59}$$

The total spontaneous emission rate per energy interval per unit volume ($s^{-1}eV^{-1}cm^{-3}$) is expressed as:

$$r^{spon}(E = \hbar\omega) = \frac{{n_e}^2\omega^2}{\pi^2\hbar c^2}\frac{\left(2g_{sp}^x + g_{sp}^z\right)}{3} \qquad \text{B-60}$$

And the total spontaneous emission rate per unit volume ($s^{-1}cm^{-3}$) can be calculated as:

$$R_{sp} = \int_0^\infty r^{spon}(\hbar\omega)d(\hbar\omega) \qquad \text{B-61}$$

Reference for Appendix B

[1] S. L. Chuang, *Physics of photonic devices*. John Wiley & Sons, 2012.

[2] S. Chuang and C. Chang, "k·p method for strained wurtzite semiconductors," *Phys. Rev. B - Condens. Matter Mater. Phys.*, 54, 4, 2491, 1996.

[3] S. L. Chuang and C. S. Chang, "A band-structure model of strained quantum-well wurtzite semiconductors," *Semicond. Sci. Technol.*, 12, 3, 252, 1997.

[4] S. L. Chuang, "Optical gain of strained wurtzite GaN quantum-well lasers," *IEEE J. Quantum Electron.*, 32, 10, 1791, 1996.

[5] H. Zhao, R. A. Arif, Y. K. Ee, and N. Tansu, "Self-consistent analysis of strain-compensated InGaN-AlGaN quantum wells for lasers and light-emitting diodes," *IEEE J. Quantum Electron.*, 45, 1, 66, 2009.